RATE AND NOISE-INDUCED TIPPING WORKING IN CONCERT

Katherine E. Slyman

A dissertation submitted to the faculty at the University of North Carolina at Chapel Hill in partial fulfillment of the requirements for the degree of Doctor of Philosophy in the Department of Mathematics in the College of Arts and Sciences.

Chapel Hill
2023

Approved by:

Christopher K.R.T. Jones

John Gemmer

Jason Metcalfe

Katherine Newhall

Erik Van Vleck

ABSTRACT

Katherine E. Slyman: Rate and Noise-Induced Tipping Working in Concert
(Under the direction of Christopher K.R.T. Jones)

Tipping is the rapid, and often irreversible, change in the state of a system[5]. Rate-induced tipping occurs when a ramp parameter changes rapidly enough to cause the system to tip between co-existing, attracting states, while noise-induced tipping occurs when there are random transitions between two attractors of the underlying deterministic system. This work builds theory for tipping events in low-dimensional dynamical systems with additive noise and time-dependent parameters, in which noise is not vanishingly small. The central question is understanding what information can be extracted from the theory of large deviations for noise levels outside the validity of the approach, where the guiding principles are geometric dynamical systems methods and Monte Carlo simulations. Both tipping mechanisms are first considered within a model of the oceanic carbon cycle, in which the key objective is understanding how the system tips from a stable fixed point to a stable periodic orbit. While rate-induced tipping away from the fixed point is straightforward, the noise-induced tipping is challenging due to a periodic orbit forming the basin boundary for tipping. Noisy trajectories will tend to cycle around the periodic orbit as the noise vanishes, but as the noise becomes slightly larger, the escaping paths become resistant to cycling. An interesting phenomena exposed is that a subset of the unstable manifold of the fixed point in the Euler-Lagrange system, with Maslov index zero, determines where the noisy trajectories escape. After considering tipping mechanisms individually, we consider a one-dimensional differential equation with both additive noise and a ramp parameter. The addition of noise to the system can cause it to tip well below the critical rate at which rate-induced tipping would occur. We achieve this by finding a global minimizer of the Freidlin-Wentzell functional of large deviation theory that represents the most probable path for tipping. This is realized as a heteroclinic connection for the Euler-Lagrange system associated with the Freidlin-Wentzell action and it exists for all rates less than or equal to the critical rate. This framework is extended to show the existence of a heteroclinic orbit for a fairly general class of functions.

To my family and friends, with special thanks to Moose and Philly.

ACKNOWLEDGEMENTS

I would like to express my sincere gratitude to my advisor Chris Jones for taking me on as a student and for providing a wide range of research and mentorship opportunities. He was the best advisor that I could have asked for and I look forward to continuing collaboration with him in future years to come.

I am indebted to John Gemmer for introducing me to applied mathematics in 2016, and thus kickstarting my career. I am thankful to Claire Kiers for introducing me to the concept of rate-induced tipping, and providing me with notes and code to help me get started in this field. I am appreciative of the members of my dissertation committee for answering both math and career-related questions over the last few years.

I am grateful for my friends Kate Daftari and Maddie Brown for helping me get through graduate school and for being sounding boards on research ideas and presentation practice. I give special thanks to my friends and family for always asking what I do, even when they still have no idea what I do. Lastly, I am especially grateful to my partner Moose for always being a constant source of encouragement.

TABLE OF CONTENTS

LIST OF FIGURES

LIST OF TABLES

CHAPTER 1

Introduction

The Intergovernmental Panel on Climate Change (IPCC)[15] defines a tipping point as "a level of change in system properties beyond which a system reorganises, often in a nonlinear manner, and does not return to the initial state even if the drivers of the change are abated." For climate systems, tipping points refer to critical thresholds when global or regional climate switch stable states[15]. However, keeping the definition of tipping points free of specific applications, tipping points occur when a change to a parameter or variable causes an abrupt change to the state of the system.

Tipping dynamics can best be understood in bistable systems, where qualitatively different stable states coexist for a given set of parameters within the system[26]. For a system initialized near a stable state, as the external conditions on the system change with time, we would expect that the stable state changes along with it, though not drastically. This phenomenon is described as a moving stable state[43]. Often, the system is able to adapt to changing external conditions and continuously track the moving stable state. If the system is able to track the moving stable state, no tipping occurs in the system, but this is not always possible. Many systems exhibit these multiple, alternative stable states where underlying dynamics, parameter values, or stochasticity can cause the abrupt shift from one stable state to another, such that the system cannot continuously track the stable state. So how should these transitions be classified? There are three main mechanisms for tipping in dynamical systems: bifurcation-induced, rate-induced, and noise-induced[6]. They have been classified according to whether they involve a bifurcation in the system (B-tipping), a parameter shift (R-tipping), or the addition of random fluctuations (N-tipping). Unlike B-tipping, with R-tipping there is no bifurcation in the system to explain the change of stability of a fixed point. B-tipping and R-tipping both occur in deterministic systems, while N-tipping requires a stochastic component. A combination of different mechanisms can also lead to tipping.

This dissertation focuses on the occurrence of a parameter shift (R-tipping), the addition of random fluctuations (N-tipping), as well as their interplay.

1.1 The Main Problem

The main objectives of this work are to build and present a theory for understanding tipping events in low-dimensional dynamical systems with additive noise and time-dependent parameters. The underlying motivation is to understand the interplay of rate and noise-induced tipping, mainly, how the two mechanisms can induce tipping together when individually it is impossible or unlikely. The guiding principles of this work come from geometric dynamical systems methods along with numerical simulations for corroboration and visualization. This approach implies we juggle between two points of view in these problems: the dynamical systems perspective and the stochastic perspective.

Many of the applications we have interest in, and are motivated by, have nonvanishingly small noise levels, leading to the central questions explored: to what extent does the Freidlin-Wentzell theory of large deviations hold for small levels of noise, away from the limit, and what information can be extracted from this theory when the levels of noise are seemingly outside the validity of the approach? The following elements create the foundation for approaching this question.

1. The Euler-Lagrange equations are derived from the minimization of the Freidlin-Wentzell action functional, and then are recast as a Hamiltonian system.
2. The unstable and stable manifolds for the base and threshold states in this Hamiltonian system, respectively, are found analytically and or computationally.
3. The heteroclinic orbits, that arise from the transverse intersections of these manifolds, are also found analytically and or computationally.
4. Monte Carlo simulations are used as a way to gain insight into noisy behavior and to corroborate most probable path results. This includes determination of convergence of the simulations for different events. See Chapter 3.2 for further explanation.

Considerable insight can be gained from using both the dynamical systems and stochastic perspectives. In Chapter 4, an oceanic carbon cycle model is explored in which the focus is on the escape from a fixed point through an unstable periodic orbit, both due to a time-dependent parameter as well as noise, but as separate phenomena. In the noisy system, in the small noise limit, realizations should cycle around the unstable periodic orbit[16]. However, away from the limit, we see something quite different: the Monte Carlo simulations show there is a specific region on the unstable periodic orbit where trajectories escape. The goal is to explain from the dynamical systems point of view why this different behavior occurs. We find two heteroclinic orbits form the boundaries of these escaping trajectories. There exists a subset of the unstable manifold of the stable fixed point that is comprised of local minimizers, and an interesting phenomena discovered is that this subset of local minimizers is actually what determines where the noisy trajectories escape. In Chapter 5, the main focus is a canonical problem where the system has both a time-dependent component and a stochastic component. We study tipping between two saddle nodes in order to learn to what extent rate and noise act in concert to enhance the likelihood of tipping. It is revealed that the Freidlin-Wentzell theory still holds in regard to the dynamical structure for small noise strengths, namely that the heteroclinic connection is the most probable path. The upshot of this work is that this most probable path is unambiguous, as it has the least action value, and the Monte Carlo simulations center around this path. The work finishes in Chapter 6 with generalizing the nonlinearity within the rate and noise canonical problem for a fairly general class of functions.

1.2 Motivation

The primary motivation of this work relates to climate subsystems. The Earth's climate is changing due to steadily warming temperatures caused by rising levels of greenhouse gases[15]. There are parts of the Earth system that have the potential for large, abrupt, and irreversible transitions in response to this warming that could lead to cascading effects[15]. These changes can be characterized as tipping points[15] and as presented by Lenton[30] and Lenton et al.[31], there are many such examples: Greenland ice sheet loss, break-off of Antarctic ice-sheets, boreal forest dieback, and permafrost loss, to name a few. Given the magnitude of the impacts of these phenomena, a comprehensive understanding of tipping phenomena is needed to predict, and attempt to mitigate, these irreparable changes. There are other major reasons to care about climate change: it has played a role in the collapse of human societies, it exacerbates infectious disease spread and spillover risk, and it affects the severity of extreme weather events[27].

The theoretical and computational tools used in these applications can be adapted to application in social systems, as tipping points also exist in social systems, and promise to have equal significance. Examples of tipping points in social systems include the disappearance of the gender gap in American higher education in the 1970s[2] and the rapidly increasing number of people in 2013 who signalled their support for same-sex marriage[3]. Even the attempts to stop tipping within the above-mentioned climate subsystems are related to tipping points in social change and human behavior, as practical solutions to climate change rely on the collective action of individuals. There is unequivocal evidence that human activity is the principal cause for the Earth's warming[15], so stabilizing the climate system critically depends on activating contagious and fast-spreading processes of social and technological change[34]. This corresponds to finding positive tipping points in the changing attitudes about climate change. For example, this theory could be used to help tip social norms about electric vehicle use or to promote the decarbonization of the power sector[39].

As seen above, there can be either undesirable or desirable outcomes as a result of tipping within a system. Desirable outcomes related to positive tipping points include the extinction of an infectious disease, the eradication of an ecological pest, or the spread of changing climate opinions, while undesirable outcomes would occur when climate subsystems fail or at the outbreak of an infectious disease. Due to the diversity of important applications, understanding the mathematics of tipping promises to have significant impact on many existing and reoccurring problems in our current society.

In recent years, there has been an increase in the use of stochastic systems to model a variety of important phenomena, including climate, biological, ecological, and epidemiological systems; these applications are directly related to our motivation. Within these stochastic models the main investigations include studying how noise affects these phenomena on a variety of scales and determining if noise can induce rare transitions[21]. The goal of understanding these phenomena demonstrate the demand for developing methods that quantify the impacts of noise in these complex systems.

In addition, within relevant models, there are many such parameters that could realistically be time-dependent or have time-varying external conditions, emphasizing a second demand for synthesizing techniques of rate-induced tipping with those of noise-induced tipping.

1.3 Historical Background

1.3.1 Rate-Induced Tipping

Of the three major tipping mechanisms, rate-induced tipping is the most recently analyzed. The first paper in which rate-induced tipping was described and written about formally was by Ashwin et al.[6], though it was recognized as a new tipping mechanism in the work of Wieczorek et al.[42]. The context of the study of rate-induced tipping has largely been for deterministic, continuous time systems of the form

$$\dot{x} = f(x, \Lambda(rt)), \tag{1.1}$$

and determining the system's sensitivity on the parameter shift $\Lambda(rt)$. There has also been recent research on rate-induced tipping in discrete-time maps[28] as well as in some noisy systems[36, 37].

The definition and language of rate-induced tipping has continued to evolve over the last decade with the aim of creating the most accurate and encompassing definition as possible. Initially, rate-induced tipping was defined for when trajectories left a predetermined radius around a stable quasistatic equilibrium (QSE)[6].

It progressed then to studying the behavior of a *local pullback attractor*, a trajectory $x^r(t)$ dependent on the size of r such that $\lim_{t\to-\infty} x^r(t)$ is the QSE at the start of the parameter shift. If $\lim_{t\to\infty} x^r(t)$ converged to the stable QSE at the end of the parameter shift, the solution was said to *end-point track* the stable QSE, as the trajectory tracked the moving stable state from its initial to ending place. Otherwise it failed to end-point track the stable QSE, and rate-induced tipping occurred[5].

Most recently still, using the behavior of trajectories, rate-induced tipping occurs if a trajectory initialized at a hyperbolic sink tends to a *regular edge state*, defined as a compact hyperbolic invariant set with one unstable direction and orientable stable manifold lying on a basin boundary in the frozen time system[43]. We will use the definition from Wieczorek et al.[43], as seen in Chapter 2.1.

While the definition and language of rate-induced tipping have evolved, so have the methods to study these nonautonomous systems. Initially, to deal with a nonautonomous system, the strategy was to rewrite it as a first order autonomous system by creating a new function $s = rt$ or $s = t$. The derivative of the function, $\dot{s}$, added a first order equation to the system. More recently, a compactification technique was developed by Wieczorek et al.[44]. This process turns the nonautonomous system into a higher dimensional first order system by making a coordinate transform that allows $\dot{s}$ to be a function of s. The resulting system has equililbria and invariant sets, implying a dynamical systems perspective can be taken to study rate-induced tipping. This technique turns the rate-induced tipping problem in the nonautonomous system into finding a heteroclinic orbit in the autonomous compactified system.

1.3.2 Noise-Induced Tipping

Noise-induced tipping encompasses a range of phenomena, including transitions between metastable states and bursting behavior. The study of noise-induced tipping has been governed by the Freidlin-Wentzell theory of large deviations. This framework is fully presented in Freidlin and Wentzell's monograph[23], Forgoston and Moore's review article[21], and for gradient systems in Berglund's review article[9].

This theory provides the basis to find the expected time of switching between coexisting stable states and how to determine the *most probable path* of escape between these states, defining the most probable path as the path that is most likely to occur among all possible paths[21]. This path will exhibit the highest probability among all the paths connecting the initial and final states. Therefore, the most probable path can be thought of as the mode of a probability distribution of escaping paths. Using the theory of large deviations, the most probable paths of escape should minimize the Freidlin-Wentzell functional. Computing minimizers of this functional over all paths and all travel times provide an estimation for the optimal path, though it is often approximated by finding critical points of the functional.

The theory of large deviations is rooted in the study of systems whose underlying deterministic dynamics are gradient. In these gradient systems, it is straightforward to calculate the expected time to tip between stable states of the corresponding deterministic system as well as the transition paths of maximal likelihood between them. For non-gradient systems, Freidlin and Wentzell introduced the quasipotential as a way to quantify these same stochastic dynamics. The quasipotential is calculated by solving the static Hamilton-Jacobi equations[33], though it is a numerically difficult task. Cameron[12] made significant headway as she developed a numerical algorithm for the computation of quasipotentials based on the ordered upwind method: a method used to approximate the solution of static Hamilton-Jacobi equations[12]. Even as numerical methods keep developing, it remains a challenge to find the quasipotential.

From the dynamical systems perspective, the quasipotential is related to the projection of an unstable manifold in the Hamiltonian system derived from the Euler-Lagrange equations that come from the minimization of the Freidlin-Wentzell action functional[17]. Using this framework, a dynamical systems approach can be taken to the quasipotential and the most probable escape path. The advantage of this approach is that in some ways, fixed points and invariant sets have more tangibility than the quasipotential. Also, as this work is for lower-dimensional dynamical systems, implying it is feasible and easier to generate unstable manifolds of base states than to generate the quasipotential.

To complement the first two approaches, as well as to aid in providing a full picture of the dynamics, requires the use of numerical simulations. Monte Carlo simulations provide a useful tool in collecting noisy realizations, which can be visualized to find where noisy trajectories escape or finding the expected time for escape. To compute expectations and the most probable escape path, empirically, we use the Monte Carlo method in which the event is simulated multiple times until it forms a converged distribution on which a statistical analysis can be run. The difficulty of this approach stems from the fact that the tipping events of interest are actually very unlikely to occur, and form a very small subset of the behaviors the system can exhibit. One method to implement this strategy requires the use of importance sampling[45]. This technique is necessary for smaller noise strengths because tipping occurs at a much lower frequency and more realizations are needed to get converged data. Importance sampling biases realizations towards the rare event, speeding up the time needed to find converged sets of Monte Carlo simulations.

1.4 Challenges and Difficulties

While the Freidlin-Wentzell theory is a well-developed mathematical framework to understand alternative stable states in stochastic systems, it does have a shortcoming. The theory was developed for vanishingly small noise, also known as the small noise limit[23]. This is a serious issue for the motivating applications since for many of these applications, the small to intermediate levels of noise are actually more realistic and appropriate. For these larger levels of noise, the transient behavior of the underlying deterministic system becomes relevant. As the larger noise tends to impact the system sooner, and not asymptotically, it interacts with the transient dynamics. Underlying this work with the dynamical systems perspective of the quasipotential gives insight into these transient dynamics.

Another challenge is that the complex systems mentioned thus far are not uniquely affected by only one tipping mechanism. For instance, climate change is a rate-induced tipping problem but it is also a noisy system. These two components are true for many relevant climate subsystems. Many conceptual models of climate systems contain multiple mechanisms that can induce tipping, so there is a clear need for mathematical approaches that combine techniques from both rate-induced and noise-induced tipping. However, as mentioned earlier, there is not much theory related to systems with both additive noise and a ramp parameter, except for the work of Ritchie and Sieber[36,37].

CHAPTER 2

Background on Tipping Mechanisms

2.1 Rate-Induced Tipping

Rate-induced tipping occurs when a sufficiently quick change to the parameter of a system may cause the system to move away from one attractor to another[6]. An analogy to illustrate this tipping mechanism relates to the party trick of pulling a tablecloth out from underneath a set of dishes on a table. If the tablecloth is pulled slowly, it carries all of the dishes with it. Alternatively, if the tablecloth is pulled quickly enough, the dishes will remain on the table. There are two distinct outcomes in this situation. It is not how far one pulls the tablecloth, but actually the speed at which the tablecloth is pulled, that determines this outcome. Likewise with rate-induced tipping, the behavior of the solutions is not determined by how much a parameter changes, but by how quickly it changes in time.

Following the work of Ashwin et al.[5,6] and Wieczorek et al.[43], we lay out the framework needed to describe rate-induced tipping more formally and also introduce notations used throughout this work.

Consider the autonomous differential equation

$$\dot{x} = f(x, \lambda), \tag{2.1}$$

where $x \in \mathbb{R}^n, \lambda \in \mathbb{R}^m, f \in C^2(\mathbb{R}^{m+n}, \mathbb{R}^n), t \in \mathbb{R}$, and $\dot{x}$ is the derivative of x with respect to time, $\frac{dx}{dt}$. Now, instead of a fixed λ, suppose that λ changes in time. We replace λ with an external input $\Lambda_r(t) = \Lambda(rt) \in C^2(\mathbb{R}, \mathbb{R}^m)$, $r \in \mathbb{R} > 0$, and specifically assume that Λ_r is *bi-asymptotically constant*. This implies that Λ_r is a parameter shift that satisfies

$$\lim_{t \to -\infty} \Lambda_r(t) = \lambda_- \in \mathbb{R}^m \text{ and } \lim_{t \to \infty} \Lambda_r(t) = \lambda_+ \in \mathbb{R}^m,$$

where λ_- is the *past limit state* and λ_+ is the *future limit state*. In addition to assuming that Λ_r is bi-asymptotically constant, assume that Λ_r is monotonically increasing, and that

$$\lambda_- < \Lambda_r < \lambda_+.$$

These assumptions on Λ_r allow a gradual transition between λ_- and λ_+ in time, where the size of r, the *rate parameter*, determines how quickly Λ_r transitions between λ_- and λ_+. While there are different types of functions that fit this criteria, we use transformations on a hyperbolic tangent function as Λ_r. The external input Λ_r is also called a *ramp function* or a *ramp parameter*.

Definition 2.1.1. Suppose $\Lambda_r(t)$ is a bi-asymptotically constant external input, with future limit state λ_+ and past limit state λ_-. Suppose that for all $t \in \mathbb{R}$, $X(t)$ is a fixed point of (2.1) when $\lambda = \Lambda_r(t)$ such that $(t, X(t))$ is a connected curve, and when $\lambda_\pm, X(t) = X^\pm$. Then $(t, X(t))$ is a stable (unstable) path if $X(t)$ is an attracting (repelling) fixed point for all t. These paths can be referred to as paths of stable (unstable) fixed points in the frozen time system.

Replacing λ with $\Lambda_r(t)$ in (2.1) leads to

$$\dot{x} = f(x, \Lambda_r(t)), \tag{2.2}$$

where $x \in \mathbb{R}^n, \Lambda_r(t) \in \mathbb{R}^m, f \in C^2(\mathbb{R}^{m+n}, \mathbb{R}^n), t \in \mathbb{R}$, and $r \in \mathbb{R}$. Solution behaviors of (2.2) change for different values of r. Let $x^{r^*}(x_0)$ denote a solution to system (2.2) initialized at $x = x_0$ with $r = r^*$. We define rate-induced tipping using the definition of Wieczorek et al.[43] below.

Definition 2.1.2. Consider an nonautonomous system (2.2) with a bi-asymptotically constant external input $\Lambda_r(t)$, with future limit state λ_+ and past limit state λ_-. Suppose that when $\Lambda_r = \lambda_-$, the system has a hyperbolic sink e^-, and when $\Lambda_r = \lambda_+$, the system has a compact invariant set η^+ that is not an attractor. The system (2.2) undergoes *rate-induced tipping* from e^- if there are rates $0 < r_2 < r_1$ such that $\lim_{t\to\infty} x^{r_1}(e^-) \to \eta^+$ and $\lim_{t\to\infty} x^{r_2}(e^-) \nrightarrow \eta^+$. The first value of r such that $\lim_{t\to\infty} x^r(e^-) \to \eta^+$ is called the critical rate and is denoted by r_c.

Definition 2.1.3. Suppose that when $\Lambda_r(t) = \lambda$ system (2.2) has a hyperbolic sink e^-. The *basin of attraction* for e^- is defined as $\mathbb{B}(e^-, \lambda) = \{x \mid \lim_{t\to\infty} x(t) = e^-\}$.

Essentially, if $r < r_c$, solutions will end-point track the path of fixed points in the frozen time system on which they were initialized. When $r = r_c$, the solution tips to the basin boundary of e^-, and when $r > r_c$, the solution either tips to infinity or a different attractor, as it left the basin of attraction for e^-. It is worth mentioning that not all choices of Λ_r result in rate-induced tipping. There is theory to determine if a system will or will not tip with a chosen Λ_r, and the conditions change based on the dimension of the system. The conditions for a system to undergo rate-induced tipping are the same for $x \in \mathbb{R}^n$, for $n \geq 1$. From the work of Ashwin et al.[5], and Kiers and Jones[29], we have the following theorem.

Theorem 2.1.4. *Suppose Λ_r gives rise to a stable path $(t, X(t))$ in* (2.2) *with $x \in \mathbb{R}^n$, for $n \geq 1$, and $X^{\pm} = \lim_{t \to \infty} X(t)$. When $\Lambda_r = \lambda_-$, assume the system has an attracting equilibrium X^-. If there is a $Y^+ \neq X^+$ such that Y^+ is an attracting equilibrium of* (2.1) *for $\lambda = \lambda^+$, and $X^- \in \mathbb{B}(Y^+, \lambda^+)$, then there is rate-induced tipping away from X^- to Y^+ for this Λ_r, for sufficiently large $r > 0$.*

The goal is to use both geometric and analytical tools from dynamical systems to gain insights into the mechanism of the rate-induced tipping. However, after introducing Λ_r, (2.2) is a nonautonomous system. The system in (2.2) must be converted to an equivalent autonomous system in order to apply these tools.

There are two main approaches for converting (2.2) back into an autonomous equation. The standard approach to investigate rate-induced tipping is to augment the system by introducing a new variable, $s = t$. Making the corresponding substitutions and differentiating, results in the $n+1$-dimensional autonomous system given by

$$\dot{x} = f(x, \Lambda_r(s)),$$

$$\dot{s} = 1.$$

While this method is well-suited for numerical computations, it does not have the underlying structure to approach the problem from a dynamical systems perspective; there are no fixed points as $\dot{s}$ will never equal zero.

The alternative approach to convert the nonautonomous system (2.2) into an autonomous system is to use *compactification*[44]. In this process, the invertibility of the time-dependent parameter is used to make a coordinate transform and then the system is augmented into an autonomous $n+1$-dimensional extended system. The compactified system will contain equilibria and compact invariant sets in the extended phase space, such as unstable and stable manifolds, allowing us to use tools and methods from dynamical systems to study the compactifed system. Solutions of (2.2) that remain bounded as $t \to \pm\infty$ become heteroclinic connections in the compactified system[44]. Therefore, compactification transforms the rate-induced tipping problem into a heteroclinic connection problem, allowing the analysis of nonautonomous rate-induced tipping in finite phase space. From a big picture perspective, compactification 'glues' the dynamics at infinity onto a finite phase space.

The first step to compactify a system is to augment the system with $y = \Lambda_r(t)$ as an additional dependent variable, where Λ_r is bi-asymptotically constant, as hypothesized above. Based on the assumptions of $\Lambda_r(t)$, y is invertible. Due to this invertibility of y, the differentiation and substitution results in the $n+1$ first order system given by

$$\begin{aligned} \dot{x} &= f(x, \Lambda_r(\Lambda_r^{-1}(y))) = f(x,y), \\ \dot{y} &= \dot{\Lambda_r}(\Lambda_r^{-1}(y)), \end{aligned} \tag{2.3}$$

where $y \in (\lambda_-, \lambda_+)$. The second step is to make the y-interval closed by including the future and past limit states of $\Lambda_r : \lambda_\pm$. This process creates an autonomous compactified system that is defined on the extended phase space.

To highlight these two methods for studying rate-induced tipping, we consider the system

$$\dot{x} = -(x-\lambda)(x-\lambda-1)(x-\lambda-2), \tag{2.4}$$

where we replace λ with a time-changing parameter $\Lambda_r(t) = 1 + \tanh(rt)$. Notice that (2.4) has three fixed points: $x = \lambda, \lambda+1$, and $\lambda+2$, where $x = \lambda, \lambda+2$ are stable and $x = \lambda+1$ is unstable. Approach 1 is demonstrated in Example 2.1.5 and Approach 2 demonstrated in Example 2.1.6.

Example 2.1.5. (Approach 1)

Consider

$$\dot{x} = -(x-\Lambda_r(t))(x-\Lambda_r(t)-1)(x-\Lambda_r(t)-2). \tag{2.5}$$

Solving $\dot{x} = 0$ in (2.5) implies that there are three branches of equilibria in the frozen time system, $x = \Lambda_r(t), x = 1+\Lambda_r(t)$, and $x = 2+\Lambda_r(t)$, where as $t \to -\infty, x \to 0,1,2$, and as $t \to \infty, x \to 2,3,4$. The two branches of equilibria $x = \Lambda_r(t)$ and $x = 2+\Lambda_r(t)$ track the stable fixed points of (2.5) in the frozen time system, while the branch $x = 1+\Lambda_r(t)$ tracks the unstable fixed point of (2.5) in the frozen time system.

Using the first approach, we set $s = t$ and augment (2.5) to become

$$\begin{aligned} \dot{x} &= -(x-\Lambda_r(s))(x-\Lambda_r(s)-1)(x-\Lambda_r(s)-2), \\ \dot{s} &= 1. \end{aligned} \tag{2.6}$$

Initializing the system on the upper branch at $x = 2, s = -10$, there are different solution behaviors depending on the size of r, as shown in Figure 2.1. Notice for $r < r_c$, the system does not tip, but for $r \geq r_c$, the solution curve tips to the unstable branch of x, or to the stable branch of x. The first time the solution curve tips to the unstable branch of x determines the value of r_c.

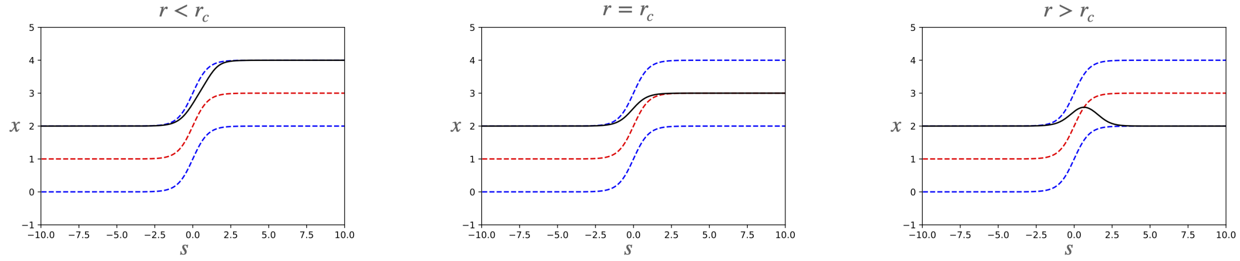

Figure 2.1: Solutions (black) of (2.6) for varying values of r. The blue dashed curves track $x = \Lambda_r(s)$ and $x = 2 + \Lambda_r(s)$ in the frozen time system, and the red dashed curve tracks $x = 1 + \Lambda_r(s)$ in the frozen time system.

Example 2.1.6. (Approach 2)

Consider

$$\dot{x} = -(x - \Lambda(rt))(x - \Lambda(rt) - 1)(x - \Lambda(rt) - 2). \tag{2.7}$$

Using the second approach, we make the coordinate transform $y = 1 + \tanh(rt)$, resulting in the system given by

$$\begin{aligned} \dot{x} &= -(x-y)(x-y-1)(x-y-2), \\ \dot{y} &= r\,\mathrm{sech}^2(\tanh^{-1}(y-1)) \\ &= r(1 - (\tanh(\tanh^{-1}(y-1)))^2) \\ &= r(1-(y-1)^2). \end{aligned} \tag{2.8}$$

Now, (2.8) is an autonomous first order system in which tools from dynamical systems can be used to study the system. There are a total of six fixed points in the system given by (2.8), three when $y = 0$: $(0,0), (1,0), (2,0)$, and three when $y = 2$: $(2,2), (3,2), (4,2)$, written in the form (x,y). Initializing the system at the fixed point $(2,0)$ corresponds to initializing on the upper branch in Example 2.1.5. For numerical purposes, initialize the system at $(2, 10^{-8})$ instead, as otherwise it would take infinite time to leave the fixed point $(2,0)$.

Just as in Example 2.1.5, there are different solution behaviors depending on the size of r, as shown in Figure 2.2. Notice for $r < r_c$, the system does not tip, but for $r \geq r_c$, the solution curve tips to the fixed point $(3,2)$ or $(4,2)$, resulting in heteroclinic connections between the fixed points. When $r = r_c$ the solution curve tips to $(3,2)$, as this marks the solution tipping to the basin boundary.

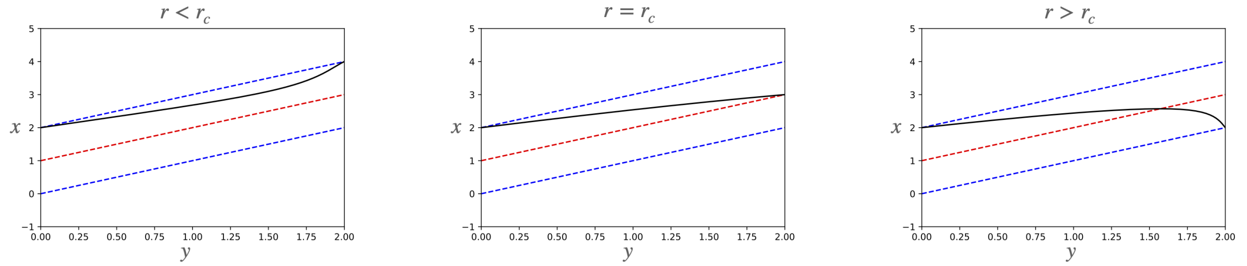

Figure 2.2: Solutions (black) of (2.8) for varying values of r. The blue dashed curves track the stable fixed points $x = y$ and $x = 2 + y$ in the frozen time system, and the red dashed curve tracks the unstable fixed point $x = 1 + y$ in the frozen time system.

2.2 Noise-Induced Tipping

In a variety of dynamical systems modeling physical phenomena, noise plays an essential role. Noise in a system can come from external forcing (additive noise) or from random internal dynamics (multiplicative noise). Noise-induced tipping occurs when noisy fluctuations result in a system departing from a neighborhood of an attractor[6]. It is well established that even small noise can result in large behavioral changes within the system, despite the fact that occurrences are rare for weaker noise[21].

This work focuses on systems with additive noise: the system in (2.1) is modified to include the possibility of random effects disturbing the system, but is restricted to the one-dimensional case ($n = 1$). Mathematically this implies a stochastic process term is added to the differential equation. A formal way to write this is to consider the stochastic differential equation (SDE) given by

$$dx = f(x, \lambda)dt + \sigma dW_t, \tag{2.9}$$

where $x \in \mathbb{R}$ is a *stochastic process* parameterized by time, f is the deterministic piece of the system and is often referred to as the *drift*, W_t is a standard *Wiener process*, and $\sigma > 0$ denotes the *noise strength* and often referred to as the diffusion coefficient. The Wiener process, W_t, is a stochastic (meaning random) process used to describe Brownian motion associated with additive Gaussian white noise. It is characterized by the following properties.

1. $W_0 = 0$, the process is initialized at 0.

2. The Brownian increment $W_{t+\Delta t} - W_t$ is independent of the past, W_s, where $0 \leq s \leq t$.

3. The Brownian increment, $W_{t+\Delta t} - W_t$, is normally distributed with mean zero and variance Δt.

4. W_t is continuous in t.

Notice that (2.9) is in a differential form. However, stochastic processes are continuous but not differentiable, as illustrated in Figure 2.3(a). The SDE (2.9) is actually a shorthand notation for the integral equation

$$x(t) = x(0) + \int_0^t f(x,\lambda)ds + \int_0^t \sigma dW_s, \tag{2.10}$$

where a solution to a stochastic differential equation is also a stochastic process. Refer to Figure 2.3 for illustrations of both one and two-dimensional Wiener processes, corresponding to one and two-dimensional Brownian motion.

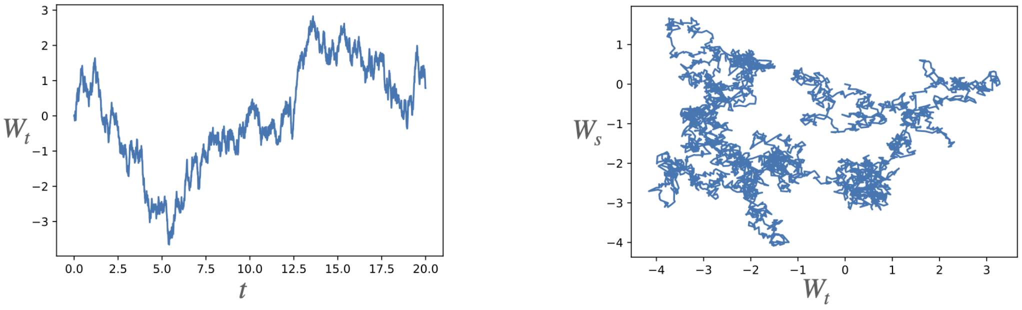

(a) (b)

Figure 2.3: (a) A single realization of a one-dimensional Wiener process. Upon inspection, observe that the process is continuous but not differentiable. (b) A single realization of a two-dimensional Wiener process.

With the addition of additive noise to the system, the system will exhibit noise-induced tipping, though it becomes more of a question about timescales and the tipping path a trajectory takes. While this section considers $x \in \mathbb{R}$, we define a realization that exhibits noise-induced tipping for $x \in \mathbb{R}^n$ as the following.

Definition 2.2.1. Consider a stochastic differential equation as in (2.9), where $x \in \mathbb{R}^n$. Suppose the drift $f(x,\lambda)$ has at least one stable state e_1. Let $z(t)$ be an approximation to a sample drawn from the distribution corresponding to the random variable solution of (2.9), called a realization. The realization $z(t)$ exhibits *noise-induced tipping* away from e_1 if $z(t)$ is not in the basin of attraction of e_1 for some $t > T$ for which $z(t)$ is defined, or if there is an escape to infinity from e_1.

As earlier with rate-induced tipping, we show examples of noise-induced tipping. Since system (2.9) is a one-dimensional system, both of these examples are gradient systems, where each example demonstrates a different time series behavior. Deterministically, gradient systems are differential equations that have the form $\dot{x} = -\nabla V(x)$, with V a real valued function, and in the SDE formulation, is the drift component.

Gradient systems have asymptotic formulae for the expected time to tip between two fixed points[9] and the most probable path for tipping between the two points can be explicitly calculated. From Berglund[9], an approximation for the expected time to tip between two minima x^* and y^*, separated by a saddle z^*, is given by

$$\mathbb{E}[\tau] \approx Ce^{\frac{2\Delta V}{\sigma^2}}, \tag{2.11}$$

where V is the associated potential function, ΔV gives the height of the potential barrier, and

$$C \approx \frac{2\pi}{\sqrt{V''(x^*)|V''(z^*)|}}. \tag{2.12}$$

This approximation for C can be found using Laplace's method. The most probable path for tipping between these points would just be the reversed time dynamics of the system.

Higher dimensional systems are unlikely to be gradient, and there is no reason for a system to be gradient unless it was derived from a physical system with special constraints. One such example is if a specific form of dissipation was underlying the system.

Example 2.2.2.

Consider the gradient, stochastic differential equation

$$\begin{aligned} dx &= -\nabla V(x)dt + \sigma dW_t \\ &= -\nabla(0.05x^2(x^2-4))dt + \sigma dW_t \\ &= (-0.2x^3 + 0.4x)dt + \sigma dW_t, \end{aligned} \tag{2.13}$$

where V is the associated potential function, as seen in Figure 2.4(a). The three fixed points of the deterministic piece of the system are $x = -\sqrt{2}$, 0, $\sqrt{2}$. There are two attractors, $x = \pm\sqrt{2}$, corresponding to the two minimums of $V(x)$, and one repeller, $x = 0$, corresponding to the local maximum of $V(x)$.

Initializing the system at fixed point $x = -\sqrt{2}$ corresponds to initializing the system in the left well of the potential function, illustrated by the red point in Figure 2.4(a). As time evolves, there are random fluctuations acting on the particle, in which a fluctuation can be strong enough to have the particle 'jump' out of the left well and into the right well of $V(x)$, where the right well corresponds to the fixed point $x = \sqrt{2}$. See Figure 2.4(b) for a time series solution. Notice in the time series that the stochastic realization is actually tipping back and forth between these two fixed points as time evolves.

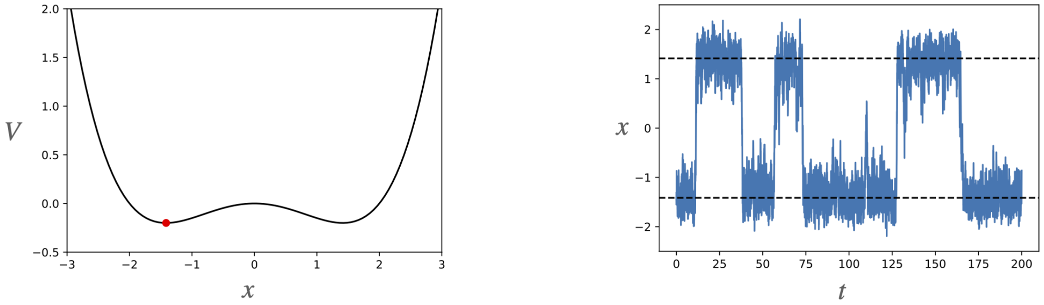

(a) (b)

Figure 2.4: (a) The potential function $V(x)$ for the system in (2.13). We demonstrate a particle (red circle), initialized at $x = -\sqrt{2}$ moving in the potential well under the influence of additive noise. (b) A stochastic realization of the particle position over time with $\sigma = 1.2$.

Example 2.2.3.

Consider the gradient, stochastic differential equation

$$\begin{aligned} dx &= -\nabla V(x)dt + \sigma dW_t \\ &= -\nabla \left(\frac{1}{4}x^4 - \frac{1}{3}x^3 - \frac{1}{2}x^2 \right) dt + \sigma dW_t \\ &= (-x + x^3 + x^2)dt + \sigma dW_t, \end{aligned} \tag{2.14}$$

where V is the associated potential function, as seen in Figure 2.5(a). The three fixed points of the deterministic piece of the system are $x = \frac{1\pm\sqrt{5}}{2}$ and $x = 0$. There are two attractors, $x = \frac{1\pm\sqrt{5}}{2}$, corresponding to the two minimums of $V(x)$, and one repeller, $x = 0$, corresponding to the local maximum of $V(x)$.

Initializing the system at fixed point $x = \frac{1-\sqrt{5}}{2}$ corresponds to initializing the system in the upper well of the potential function, illustrated by the red point in Figure 2.5(a). As time evolves, there are random fluctuations acting on the particle, in which a fluctuation can be strong enough to have the particle ‘jump’ out of the upper well and into the lower well, where the lower well corresponds to the fixed point $x = \frac{1+\sqrt{5}}{2}$. See Figure 2.5(b) for a time series solution.

Note that while it is possible to tip back to the other fixed point, it is extremely rare. This would require the particle to ‘jump’ out of the lower well and into the upper well, which requires a very strong fluctuation. Calculating the expected time to tip in this case, using the formula in (2.11), we find it is on the order of $O(10000)$.

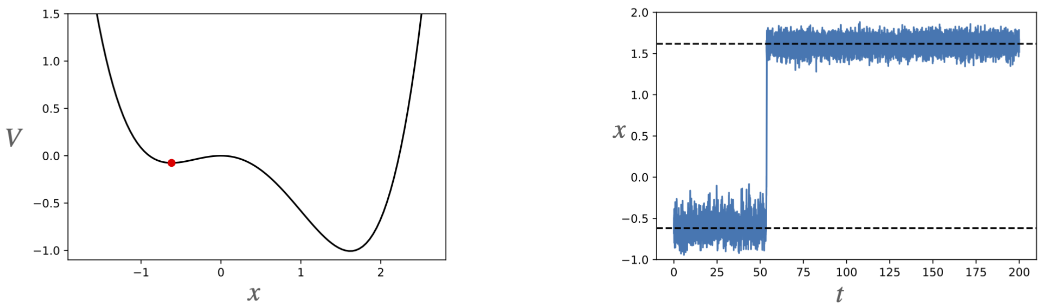

(a)

(b)

Figure 2.5: (a) The potential function $V(x)$ for the system in (2.14). We demonstrate a particle (red circle), initialized at $x = \frac{1-\sqrt{5}}{2}$ moving in the potential well under the influence of additive noise. (b) A stochastic realization of the particle position over time with $\sigma = 0.5$.

2.3 Rate-Induced vs. Noise-Induced Tipping

We conclude the background on rate and noise-induced tipping by comparing and contrasting the two mechanisms. Figure 2.6 demonstrates these two tipping mechanisms schematically, in terms of a potential function, and is referred to below.

Noise-induced tipping occurs when a noisy fluctuation is strong enough to push the particle out of the minimum and to some local maximum, where it can then fall to another minimum. Rate-induced tipping occurs when an external input varies too fast compared to the response rate of the system, resulting in a shift of the landscape and the deviation of a particle from its initialized stable state[41]. This starts the tracking of a different stable state.

For both tipping mechanisms, tipping occurs when a solution trajectory of the respective system crosses the threshold boundary (the boundary of the basin of attraction of the starting stable state). In a rate-induced tipping problem, the threshold boundary is associated with regular edge states, as defined in Chapter 1.3.1. In a noise-induced tipping problem, the threshold boundary is the local maximum separating two minima[9].

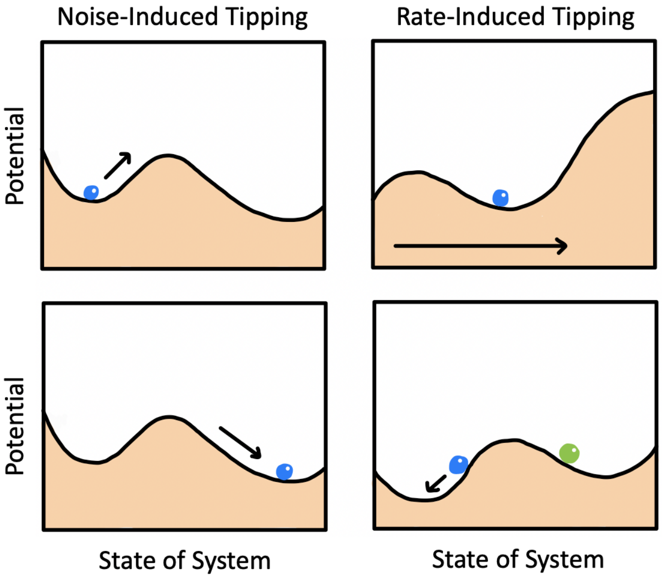

Figure 2.6: Schematics for noise and rate-induced tipping in terms of a potential function and initializing with a particle at a minimum.

CHAPTER 3

Methods for Stochastic Differential Equations

The theory of large deviations is utilized to find the most probable escape path and the expected time of escape. While these attributes are straight-forward to study in one-dimensional systems, they are harder to implement in higher dimensional systems. The framework for studying the effects of additive noise on the dynamics of a two-dimensional system is introduced, as well as how to find the most probable tipping path when tipping between two states.

The most probable path between two states should minimize the Freidlin-Wentzell action functional. Minimizing this functional works nicely if the initial and final states are both inside the basin boundary of the initial state, and neither are fixed points. If the paths involve fixed points, or cross basin boundaries, then there are complications. These situations occur when considering noise-induced tipping and are the focus of this work.

The minimization of the functional leads to the derivation of the Euler-Lagrange equations. The Euler-Lagrange equations for the extrema of the Freidlin-Wentzell function can be written as a Hamiltonian system, and these equations provide an underlying geometric context for the initial and threshold states. This framework can be exploited by finding unstable and stable manifolds of these states respectively. The intersections of these manifolds are heteroclinic orbits, which can then be used to find the most probable path of tipping or to isolate a subset of the unstable manifold. However, it is not enough to consider just the analytical perspective; numerical simulations are needed to corroborate the results.

Recall from Chapter 1.3.2 that the most probable path between two states can be thought of as the mode of the probability distribution of escape paths. It is helpful, and almost a necessity, to simulate large amounts of noisy realizations of the stochastic systems, and determine if and when they are meaningful. This chapter elaborates on techniques for numerically simulating stochastic differential equations as well as describing the process of finding converged sets of noisy realizations. The converged collection of noisy realizations can aid in determining how paths concentrate, where escape of a basin of attraction occurs, or finding the expected time for escape.

We note that the techniques provided in this chapter provide a basis for the rest of this dissertation.

3.1 The Theory of Large Deviations and the Freidlin-Wentzell Functional

Consider the system of stochastic differential equations given by

$$dx = f(x,y)dt + \sigma_1 dW_1,$$

$$dy = g(x,y)dt + \sigma_2 dW_2.$$

Assuming (3.1) has two stable states, the goal is to find the most probable path to tip between these two states, and the tool used to study these transitions is the Freidlin-Wentzell theory of large deviations.

As presented in Freidlin and Wentzell[23], the most probable path between two points (x_0, y_0) and (x_f, y_f) is a curve of the form $(c_1(t), c_2(t))$ that minimizes the Freidlin-Wentzell functional

$$I[c_1, c_2] = \int_{t_0}^{t_f} \left(\frac{(\dot{c_1} - f(c_1(t), c_2(t)))^2}{\sigma_1^2} + \frac{(\dot{c_2} - g(c_1(t), c_2(t)))^2}{\sigma_2^2} \right) dt, \tag{3.1}$$

over absolutely continuous functions from $[t_0, t_f]$ where

$$(c_1(t_0), c_2(t_0)) = (x_0, y_0) \text{ and } (c_1(t_f), c_2(t_f)) = (x_f, y_f).$$

$I[c_1, c_2]$ is nonnegative and vanishes if and only if both $\dot{c_1} = f$ and $\dot{c_2} = g$ are solutions to the associated deterministic system. This functional represents the cost of straying from the deterministic dynamics.

Minimizing this functional leads to the Euler-Lagrange equations, and satisfying the Euler-Lagrange equations is necessary but not sufficient for minimizers[23]. The most probable path must satisfy these equations, and so they form the basis to then perform further analysis, as the Euler-Lagrange equations allow the extrema of the Freidlin-Wentzell function to be written as a Hamiltonian system.

Of particular interest are the cases when (x_0, y_0) is a fixed point and (x_f, y_f) is either another fixed point or a periodic orbit. The formulation of the Freidlin-Wentzell functional suggests that the most probable path starting at the fixed point (x_0, y_0) should reach the final state in time $t_f - t_0$. This causes some complications: it turns out that there is not a minimizer defined on a bounded time domain. By Lemma 3.1 of Freidlin and Wentzell[23], this minimizer must lie inside the zero-set ($H = 0$) of the four-dimensional Hamiltonian system. The only path that starts at (x_0, y_0), and lies in $H = 0$, is on the unstable manifold of (x_0, y_0). Since a trajectory cannot reach the fixed point (x_0, y_0) in finite (backwards) time, the minimizer must lie on a domain that is at least semi-infinite. The strategy is to modify the process to instead consider a minimizing sequence that converges on a semi-infinite domain, though studying the Euler-Lagrange equations is still justified.

Since the minimizing trajectory must be smooth, it follows that it must be a heteroclinic orbit from (x_0, y_0) to (x_f, y_f). In particular, its domain will be $(-\infty, \infty)$ and it lies in both the unstable manifold of (x_0, y_0) and the stable manifold of (x_f, y_f) in the Hamiltonian system.

To derive the Euler-Lagrange equations, $(\bar{c_1}, \bar{c_2})$ is assumed to be a critical point of the Freidlin-Wentzell functional, where

$$\begin{aligned} c_1(t) &= \bar{c_1} + \varepsilon \delta c_1(t), \\ c_2(t) &= \bar{c_2} + \varepsilon \delta c_2(t), \end{aligned} \tag{3.2}$$

for $0 < \varepsilon \ll 1$. Assume $\delta c_1, \delta c_2 \in C^2[t_0, t_f]$, and that $\delta c_1(t_0) = \delta c_1(t_f) = \delta c_2(t_0) = \delta c_2(t_f) = 0$. The components $\varepsilon \delta c_i(t)$ are small perturbations of the critical point.

Let $F(\varepsilon) = I[\bar{c_1} + \varepsilon \delta c_1, \bar{c_2} + \varepsilon \delta c_2]$, and expand the functional form of $F(\varepsilon)$ to see

$$F(\varepsilon) = \int_{t_0}^{t_f} \frac{(\dot{\bar{c_1}} + \varepsilon \delta \dot{c_1} - f(\bar{c_1} + \varepsilon \delta c_1, \bar{c_2} + \varepsilon \delta c_2))^2}{\sigma_1^2} + \frac{(\dot{\bar{c_2}} + \varepsilon \delta \dot{c_2} - g(\bar{c_1} + \varepsilon \delta c_1, \bar{c_2} + \varepsilon \delta c_2))^2}{\sigma_2^2} dt. \tag{3.3}$$

Since $(\bar{c_1}(t), \bar{c_2}(t))$ is a critical point of I, it follows that $F'(0) = 0$ for all $\delta c_1, \delta c_2$. The calculations begin with differentiating (3.3) with respect to ε, resulting in an equation for $F'(\varepsilon)$ given by

$$\begin{aligned} F'(\varepsilon) = \int_{t_0}^{t_f} \bigg[&\frac{2}{\sigma_1^2} (\dot{\bar{c_1}} + \varepsilon \delta \dot{c_1} - f(\bar{c_1} + \varepsilon \delta c_1, \bar{c_2} + \varepsilon \delta c_2))(\delta \dot{c_1} - f_x \delta c_1 - f_y \delta c_2) \\ &+ \frac{2}{\sigma_2^2} (\dot{\bar{c_2}} + \varepsilon \delta \dot{c_2} - g(\bar{c_1} + \varepsilon \delta c_1, \bar{c_2} + \varepsilon \delta c_2))(\delta \dot{c_2} - g_x \delta c_1 - g_y \delta c_2) \bigg] dt. \end{aligned} \tag{3.4}$$

Rearranging (3.4),

$$\begin{aligned} F'(\varepsilon) = \int_{t_0}^{t_f} \bigg[&\frac{2}{\sigma_1^2} (\dot{\bar{c_1}} + \varepsilon \delta \dot{c_1} - f(\bar{c_1} + \varepsilon \delta c_1, \bar{c_2} + \varepsilon \delta c_2)) \delta \dot{c_1} \\ &+ \frac{2}{\sigma_1^2} (\dot{\bar{c_1}} + \varepsilon \delta \dot{c_1} - f(\bar{c_1} + \varepsilon \delta c_1, \bar{c_2} + \varepsilon \delta c_2))(-f_x \delta c_1 - f_y \delta c_2) \\ &+ \frac{2}{\sigma_2^2} (\dot{\bar{c_2}} + \varepsilon \delta \dot{c_2} - g(\bar{c_1} + \varepsilon \delta c_1, \bar{c_2} + \varepsilon \delta c_2)) \delta \dot{c_2} \\ &+ \frac{2}{\sigma_2^2} (\dot{\bar{c_2}} + \varepsilon \delta \dot{c_2} - g(\bar{c_1} + \varepsilon \delta c_1, \bar{c_2} + \varepsilon \delta c_2))(-g_x \delta c_1 - g_y \delta c_2) \bigg] dt. \end{aligned} \tag{3.5}$$

Expand $F'(\varepsilon)$, and then apply integration by parts twice to eliminate terms that have either $\delta \dot{c_1}$ and $\delta \dot{c_2}$ attached to the quantity. To use integration by parts, let

$$\begin{aligned} u &= \dot{\bar{c}}_1 + \varepsilon\delta\dot{c}_1 - f & \qquad\qquad & u = \dot{\bar{c}}_2 + \varepsilon\delta\dot{c}_2 - g \\ du &= [\ddot{\bar{c}}_1 + \varepsilon\delta\ddot{c}_1 - f_x\dot{c}_1 - f_y\dot{c}_2]dt & , \qquad & du = [\ddot{\bar{c}}_2 + \varepsilon\delta\ddot{c}_2 - g_x\dot{c}_1 - g_y\dot{c}_2]dt \\ v &= \delta c_1 & & v = \delta c_1 \\ dv &= \delta\dot{c}_1 dt & & dv = \delta\dot{c}_1 dt. \end{aligned} \tag{3.6}$$

Since $\delta c_1(t_0) = \delta c_1(t_f) = 0$ and $\delta c_2(t_0) = \delta c_2(t_f) = 0$, the boundary terms from the integration by parts vanish. Rearrange $F'(\varepsilon)$ by collecting δc_1 and δc_2 terms to see

$$\begin{aligned} F'(\varepsilon) = \int_{t_0}^{t_f} \Bigg[\Bigg(& \frac{2}{\sigma_1^2}(-\ddot{\bar{c}}_1 - \varepsilon\delta\ddot{c}_1 + f_x\dot{c}_1 + f_y\dot{c}_2 - \dot{\bar{c}}_1 f_x - \varepsilon\delta\dot{c}_1 f_x + ff_x) + \\ & \frac{2}{\sigma_2^2}(-\dot{\bar{c}}_2 g_x + \varepsilon\delta\dot{c}_2 g_x + gg_x)\Bigg)\delta c_1 + \Bigg(\frac{2}{\sigma_1^2}(-\dot{\bar{c}}_1 f_y - \varepsilon\delta\dot{c}_1 f_y + ff_y) + \\ & \frac{2}{\sigma_2^2}(-\ddot{\bar{c}}_2 - \varepsilon\delta\ddot{c}_2 + g_x\dot{c}_1 + g_y\dot{c}_2 - \dot{\bar{c}}_2 g_y - \varepsilon\delta\dot{c}_2 g_y + gg_y)\Bigg)\delta c_2\Bigg] dt. \end{aligned} \tag{3.7}$$

To find expressions for $\dot{c}_1$ and $\dot{c}_2$ differentiate (3.2), leading to

$$\begin{aligned} \dot{c}_1(t) &= \dot{\bar{c}}_1 + \varepsilon\delta\dot{c}_1, \\ \dot{c}_2(t) &= \dot{\bar{c}}_2 + \varepsilon\delta\dot{c}_2, \end{aligned} \tag{3.8}$$

and then (3.8) are substituted into (3.7). Making these substitutions and evaluating $F'(\varepsilon)$ at $\varepsilon = 0$ results in

$$\begin{aligned} F'(0) = \int_{t_0}^{t_f} \Bigg[& \left(\frac{2}{\sigma_1^2}(-\ddot{c}_1 + f_y\dot{c}_2 + ff_x) + \frac{2}{\sigma_2^2}(gg_x - \dot{c}_2 g_x)\right)\delta c_1 \\ & + \left(\frac{2}{\sigma_1^2}(ff_y - \dot{c}_1 f_y) + \frac{2}{\sigma_2^2}(-\ddot{c}_2 + gg_y + g_x\dot{c}_1)\right)\delta c_2\Bigg] dt. \end{aligned} \tag{3.9}$$

Remember that $(\bar{c_1}(t), \bar{c_2}(t))$ is a critical point of I, and so $F'(0) = 0$. It follows that (3.9) is zero for all curves $\delta c_1, \delta c_2$, and the resulting equations are

$$\begin{aligned} 0 &= \frac{2}{\sigma_1^2}(-\ddot{c}_1 + f_y\dot{c}_2 + ff_x) + \frac{2}{\sigma_2^2}(gg_x - \dot{c}_2 g_x), \\ 0 &= \frac{2}{\sigma_1^2}(ff_y - \dot{c}_1 f_y) + \frac{2}{\sigma_2^2}(-\ddot{c}_2 + g_x\dot{c}_1 + gg_y). \end{aligned} \tag{3.10}$$

These equations are rewritten as the Euler-Lagrange equations, given by

$$\begin{aligned} \ddot{c_1} &= f_y\dot{c_2} + ff_x + \frac{\sigma_1^2}{\sigma_2^2}(gg_x - \dot{c_2}g_x), \\ \ddot{c_2} &= g_x\dot{c_1} + gg_y + \frac{\sigma_2^2}{\sigma_1^2}(ff_y - \dot{c_1}f_y), \end{aligned} \tag{3.11}$$

which, to reiterate, are a condition that extrema of the Freidlin-Wentzell functional must satisfy. These Euler-Lagrange equations for extrema of (3.1) can be written as a Hamiltonian system, and this process is performed in later chapters as needed.

Depending on the source, there are multiple variations in the formulation of the Freidlin-Wentzell functional as seen in (3.1): some include the noise coefficient and some include a constant of 1/2. As these terms amount to multiplying the functional by a constant, the extrema of the function are still extrema when scaling them, and so there is no difference in the outcome. This choice of formulation does lead to different asymptotic formulae for the expected time to tip.

3.2 Numerically Solving Stochastic Differential Equations

To numerically simulate the stochastic differential equation expressed in (2.9), we use the Euler-Maruyama method, which gives rise to a discretized Markov process[24]. The Euler-Maruyama method creates the stochastic Euler scheme given by

$$x_{n+1} = x_n + f(x_n, \lambda)\Delta t + \sigma \Delta W_n, \tag{3.12}$$

where $\Delta t = t_{n+1} - t_n$ is the time increment and $\Delta W_n = W_{t_{n+1}} - W_{t_n}$ is the Brownian increment.

Implementing the map in (3.12) requires using properties of the Wiener process to numerically evaluate ΔW_n. Recall from Chapter 2.2 that the Brownian increments of the Wiener process are independent Gaussian random variables and normally distributed with mean zero and variance Δt, implying $\Delta W_n \sim N(0, \Delta t)$. In practice, a random number generator is used to draw noise values from this distribution and the stochastic Euler scheme becomes

$$\begin{aligned} x_{n+1} &= x_n + f(x_n, \lambda)\Delta t + \sigma \Delta W_n \\ &= x_n + f(x_n, \lambda)\Delta t + \sigma N(0, \Delta t). \end{aligned} \tag{3.13}$$

While it is possible to implement the scheme in (3.13), the size of the Brownian increment is not intuitive as $N(0, \Delta t)$ is not a standard normal distribution. Instead, we choose to numerically simulate $\Delta W = W_{t_{n+1}} - W_{t_n}$

using $\sqrt{\Delta t} \cdot N(0,1)$, so that the size of the Brownian increment is relative to a standard normal distribution. This transformation is justified by Claim 3.2.1 below, and the alternative scheme

$$\begin{aligned} x_{n+1} &= x_n + f(x_n,\lambda)\Delta t + \sigma \Delta W_n \\ &= x_n + f(x_n,\lambda)\Delta t + \sigma \sqrt{\Delta t} N(0,1), \end{aligned} \tag{3.14}$$

is implemented to numerically simulate (2.9).

Claim 3.2.1. *Let X be a normally distributed random variable with mean 0 and variance Δt, implying $X \sim N(0,\Delta t)$. Then $X \sim \sqrt{\Delta t} Z$ where $Z \sim N(0,1)$, and $N(0,\Delta t) = \sqrt{\Delta t} N(0,1)$.*

Proof. Suppose $X \sim N(\mu,\sigma^2)$. We standardize the normal distribution by introducing $Z = \frac{X-\mu}{\sigma}$, where Z is a standard normal random variable. Since Z is standard normal, $Z \sim N(0,1)$. Therefore, if $X \sim N(0,\Delta t)$ then $Z = \frac{X}{\sqrt{\Delta t}}$. Rearranging this equation, we see that $X = \sqrt{\Delta t} Z$, implying $X \sim \sqrt{\Delta t} Z$ and that $N(0,\Delta t) = \sqrt{\Delta t} N(0,1)$. $\square$

Recursively running the scheme in (3.14) over a defined time interval results in a single noisy realization. Implementing this scheme repeatedly to get a large amount of noisy realizations is the *Monte Carlo method*, in which repeated sampling is used until enough results are gathered to make up a representative sample of the behavior. The collection of these noisy realizations are used to visualize dominant behaviors of the stochastic system, including where trajectories concentrate, where trajectories may exit a set, or the expected time for trajectories to exit a set.

The behavior of the noisy realizations however, may not actually form a true representation of solutions to the system. It is necessary that the Monte Carlo simulations are a valid representation if we want to trust the numerical results of the behaviors mentioned above. To build confidence into these behaviors or events, a sufficiently large amount of Monte Carlo simulations are needed so that the event simulations converge.

The first step in this process is to consider the event outcomes as a probability distribution. The second step is to show the probability distribution of the event simulations converges. The probability distribution of the Monte Carlo simulations converges if more realizations added to the set of simulations does not change the statistics of the probability distribution of the event. To determine the convergence of a distribution, we first choose the event of the system that needs to be resolved. The algorithm for determining if an event has a converged distribution is as follows.

1. Run M simulations of a stochastic Euler scheme such as (3.14) on some time interval, and assume K events occur. Bin the K events by the Freedman Diaconis rule[22]. This separates the K events into B bins of equal length.

2. Run another M realizations of (3.14) on the same time interval and with the same step size. Assume there are J events. Bin the J events by the same number of bins B found in Step 1.

3. There are two vectors D_1, D_2 of the same dimension, where each component of the vector represents the amount of paths that tipped in that time interval. Calculate $Err = \frac{||D_1 - D_2||_2}{||D_1||_2}$, which is the relative error between the two data sets.

4. If $Err < 0.1$, then the distribution has converged. If $Err \geq 0.1$, iterate this process with larger M until the relative error of D_1 and D_2 is small enough. To iterate, double the number of samples and repeat this process. In addition, once $Err < 0.1$, use the Kolmogorov-Smirnov Two Sample Test[19] as a final verification that the distribution has converged.

The numerical methods described throughout this chapter are used to join the dynamical and stochastic perspectives in the later chapters. In Chapter 4, using the above convergence process, Monte Carlo simulations will show that the escape locations of the noisy trajectories match that of a special set of minimizers of the Freidlin-Wentzell functional. In Chapter 5, Monte Carlo simulations are used to find a numerical most probable path, as well as to find the expected time for noisy trajectories to tip over a basin boundary.

CHAPTER 4

Tipping in an Oceanic Carbon Cycle Model

The amount of carbon dioxide in the atmosphere is rising[32]. For a MIT news article[14], geophysicist and applied mathematician Daniel Rothman hypothesized:

> *By the end of this century, the planet is likely to reach a critical threshold, based on the rapid rate at which humans are adding carbon dioxide to the atmosphere. When we cross that threshold, we are likely to set in motion a freight train of consequences, potentially culminating in the Earth's sixth mass extinction.*

Rothman[38] presents a two-component dynamical system encompassing the important features of the oceanic carbon cycle, which describes the processes that exchange carbon between the ocean, atmosphere, and the continents. After analyzing the model, he discusses the implications of these findings for interpreting the geochemical record of past disruptions and predicting the carbon cycle's response to today's anthropogenic perturbations. Rothman determined when the CO_2 injection rate crossed a critical threshold value, it led to significant disruptions of the ancient earth system, including mass extinction events. He concluded that the injection rate is near that critical threshold.

The ocean absorbs much of the carbon dioxide; it is the largest sink of CO_2 on the planet. This addition of CO_2 causes ocean acidification, meaning the pH levels of the ocean are decreasing, causing difficulty for marine species and ecosystems (e.g. coral reefs) to survive. These species will either have to adapt to the changing ocean or risk extinction. Understanding the carbon cycle is of vital importance for our society as the preservation of these ecosystems and organisms are tied to fishing, industrial materials, and tourism industries[32]. These realizations, along with the results of Rothman's work, demonstrate the importance of understanding the carbon cycle and its underlying mechanisms.

Using Rothman[38] as motivation, Section 4.1 begins with the model description and looking at the regime of study. The regime chosen is bistable and exhibits a stable fixed point and a stable periodic orbit, separated by an unstable periodic orbit. Section 4.2 considers the deterministic system and the possibility of rate-induced tipping away from the stable fixed point when the system's parameter representing the injection of CO_2 is time-dependent. After considering basins of attraction of the stable fixed point and the stable periodic orbit, and choosing a correct parameter shift, the conditions of Theorem 2.1.4 are met, and the system undergoes tipping away from the stable fixed point.

After the deterministic analysis, Section 4.3 considers the effects of stochasticity on the state variables of the model in which the focus is noise-induced tipping from the stable fixed point to the stable periodic orbit. We only need to find a trajectory between the stable fixed point and the unstable periodic orbit, as after a trajectory reaches this boundary, the system will follow the deterministic flow. The emphasis of this work is to find local minimizers of the Freidlin-Wentzell functional on the semi-infinite domain $t \in (-\infty, t_f]$, where trajectories reach the unstable periodic orbit of the underlying deterministic system at $t = t_f$. Since ultimately we are looking for global minimizers for the small, but not vanishingly small noise regime, the extra step needed is the use of the *Onsager-Machlup functional*[13], a perturbation of the Freidlin-Wentzell functional, on the set of minimizers found. This extra consideration is not highlighted in this work but is discussed in Section 4.4.1. This analysis of the stochastic system is largely based on the analysis and the methods used in Fleurantin et al.[20] as the base structures are the same; the goal is to tip from a stable fixed point to an unstable periodic orbit.

The approach is as follows. The Euler-Lagrange equations associated with the Freidlin-Wentzell action functional are derived and then used to create a four-dimensional Hamiltonian system. This four-dimensional system changes the stability directions of the stable fixed point and unstable periodic orbit as compared to their stability in the original two-dimensional system. This change of stability allows us to find the invariant manifolds associated with these objects, and their intersections, resulting in two heteroclinic orbits. Using a geometric dynamical systems approach, there exists an isolated subset of the unstable manifold of the stable fixed point in the Euler-Lagrange system, which we call the *River*. Then using the Maslov index, a subset of the River can be further identified, which is comprised of local minimizers that escape the periodic orbit with minimal rotation. By Monte Carlo simulations, it is shown that this set of minimizers on the River matches closely the escape region of the simulated noisy trajectories at a certain level of small noise.

This process uses the Freidlin-Wentzell action functional to capture a phenomenon that is occurring at noise levels that are not vanishingly small. The key question becomes finding which parts of the theory hold true for small, but not vanishingly small, levels of noise, and how to best capture the behaviors exhibited by the system for these noise strengths.

For vanishingly small noise, this escaping behavior we foreshadow does not occur when tipping from a stable fixed point to an unstable periodic orbit. The work of Day[16] shows that as noise vanishes, there is no preferred exit point or region along an unstable periodic orbit, and that the most probable exit point exhibits cycling around the periodic orbit. However, for slightly larger noise strengths, this cycling is actually resisted.

4.1 The Original Model

4.1.1 Model Setup

Rothman[38] creates a simple dynamical system model of the marine carbon cycle given by

$$\begin{aligned} \dot{c} &= f(c)[\mu(1-bs(c,c_p)-\theta\bar{s}(c,c_x)-\nu)+w-w_0], \\ \dot{w} &= \mu[1-bs(c,c_p)+\theta\bar{s}(c,c_x)+\nu]-w+w_0, \end{aligned} \tag{4.1}$$

where $\dot{c}$ is the rate of change of the CO_3^{2-} concentration and $\dot{w}$ is the rate of change of the dissolved inorganic carbon concentration. The functions $f, s, \bar{s}$ are sigmodal functions modeling the buffering, burial, and respiration of the concentration of CO_3^{2-}, and are explicitly given by

$$\begin{aligned} f(c) &= \frac{f_0 c^\beta}{c^\beta + c_f^\beta}, \\ s(c,x) &= \frac{c^\gamma}{c^\gamma + x^\gamma}, \\ \bar{s}(c,x) &= 1 - s(c,x). \end{aligned} \tag{4.2}$$

Hence, substituting (4.2) into (4.1) results in the expanded system

$$\begin{aligned} \dot{c} = F(c,w) &= \frac{f_0 c^\beta}{c^\beta + c_f^\beta}\left[\mu\left(1-\frac{bc^\gamma}{c^\gamma+c_p^\gamma}-\theta\left(1-\frac{c^\gamma}{c^\gamma+c_x^\gamma}\right)-\nu\right)+w-w_0\right], \\ \dot{w} = G(c,w) &= \mu\left(1-\frac{bc^\gamma}{c^\gamma+c_p^\gamma}+\theta\left(1-\frac{c^\gamma}{c^\gamma+c_x^\gamma}\right)+\nu\right)-w+w_0. \end{aligned} \tag{4.3}$$

This model assumes a well-mixed ocean, implying the timescales considered must be larger than approximately 1000 years, which are the timescales necessary for global ocean mixing: in (4.3), time is nondimensionalized by $t = t/\tau_w$, where $\tau_w = 1000$. Keep in mind that this model does not account for effects that arise on shorter timescales. The other parameters, along with their descriptions, values, and units, are listed in Table 4.1.1.

In Rothman[38], only μ, b, θ, c_x, c_p, and ν were of interest, and the remaining 5 parameters were set to correspond to the equilibrium chemistry or the properties of the modern ocean in order to maintain realism. For the purposes of this work, the parameters of focus are c_x and ν. The parameter c_x is considered in regards

Parameter	Value	Units	Description
b	4	-	maximum $CaCO_3$burial rate
β	1.70	-	sigmoid sharpness index
c_f	43.9	μmol kg^{-1}	crossover [CO_3^{2-}] (buffering)
c_p	110	μmol kg^{-1}	crossover [CO_3^{2-}] (burial)
c_x	58	μmol kg^{-1}	crossover [CO_3^{2-}] (respiration)
f_0	0.694	-	maximum buffer factor
γ	4	-	sigmoid sharpness index
μ	250	μmol kg^{-1}	characteristic concentration $j_{in}\tau_w$
ν	0.1	-	CO_2 injection rate
τ_w	10^4	year	characteristic timescale
θ	5	-	maximum respiration feedback rate
w_0	2000	μmol kg^{-1}	reference DIC concentration

Table 4.1: Parameters of the oceanic carbon cycle model (4.3) and their values.

to showing different system behaviors and is also the bifurcation parameter. Later, the parameter ν is changed into a time-dependent parameter instead of staying a fixed value.

4.1.2 Parameter Regimes, Fixed Points, and a Bifurcation Analysis

The fixed points of (4.3) occur where $\dot{c} = \dot{w} = 0$, implying the unique steady-state solution (c^*, w^*) is

$$\begin{aligned} c^* &= c_p(b-1)^{-1/\gamma}, \\ w^* &= w_0 + \mu\left(\theta + \nu - \frac{\theta c_p^\gamma}{c_p^\gamma + (b-1)c_x^\gamma}\right). \end{aligned} \tag{4.4}$$

System (4.3) is linearized about this fixed point (c^*, w^*) from (4.4) using the Jacobian matrix

$$J(c^*, w^*) = \begin{pmatrix} F_c & F_w \\ G_c & G_w \end{pmatrix}, \tag{4.5}$$

where the partial derivatives F_c, F_w, G_c, and G_w are defined as

$$\begin{aligned} F_c &= \frac{f_0 c^{\beta-1}}{(c^\beta + c_f^\beta)^2}\left[\beta c_f^\beta \left(w - w_0 + \mu\left(1 - \frac{bc^\gamma}{c^\gamma + c_p^\gamma} - \frac{\theta c_x^\gamma}{c^\gamma + c_x^\gamma} - \nu\right)\right)\right. \\ &\qquad \left. - \mu\gamma c^\gamma (c^\beta + c_f^\beta)\left(\frac{bc_p^\gamma}{(c^\gamma + c_p^\gamma)^2} - \frac{\theta c_x^\gamma}{(c^\gamma + c_x^\gamma)^2}\right)\right], \qquad (4.6) \\ F_w &= \frac{f_0 c^\beta}{c^\beta + c_f^\beta}, \end{aligned}$$

$$G_c = -\mu \gamma c^{\gamma-1} \left(\frac{b c_p^\gamma}{(c^\gamma + c_p^\gamma)^2} + \frac{\theta c_x^\gamma}{(c^\gamma + c_x^\gamma)^2} \right),$$

$$G_w = -1.$$

The eigenvalues of $J(c^*, w^*)$ are complex conjugate pairs, and as c_x increases, these eigenvalues cross the imaginary axis. This crossing of the imaginary axis implies the system undergoes a Hopf bifurcation when the real part of the eigenvalues of $J(c^*, w^*)$ are zero. See Figure 4.1 for a depiction of the shift in eigenvalues.

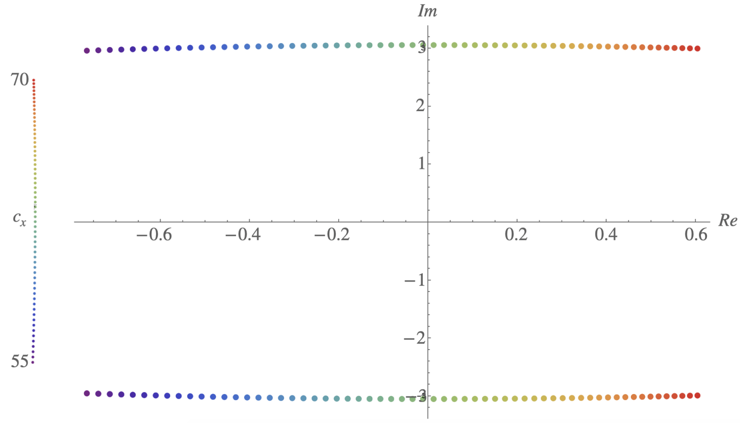

Figure 4.1: The eigenvalues of $J(c^*, w^*)$ for varying values of $c_x \in [55, 70]$, with a step size of 0.25. When the eigenvalues cross the imaginary axis at $c_x \approx 62.6$, the system undergoes a Hopf bifurcation.

A bifurcation analysis is needed to further understand the possible solution behaviors that system (4.3) can exhibit. Using MatCont[18], a Matlab software project that provides a toolbox for the numerical continuation and bifurcation study of continuous and discrete parameterized dynamical systems, we create the bifurcation diagram seen in Figure 4.2.

There are three different system behaviors dependent on the parameter regime chosen, within realistic values of c_x. From the bifurcation diagram in Figure 4.2, it follows that there can be a stable fixed point, an unstable fixed point and stable periodic orbit, or a stable fixed point and a stable periodic orbit separated by an unstable periodic orbit. See Figure 4.3 for an illustration of the phase planes of these three dynamical regimes. In Sections 4.2 and 4.3, the focus is on the regime in which there is bistability.

This bistable regime, where the parameter values are set as in Table 4.1.1, corresponds to Figure 4.3b. Let z^* denote the fixed point (c^*, w^*), let Γ_u denote the unstable periodic orbit, and let Γ_s denote the stable periodic orbit.

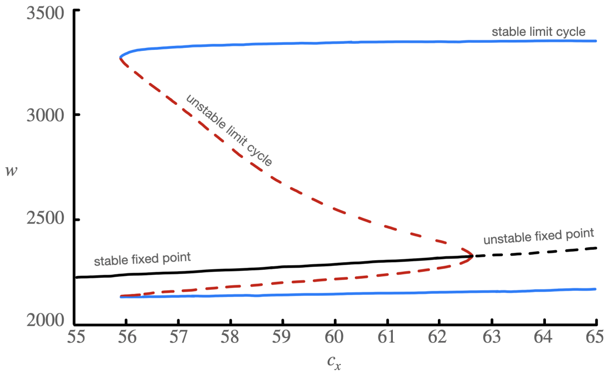

Figure 4.2: Bifurcation diagram for the parameter c_x. The solid blue lines indicates the maximum and minimum values of w in the stable periodic orbit and the dashed red lines represents the same extremes for the unstable periodic orbit. The black solid line indicates the stable fixed point while the black dashed line indicates the unstable fixed point. The subcritical Hopf bifurcation occurs at $c_x \approx 62.6$. A saddle-node bifurcation of cycles occurs where the unstable and stable limit cycles collide at $c_x \approx 55.9$.

The fixed point is explicitly given by

$$z^* = (83.58192542167518, 2260.2904217603455), \tag{4.7}$$

and the linearzation at (4.7) is

$$J(z^*) = \begin{pmatrix} 0.08712628 & 0.51998416 \\ -18.11401945 & -1 \end{pmatrix}. \tag{4.8}$$

The eigenvalues of the matrix in (4.8) are given by

$$\lambda_{1,2} = -0.456437 \pm 3.02052i, \tag{4.9}$$

implying the fixed point (4.7) is a stable spiral. In the two-dimensional system, z^* and Γ_s have two stable directions, implying they each have a two-dimensional stable subspace, and Γ_u has one unstable direction and one neutral direction, implying it has a one-dimensional unstable subspace. Floquet multipliers are used to find the stability of the periodic orbits.

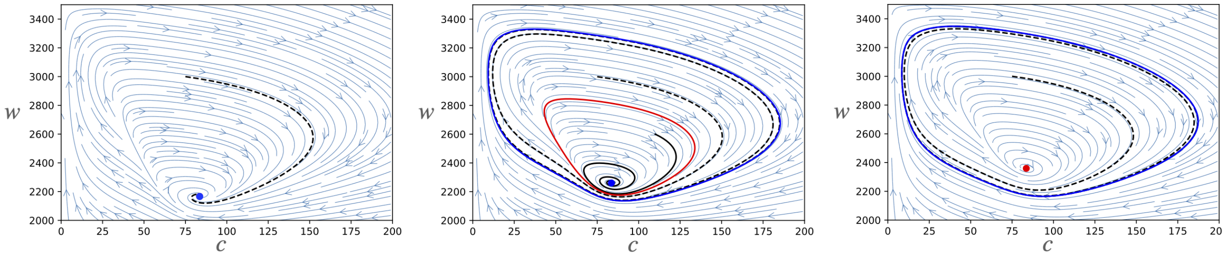

(a) (b) (c)

Figure 4.3: Phase planes of system (4.3) with all parameters set as in Table 4.1.1, except allowing c_x to vary. Stable states are in blue and unstable states are in red. Black solid and dashed curves represent single solution trajectories. (a) $c_x = 55$: There is a stable fixed point. (b) $c_x = 58$: There is a stable periodic orbit and a stable fixed point separated by an unstable periodic orbit. (c) $c_x = 65$: There is a stable periodic orbit and an unstable fixed point.

4.2 The Addition of a Time-Varying Parameter

4.2.1 Creating the Ramped Parameter and the Susceptibility to R-Tipping

Introducing a parameter shift to replace ν allows the CO$_2$ injection rate to vary in time. We create a monotonically increasing bi-asymptotically constant $\Lambda_r(t)$ given by

$$\Lambda_r(t) = \nu_- + \frac{\nu_+ - \nu_-}{2}(1 + \tanh(rt)), \tag{4.10}$$

in which $\Lambda_r(t)$ will gradually transition from ν_- to ν_+. After making this substitution, (4.1) is a nonautonomous system of the form

$$\begin{aligned} \dot{c} &= f(c)[\mu(1 - bs(c,c_p) - \theta\bar{s}(c,c_x) - \Lambda_r(t)) + w - w_0], \\ \dot{w} &= \mu[1 - bs(c,c_p) + \theta\bar{s}(c,c_x) + \Lambda_r(t)] - w + w_0. \end{aligned} \tag{4.11}$$

As mentioned earlier, the parameter values were chosen such that there is a stable fixed point and a stable periodic orbit separated by an unstable periodic orbit. The unstable periodic orbit forms the boundary between the basins of attraction for the stable fixed point and the stable limit cycle. Let p_-, Γ_{u^-}, and Γ_{s^-} represent the stable fixed point, unstable periodic orbit, and the stable periodic orbit at the past limit state ν_-. Let p_+, Γ_{u^+}, and Γ_{s^+} represent the stable fixed point, unstable periodic orbit, and the stable periodic orbit at the future limit state ν_+. For rate-induced tipping to occur within system (4.11) for this parameter shift, $(p_-, \nu_-) \in \mathbb{B}(\Gamma_{s^+}, \nu_+)$, by the conditions of Theorem 2.1.4.

This condition is checked visually in Figure 4.4. In this figure, the past limit state is set at $\nu_- = 0$ and we plot the corresponding stable fixed point p_-. We also plot the unstable periodic orbit Γ_{u^+} for different possible values of the future limit state ν_+. For rate-induced tipping to occur, it is necessary that $(p_-,0) \in \mathbb{B}(\Gamma_{s^+},\nu_+)$, implying that p_- must be on the outside of Γ_{u^+}. For $\nu = 0.4$, this transition occurs and the carbon cycle model is susceptible to rate-induced tipping away from p_-.

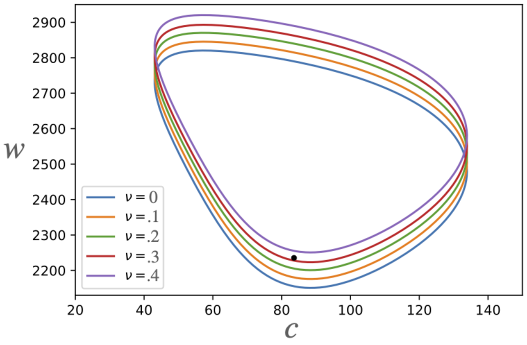

Figure 4.4: The stable fixed point p_- (black circle) of (4.11) at the past limit state $\nu_- = 0$, plotted against the unstable periodic orbit Γ_{u^+} at the future limit state ν_+ for varying values. Crossing of the basin of attraction boundary occurs as $(p_-,0) \in \mathbb{B}(\Gamma_{s^+},0.4)$, implying there will be rate-induced tipping away from p_-.

4.2.2 Numerical Results

From the analysis in Section 4.2.1, (4.10) becomes

$$\Lambda_r(t) = 0.2(1+\tanh(rt)), \tag{4.12}$$

which gradually transitions from 0 to 0.4 in time. To convert system (4.11) back to an autonomous system, it is augmented using Approach 1 from Section 2.1, resulting in the system given by

$$\begin{aligned} \dot{c} &= f(c)[\mu(1-bs(c,c_p)-\theta\bar{s}(c,c_x)-\Lambda_r(s))+w-w_0], \\ \dot{w} &= \mu[1-bs(c,c_p)+\theta\bar{s}(c,c_x)+\Lambda_r(s)]-w+w_0, \\ \dot{s} &= 1. \end{aligned} \tag{4.13}$$

Initializing system (4.13) at p_-, and numerically simulating (4.13) for increasing values of r, shows how solution behaviors change as r changes. In Figure 4.5, notice that for sufficiently large values of r the system tips, and for sufficiently small values of r the system does not tip. This shows that the rate at which ν is varied determines whether the system tips, implying the existence of a critical rate, r_c, and above which tipping

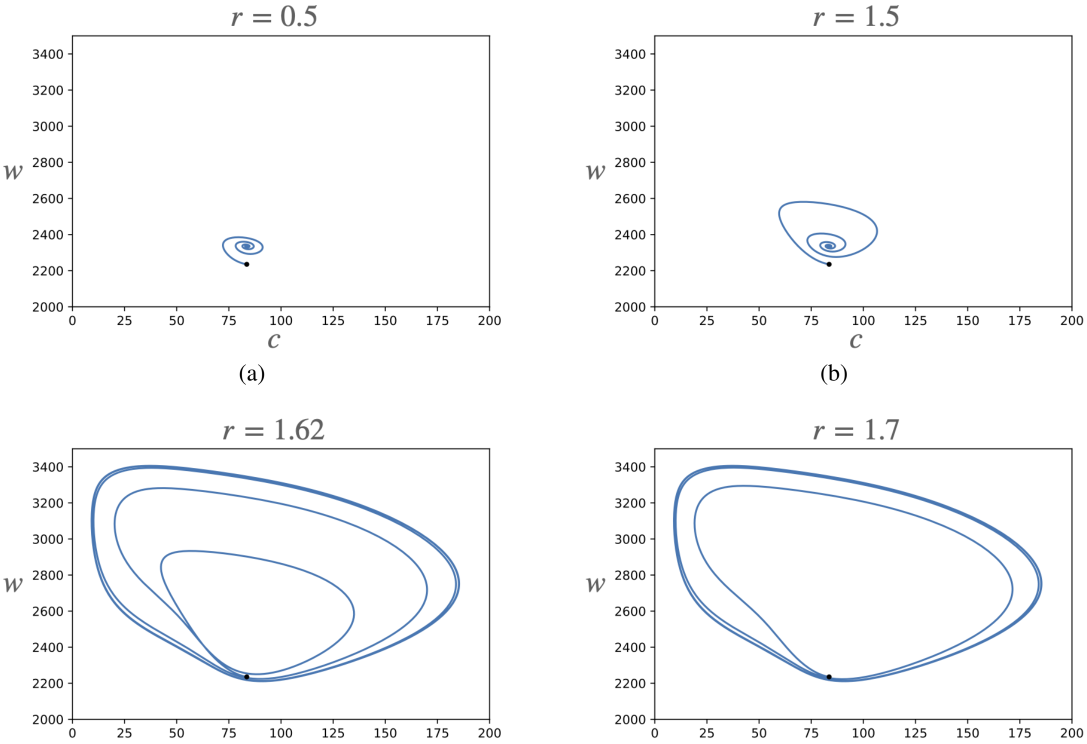
$r = 0.5$

$r = 1.5$

$r = 1.62$

$r = 1.7$

(a) (b) (c) (d)

Figure 4.5: The two-dimensional viewpoint. Solution behaviors (blue) of system (4.13) for varying values of r. The system is initialized at p_- (black circle). (a) $r = 0.5$: No tipping occurs as the solution end-point tracks p_+. (b) $r = 1.5$: No tipping occurs as the solution end-point tracks p_+. (c) $r = 1.62$: Rate-induced tipping occurs away from p_- as the solution escapes the basin of attraction of p_- and relaxes to Γ_{s^+}. (d) $r = 1.7$: Rate-induced tipping occurs away from p_- as the solution escapes the basin of attraction of p_- and relaxes to Γ_{s^+}.

occurs. The behaviors for the cases $r = 1.5$ and $r = 1.62$ are also illustrated in three-dimensional space in Figure 4.6.

The main goal was to show that the system is susceptible to rate-induced tipping, not to find r_c, though at $r = r_c$, there is an orbit connecting the stable fixed point p^- to the unstable periodic orbit Γ_{u^+}.

In conclusion, if the CO_2 injection rate ν is a time-dependent parameter, and if it varies fast enough, the system does in fact cross over from the basin of attraction of the fixed point to that of the stable periodic orbit. Therefore, the system can tip between states before the actual loss of stability of the fixed point. Physically this implies that the amounts of carbonate and dissolved inorganic carbon could change drastically in a relatively short time, affecting the oceans and their current balance.

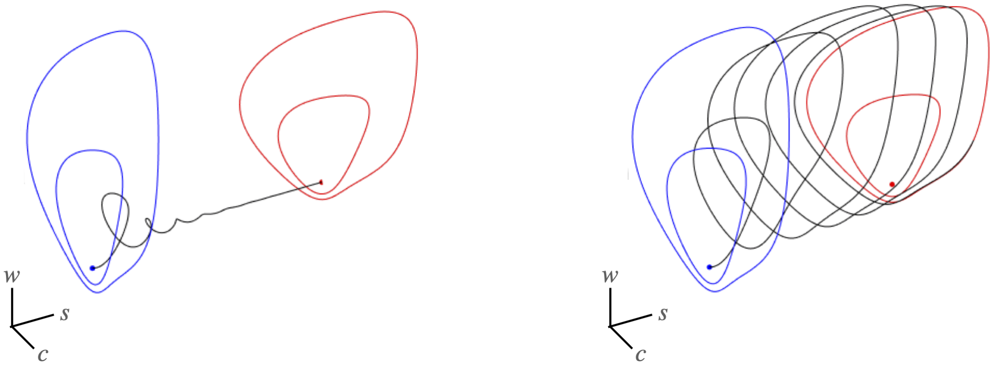

(a) (b)

Figure 4.6: The three-dimensional viewpoint. Solution behaviors (black) of system (4.13) for varying values of r, where the past limit system is in blue and the future limit system is in red. The system is initialized at p_- (blue circle). (a) $r = 1.5$: No tipping occurs as the solution end-point tracks p_+. (b) $r = 1.62$: Rate-induced tipping occurs away from p_- as the solution escapes the basin of attraction of p_- and relaxes to Γ_{s^+}.

4.3 The Stochastic Version of the Model

Instead of considering the addition of a ramp parameter, we now look at the addition of additive white noise on the dynamics of c and w. Looking at numerically simulated noisy trajectories to gain an initial understanding of the stochastic behavior, there seems to be a clear location on Γ_u that the trajectories concentrate around when tipping away from the stable fixed point, as seen in Figure 4.7.

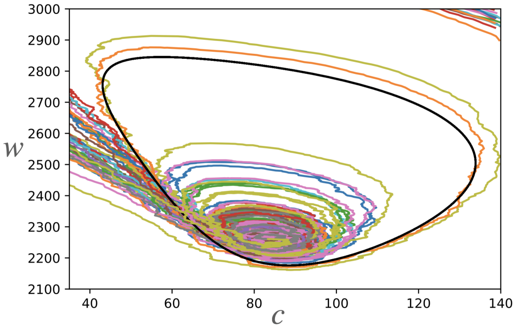

Figure 4.7: Realizations (colored trajectories) of (4.15) that escape the unstable periodic orbit (black) on the time interval $[0, 15]$ with noise strength $\sigma_1 = \sigma_2 = 5$. Once they have escaped, they follow the stable periodic orbit (not pictured).

4.3.1 The Initial Setup and the Most Probable Path Equations

Consider the system given by

$$\begin{aligned} dc &= F(c,w)dt + \sigma_1 dW_1, \\ dw &= G(c,w)dt + \sigma_2 dW_2, \end{aligned} \tag{4.14}$$

where $F(c,w)$ and $G(c,w)$ are as given in (4.3), and we set $\sigma_1 = \sigma_2$ for mathematical simplification. Recall the regime of focus is bistable and the parameters are set as they are in Table 4.1.1. The goal is to tip from the stable fixed point to the stable periodic orbit. From Freidlin-Wentzell theory, the system will tip with probability one, but it needs to be determined how and on what timescale. The approach is to consider the most probable path for tipping from the stable fixed point to the unstable periodic orbit, as the system will follow the deterministic flow once it reaches the basin boundary.

The theory of large deviations says that the most probable paths of escape from the attracting fixed point through the unstable periodic orbit should minimize (3.1). Using the methods described in Section 3.1, the general Euler-Lagrange equations (3.11) derived in Section 3.1 become

$$\begin{aligned} \ddot{c} &= F_w\dot{w} + FF_c + GG_c - \dot{w}G_c, \\ \ddot{w} &= G_c\dot{c} + GG_w + FF_w - \dot{c}F_w, \end{aligned} \tag{4.15}$$

for the stochastic carbon cycle model, assuming $\sigma_1 = \sigma_2$. Using the Euler-Lagrange equations in (4.15), we make a Legendre transform^4 to create a degree four Hamiltonian system. Let

$$\begin{aligned} p &= \dot{c} - F, \\ q &= \dot{w} - G. \end{aligned} \tag{4.16}$$

Differentiating p and q with respect to t,

$$\begin{aligned} \dot{p} &= \ddot{c} - F_c\dot{c} - F_w\dot{w}, \\ \dot{q} &= \ddot{w} - G_c\dot{c} - G_w\dot{w}. \end{aligned} \tag{4.17}$$

Substituting $\ddot{c}$ into $\dot{w}$ and $\ddot{y}$ into $\dot{q}$ from (4.15), (4.17) becomes

$$\begin{aligned} \dot{p} &= (F_w\dot{w} + FF_c + GG_c - \dot{w}G_c) - F_c\dot{c} - F_w\dot{w} \\ &= FF_c + GG_c - (G+q)G_c - F_c(F+p) \\ &= -F_cp - G_cq, \\ \dot{q} &= (G_c\dot{c} + GG_w + FF_w - \dot{c}F_w) - G_c\dot{c} - G_w\dot{w} \end{aligned} \tag{4.18}$$

$$= GG_w + FF_w - (F+p)F_w - G_w(G+q)$$
$$= -F_w p - G_w q.$$

The Euler-Lagrange equations as a Hamiltonian system then reads as

$$\begin{aligned}
\dot{x} &= F + p, \\
\dot{y} &= G + q, \\
\dot{p} &= -F_c p - G_c q, \\
\dot{q} &= -F_w p - G_w q,
\end{aligned} \tag{4.19}$$

where the Hamiltonian is given by

$$H(c,w,p,q) = F(c,w)p + G(c,w)q + \frac{p^2+q^2}{2}. \tag{4.20}$$

Notice $p = q = 0$ is invariant. These invariant planes carry the deterministic flow given by system (4.3). The fixed point z^* and periodic orbits Γ_u and Γ_s reappear with their attraction and repulsion reproduced. We slightly abuse notation to allow the same notation of z^*, Γ_u, and Γ_s for the fixed point and the unstable and stable periodic orbits, respectively, in reference to both Equations (4.3) and (4.19), as the p and q components are just zero. While the notation stays the same, notice that their stability properties change between the two-dimensional system in (4.3) and the four-dimensional system (4.19). This is the reason for using system (4.19) for determining the most probable paths of escape from z^* out of its basin of attraction, and to Γ_u.

The stability of z^*, Γ_u, and Γ_s were determined for the two-dimensional system, and now it is necessary to determine their stability in the four-dimensional system. The Jacobian matrix for the linearized flow of (4.19) is given by

$$J(c,w,p,q) = \begin{pmatrix} F_c & F_w & 1 & 0 \\ G_c & G_w & 0 & 1 \\ -F_{cc}p - G_{cc}q & -F_{cw}p - G_{cw}q & -F_c & -G_c \\ -F_{wc}p - G_{wc}q & -F_{ww}p - G_{ww}q & -F_w & -G_w \end{pmatrix}, \tag{4.21}$$

which actually evaluated at z^* is

$$J(z^*) = \begin{pmatrix} 0.08712628 & 0.51998416 & 1 & 0 \\ -18.11401945 & -1 & 0 & 1 \\ 0 & 0 & -0.08712628 & 18.11401945 \\ 0 & 0 & -0.51998416 & 1 \end{pmatrix}. \tag{4.22}$$

The eigenvalues of this matrix are given by

$$\begin{aligned} \lambda_{1,2} &= -0.456437 \pm 3.02052i, \\ \lambda_{3,4} &= \quad 0.456437 \pm 3.02052i, \end{aligned} \tag{4.23}$$

where $\lambda_{3,4}$ are the eigenvalues associated with the unstable eigenvectors that span the two-dimensional unstable subspace. The corresponding eigenvectors are given by

$$v_{3,4} = \begin{pmatrix} -.415332954257906 \pm 3.614767708743985i \\ 18.692389481011410 \mp 6.191296365829346i \\ 1.045345562758857 \pm 5.808869622205990i \\ 1 \pm 0i \end{pmatrix}. \tag{4.24}$$

Notice that $\lambda_{1,2}$ are exactly the eigenvalues of (4.8), and correspond to the two-dimensional stable subspace of the fixed point z^* in (4.19), as well as the deterministic flow of (4.3). From the above analysis, the unstable manifold of z^*, denoted by $W^u(z^*)$, is two-dimensional.

Technically, Γ_u has one stable, two neutral, and one unstable Floquet multipliers. These can be found numerically or determined using the fact that for a Hamiltonian system with two degrees of freedom, there are two neutral Floquet exponents and two that are reciprocals of one another. It may seem as though Γ_u should have a one-dimensional stable manifold, but integrating this one-dimensional stable direction results in a tangent bundle, which will be a two-dimensional manifold. It follows that Γ_u has both a two-dimensional stable subspace and a two-dimensional unstable subspace in (4.19), where the two-dimensional unstable subspace aligns with that of the deterministic flow of (4.3).

Both the unstable manifold of z^* and stable manifold of Γ_u lie in $\mathbb{R}^4$, in the complement of the deterministic plane, and will aid in determining the most probable path, as the transverse intersections of $W^u(z^*)$ and $W^s(\Gamma_u)$ are the heteroclinic orbits. $W^u(z^*)$ will be of special importance in later sections.

4.3.2 Computing the Unstable Manifold

$W^u(z^*)$ is computed as follows. We first find a piece of the local unstable manifold, $W^u_{loc}(z^*)$. Take the fixed point $z^* \in \mathbb{R}^4$, corresponding to a time of negative infinity, where the linearized system about z^* has eigenvectors $v_{3,4}$ corresponding to the two eigenvalues with positive real part $\lambda_{3,4}$. Then, we initialize using

$$\psi = z^* + \theta_1 v_1 + \theta_2 v_2, \tag{4.25}$$

where $|\theta_1|^2 + |\theta_2|^2 = \varepsilon^2$, and ε scales how close the initialization is to the fixed point z^*. As $v_3 = \bar{v_4}$, it is necessary that $\theta_1 = \bar{\theta}_2$ in order to keep components real by applying the conjugate. Let

$$\begin{aligned} \theta_1 &= \varepsilon(\cos(x) + i\sin(x)) \\ \theta_2 &= \varepsilon(\cos(x) - i\sin(x)) \end{aligned} \tag{4.26}$$

where $0 \le x \le 2\pi$. As $x \in [0, 2\pi]$ varies, a collection of ψ values is created, which together form a circle of points that lie in $W^u_{loc}(z^*)$. Call this set K. See Figure 4.10(a) for a depiction of K.

The global unstable manifold is generated by initiating trajectories from circle K inside the local unstable manifold. (4.19) is numerically simulated using each point on K as an initial condition, and the union of the set of these full trajectories form $W^u(z^*)$. With exception of the heteroclinic orbits, the only trajectories of interest are those that reach the unstable periodic orbit Γ_u in finite time. Therefore, it is not necessary to integrate over too long a time period and we focus on the finite portion of $W^u(z^*)$ that reaches just past the boundary of Γ_u. See Figure 4.7(a) for a visualization of $W^u(z^*)$.

4.3.3 Computing the Stable Manifold

$W^s(\Gamma_u)$ is computed as follows. First, the period of Γ_u, T, needs to be determined. The periodic orbit Γ_u is discretized into $N+1$ points Γ_{u_k}, where $0 \le k \le N$. For each point, there corresponds a time along the period τ_k such that $\Gamma_{u_k} = \Gamma_{u_{\tau_k}}$. Note that it does not matter the location of the start point.

Then, the *monodromy matrix*, which is the state transition matrix ϕ after one period, is found for $k = 0$. Let ξ_{s_0} be the eigenvector associated with the stable eigenvalue of the monodromy matrix, where the stable eigenvalue $\lambda \in (0, 1)$. This vector ξ_{s_0} is tangent to the stable manifold at Γ_0. The stability type of the state transition matrix of any point Γ_k on the periodic orbit is independent of k, and the eigenvectors can be computed if the state transition matrix is known at a base point Γ_0. It will be the eigenvector of the monodromy matrix computed at Γ_0, multiplied by the state transition matrix of the new point Γ_k at its associated time τ_k. Formally this is written as

$$\xi_{s_k} = \phi(0,\tau_k)\xi_{s_0}. \tag{4.27}$$

So, for each point Γ_k, the state transition matrix $\phi(0,\tau_k)$ is computed to obtain the tangent space to the stable manifold at the point with (4.27). The collection of these ξ_{s_k} form a tangent bundle.

A tolerance ε is chosen, where ε scales how close the initialization is to the periodic orbit. For small enough ε,

$$x_{s_k} = \Gamma_k + \varepsilon\xi_{u_k} \tag{4.28}$$

are points in the stable subspace of Γ_u. This set of initial conditions (4.28) is integrated in backwards time over some time interval, obtaining the orbits $x_{s_k}(t)$. The collection of these orbits form the global stable manifold of Γ_u. See Figure 4.7(b) for a visualization of $W^s(\Gamma_u)$.

4.3.4 Finding the Heteroclinic Orbits

Now that there are approximations of $W^u(z^*)$ and $W^s(\Gamma_u)$, it is possible to find the heteroclinic orbits. The heteroclinic orbits are found through the intersections of these invariant manifolds. We expect these intersections to be transverse, which is why they can be found computationally.

To actually achieve finding these intersections, an algorithm to find sets of closest points (one on $W^u(z^*)$ and the other on $W^s(\Gamma_u)$) is used. The algorithm for finding a set of closest points is as follows.

1. Restructure both the unstable and stable manifold datasets into two dataframes with columns of c, w, p, q.
2. Create a BallTree for the stable manifold, which partitions its dataframe into a nested set of balls. The resulting data structure has characteristics that make it useful for a nearest neighbor search.
3. Query the tree to find its nearest neighbor within the unstable manifold dataframe, and return the distance between, and the IDs, of the two points.
4. Sort by the shortest distance.

Initially the heteroclinic orbits are computed using these sets of points, where the point on $W^s(\Gamma_u)$ is integrated forward in time towards Γ_u, and the point on $W^u(z^*)$ is integrated backwards in time towards z^*. The tangency of the two trajectories has to be verified to ensure that two points actually have trajectories tangent to one another, and not intersecting one another or meeting at a cusp. This process is performed by inspection of the integration near the intersection point. Once it is determined that they fall on the same path, the trajectory integrated backwards in time is used to find its corresponding point on the parameterized circle K. The initialized points on K correspond to angles in $[0,2\pi]$. Using this process, two heteroclinic orbits are found: $\mathscr{H}_1$ and $\mathscr{H}_2$. This implies there are two initial points on K, corresponding to two angles $x_1, x_2 \in [0,2\pi]$.

The invariant manifolds are illustrated in (c,w,q) space in Figure 4.8(a) and Figure 4.8(b). An overlap of the invariant manifolds with their transverse intersections, as well as the heteroclinic orbits themselves are illustrated in (c,w,q) space in Figure 4.8(c) and Figure 4.8(d). For other images of the heteroclinic orbits, see Figure 4.11(a) and 4.11(c) for two-dimensional projections, or Figure 4.12(a) for a different three-dimensional view, projected into (c,w,q) space, without the invariant manifolds overlaid.

4.3.5 The River

Recall, there are two heteroclinic orbits, $\mathscr{H}_1$ and $\mathscr{H}_2$, connecting z^* and Γ_u. As mentioned in Section 4.3.4, the heteroclinic orbits $\mathscr{H}_1$ and $\mathscr{H}_2$ are associated with two points on K, which correspond to two angles x_1 and x_2 respectively, from the initialization process. The angles x_1 and x_2 divide the circle $K \subset W^u(z^*)$ into two arcs of points. From Lemma 2.3 in Fleurantin et al.[20], there are angles x near angle x_1 for which the associated trajectories pass over Γ_u, and so they are considered exit trajectories. These exit trajectories correspond to x values between x_1 and x_2, and most exit with minimal rotation.

All trajectories with angles between x_1 and x_2 exit Γ_u. This implies that every trajectory associated with angles $x \in (x_1, x_2)$ crosses Γ_u when projected into (c,w) space. The River, formally defined below, is used to describe the set of trajectories on $W^u(z^*)$ that cross Γ_u with x values between x_1 and x_2. The heteroclinic orbits $\mathscr{H}_1$ and $\mathscr{H}_2$ form the banks of the River. It is expected that between the two heteroclinics $\mathscr{H}_1$ and $\mathscr{H}_2$, part of the River will leak out. Using the Maslov index, a subset of the River can be further identified, called the subriver. The definitions of the Maslov Index and the subriver are below.

Definition 4.3.1. Let Z be a trajectory $z(t)$ for $t \in (-\infty, t_f]$ satisfying (4.19). The *River*, denoted $\mathscr{R}$, is defined as $\mathscr{R} = \{Z \mid z(\tau_1) \in K \text{ for some } x_1 < x < x_2 \text{ and for some } \tau_1 < t_f \text{ and } z(t_f) \subset \Gamma_u.\}$

Definition 4.3.2. Let Z be a trajectory in $\mathscr{R}$. The Maslov Index of a trajectory Z on $W^u(z^*)$, denoted $M(Z)$, is the number of conjugate points along $z(t)$ for $t \in (-\infty, t_f]$, counting multiplicity.

Definition 4.3.3. Let Z be a trajectory in $\mathscr{R}$. The sub-river, denoted $\tilde{\mathscr{R}}$, is defined as $\tilde{\mathscr{R}} = \{Z \in \mathscr{R} | M(Z) = 0\}$.

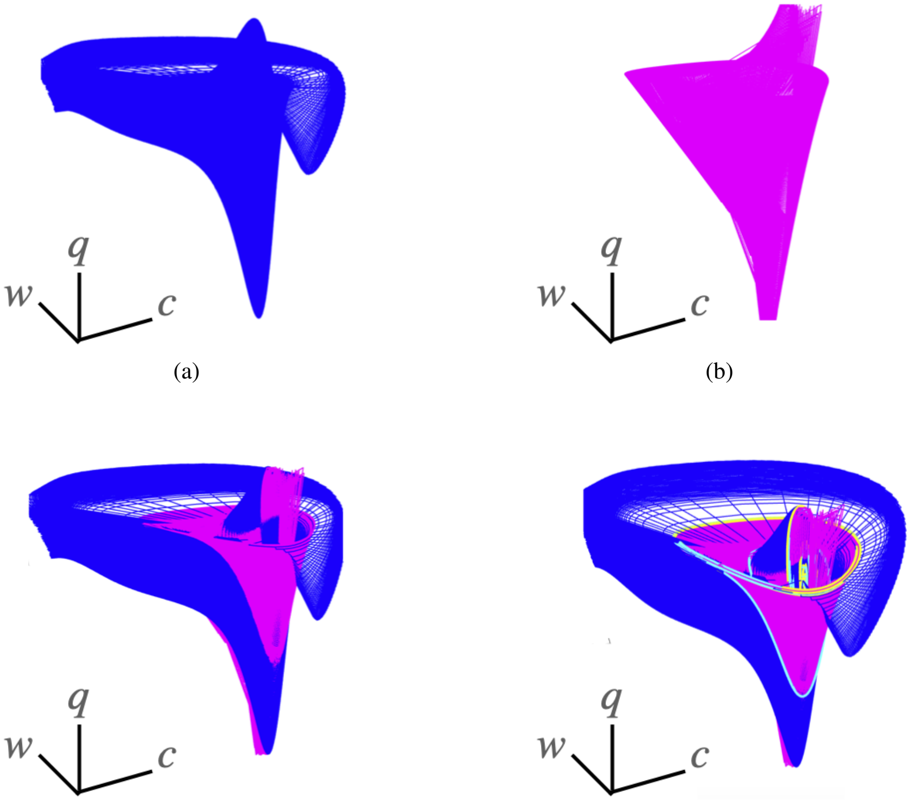

(a) (b)

(c) (d)

Figure 4.8: The invariant manifolds in (c, w, q) space. (a) $W^u(z^*)$. (b) $W^s(\Gamma_u)$. (c) $W^u(z^*)$ (blue) and $W^s(\Gamma_u)$ (magenta) overlaid together. (d) $W^u(z^*)$ (blue) and $W^s(\Gamma_u)$ (magenta) and their transverse intersections. The transverse intersections correspond to the heteroclinic orbits (yellow, cyan).

We note that $\tilde{\mathscr{R}} \subset \mathscr{R}$.

The angles of K that correspond to the River are depicted in Figure 4.10(b) and the angles of K that correspond to the subriver are shown in Figure 4.10(c). The River $\mathscr{R}$ of (4.19) is depicted in two dimensions in Figure 4.9 and in three dimensions in Figure 4.12(b), specifically in (c, w, q) space.

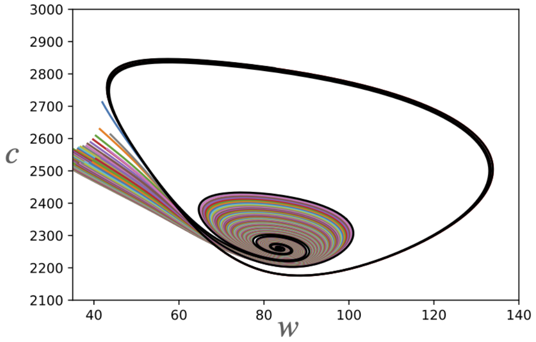

Figure 4.9: The River trajectories (colored curves) integrated until they are past Γ_u. The heteroclinic orbits $\mathscr{H}_1$ and $\mathscr{H}_2$ (both in black) form the banks of the River.

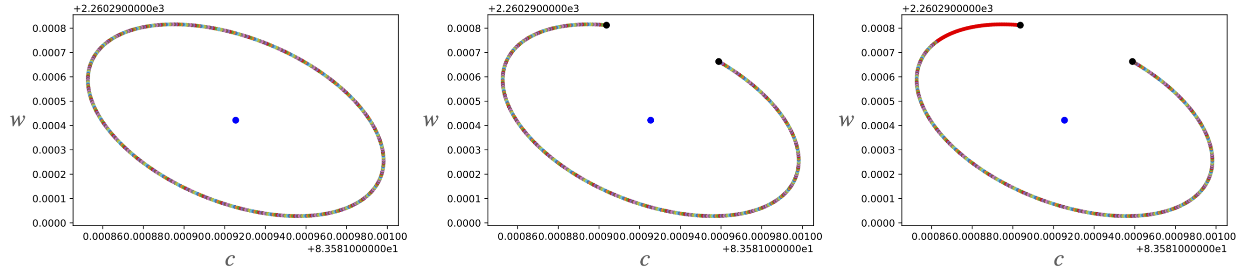

(a)

(b)

(c)

Figure 4.10: The stable fixed point z^* is denoted by the blue circle. The black circles represent the angles x_1 and x_2 associated with the heteroclinic orbits $\mathscr{H}_1$ and $\mathscr{H}_2$. (a) The collection of ψ values that form the set K. This circle lies in $W^u_{loc}(z^*)$ and integrated forward in time to find $W^u(z^*)$. (b) The arc of set K associated with the angles that will form the river trajectories when integrated forward in time. (c) The arc of set K associated with the angles that will form the river trajectories overlaid with the angles that will form the subriver (red).

Now, from Definitions 4.3.2 and 4.3.3, it is only necessary to find the number of conjugate points on a River trajectory to determine whether or not it is a trajectory in the subriver. A conjugate point occurs along a trajectory in $W^u(z^*)$ when the tangent space to the invariant manifold at a point on that trajectory has a degenerate projection onto (c, w) space. These points can be found by tracking the tangent space to $W^u(z^*)$ along trajectories in $W^u(z^*)$. There are coordinates on the space of planes that allow the tracking of this tangent space to $W^u(z^*)$ along a trajectory. The approach is to form the Plücker coordinates of the two-dimensional subspace in $\mathbb{R}^4$, as Plücker coordinates are a way to assign six homogeneous coordinates to planes in $\mathbb{R}^4$. The space of planes in $\mathbb{R}^4$ can be embedded into P^5.

A conjugate point can be conveniently described in Plücker coordinates. Using Lemma 4.3 from Fleurantin et al.[20], the time $t = \tau$ is a conjugate point for a trajectory $z(t) = (c(t), w(t), p(t), q(t))$ in $W^u(z^*)$ if $\rho_{12}(\tau) = 0$ for the Plücker coordinates of the tangent space of $W^u(z^*)$.

If Π is a two-dimensional subspace of $\mathbb{R}^4$, using coordinates (y_1, y_2, y_3, y_4), then the coordinates of Π are given by

$$dy_{i_1} \wedge dy_{i_2} \tag{4.29}$$

for all choices of (i_1, i_2)[25]. Let Π be a plane spanned by v_3 and v_4 from (4.24) with

$$v_3 = \begin{pmatrix} v_{31} \\ v_{32} \\ v_{33} \\ v_{34} \end{pmatrix} \text{ and } v_4 = \begin{pmatrix} v_{41} \\ v_{42} \\ v_{43} \\ v_{44} \end{pmatrix}. \tag{4.30}$$

Use (4.29), to set

$$\rho_{ij} = \begin{vmatrix} v_{3i} & v_{3j} \\ v_{4i} & v_{4j} \end{vmatrix} = dx_i \wedge dx_j(v_3, v_4), \quad 1 \le i, j \le 4, \quad i \neq j. \tag{4.31}$$

It follows the Plücker coordinates for this particular problem are given by

$$\begin{aligned} \rho_{12} &= dc \wedge dw, \\ \rho_{13} &= dc \wedge dp, \\ \rho_{14} &= dc \wedge dq, \\ \rho_{23} &= dw \wedge dp, \\ \rho_{24} &= dw \wedge dq, \\ \rho_{34} &= dp \wedge dq. \end{aligned} \tag{4.32}$$

How the Plücker coordinates of a plane vary can be captured by an ordinary differential equation governing the variation in time of the plane's Plücker coordinates. This is calculated using the properties of differential forms of the linearized system (4.19), which can be written as

$$\dot{U} = AU, \tag{4.33}$$

since it is Hamiltonian, and where $U = (dc, dw, dp, dq)$. Therefore, we only need to solve

$$\frac{d\hat{U}}{dt} = B(x(t), y(t), p(t), q(t))\hat{U}, \tag{4.34}$$

where $\hat{U} = (\rho_{12}, \rho_{13}, \rho_{14}, \rho_{23}, \rho_{24}, \rho_{34})$ and

$$B(c,w,p,q) = \begin{pmatrix} F_c + G_w & 0 & 1 & -1 & 0 & 0 \\ -pF_{cw} - qG_{cw} & 0 & -G_c & F_w & 0 & 0 \\ -pF_{ww} - qG_{ww} & -F_w & F_c - G_w & 0 & F_w & 1 \\ pF_{cc} + qG_{cc} & G_c & 0 & -F_c + G_w & -G_c & -1 \\ pF_{wc} + qG_{wc} & 0 & G_c & -F_w & 0 & 0 \\ 0 & pF_{cw} + qG_{cw} & -pF_{cc} - qG_{cc} & pF_{ww} + qG_{ww} & -pF_{cw} - qG_{cw} & -F_c - G_w \end{pmatrix}. \tag{4.35}$$

The trajectories in $W^u(z^*)$ are parameterized by angles x that determine a point on K. The algorithm for finding conjugate points along a trajectory that passes through K is as follows.

1. Take a trajectory of $W^u(z^*)$, $z(t)$, initialized from K. From this trajectory, the locations (c,w,p,q) as well as the time of each location are known.
2. Form Plücker coordinates of the unstable subspace of system (4.19) at z^* and initialize system (4.34) with these coordinates at the first time and point location of $z(t)$.
3. Integrate system (4.34) forward in time, by one time step. The ending location becomes the next initial condition. Repeat this process until reaching the final time of $z(t)$. Keep track of ρ_{12}.
4. Find the values of t where $\rho_{12} = 0$.

For every trajectory in $\mathscr{R}$, the conjugate points are tracked. Using Theorem 5.2 in Fleurantin et al.[20], the trajectories in $\tilde{\mathscr{R}}$ are minimizers of the Freidlin-Wentzell functional given their respective boundary value. While the trajectories in $\tilde{\mathscr{R}}$ are minimizers of the Freidlin-Wentzell functional, it is only expected that these trajectories are local minimizers. In fact, there will be infinitely many trajectories in $W^u(z^*)$ that cross Γ_u at a fixed boundary point that will consist of minimizers. The argument is that the trajectories in $\tilde{\mathscr{R}}$ play a fundamental role for the noisy realizations that escape for small but not vanishing noise strengths.

Figure 4.11 illustrates the tracking of conjugate points for the heteroclinic orbits $\mathscr{H}_1$ and $\mathscr{H}_2$ that were computed in Section 4.3.4. The heteroclinic orbits are shown in the left column and their associated plot in the right column, indicating if and where a conjugate point is detected, corresponding to where $\rho_{12} = 0$. These computations show that one heteroclinic orbit has Maslov Index: 0 (Figure 4.11(b)) and the other has Maslov Index: 2 (Figure 4.11(d)). The zero-conjugate point heteroclinic orbit is denoted by $\mathscr{H}_1$ and the two-conjugate point heteroclinic orbit is denoted by $\mathscr{H}_2$.

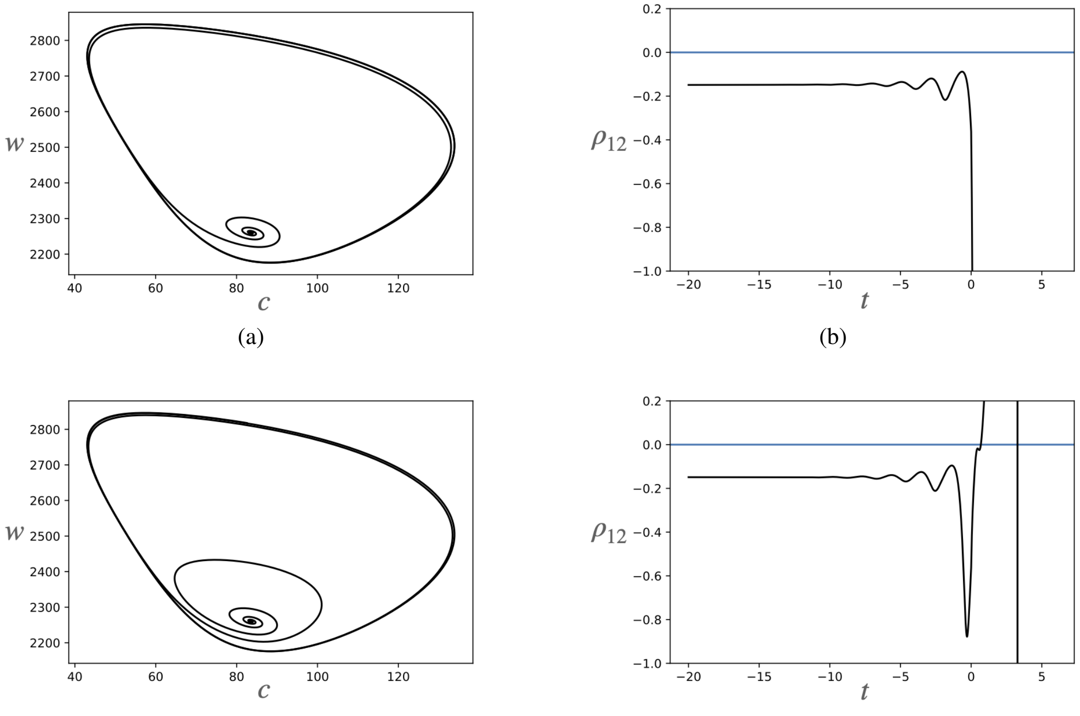

(a)

(b)

(c)

(d)

Figure 4.11: (a) The heteroclinic orbit $\mathscr{H}_1$ of system (4.19). (b) A plot tracking the component ρ_{12} for $\mathscr{H}_1$ and showing there are no conjugate points on the time interval specified as the curve never crosses 0. (c) The heteroclinic orbit $\mathscr{H}_2$ of system (4.19). (d) A plot tracking the component ρ_{12} for $\mathscr{H}_2$ and showing there are two conjugate points on the time interval specified as the curve crosses 0 twice.

4.3.6 Monte Carlo Simulations and Escaping Paths

The analysis carried out so far was aimed at finding a most probable path of escape for noisy trajectories through a periodic orbit that forms the boundary of the basin of attraction of the attracting fixed point. The work has been predicated on the notion that for small, but non-vanishing small noise, noisy trajectories that escape will not exhibit cycling behavior. Rather, they find an escape region at a specific part of the periodic orbit. Moreover, they will choose to leave the basin of attraction without overly cycling.

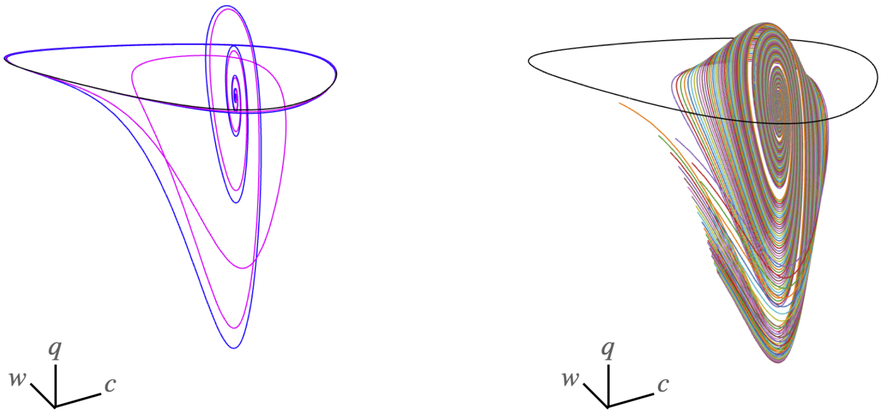

(a) (b)

Figure 4.12: (a) The heteroclinics $\mathscr{H}_1$ (blue) and $\mathscr{H}_2$ (magenta) in three-dimensional space. (b) Trajectories in the River $\mathscr{R}$ reaching Γ_u (black) in (c,w,q) space.

We show that this escape region exists by carrying out Monte Carlo simulations on the oceanic carbon cycle model with additive noise. In the computations, the noise strength is set at $\sigma_1 = \sigma_2 = 5$. It may be argued that this is not all that small, however, it was derived by pushing the noise to the smallest level for which convergence could be obtained for the exit distributions within reasonable computing time. Studying (4.36) with $\sigma_1 = \sigma_2 = 5$ on the time interval $[0,15]$, initialized at z^* with a step size of $dt = .005$, has the percentage of samples that escape at approximately 4%.

System (4.14) is numerically simulated using the Euler-Maruyama method to create a discretized Markov process[24] over the time interval $[0,15]$. The time interval is partitioned into sub-intervals of width $\Delta t = .005$, and the solution is initialized at $c = c^*$ and $w = w^*$. To create the discretized Markov process, the system is recursively defined as

$$\begin{aligned} c_{n+1} &= (f(c_n)[\mu(1-bs(c_n,c_p)-\theta\bar{s}(c_n,c_x)-\nu)+w_n-w_0])\Delta t+\sigma\Delta W_{1n}, \\ w_{n+1} &= (\mu[1-bs(c_n,c_p)+\theta\bar{s}(c_n,c_x)+\nu]-w_n+w_0)\Delta t+\sigma\Delta W_{2n}. \end{aligned} \tag{4.36}$$

Recall a standard Weiner process, W, satisfies the property that Brownian increments are independent and normally distributed with mean zero and variance Δt. It follows that $\Delta W_i = W_{i\,n} - W_{i\,n-1}$, $i = 1,2$, can be numerically simulated using $\sqrt{\Delta t}\cdot N(0,1)$, as shown in Claim 3.2.1.

The goal is to find the realizations that have transitioned from z^* to somewhere outside the unstable periodic orbit, and capture where on Γ_u they have exited. Let τ_i denote the first time a path, X_i, crosses Γ_u. Escape events are defined to be the paths X_i that have $\tau_i \leq 15$. Let the point of X_i at τ_i be given by

(c_i, w_i). Refer to Figure 4.13 for an example of realizations that have and have not escaped on the finite time interval, as well as the escape location. Assume for M realizations there are K escape events. We construct the distributions for the c and w locations for the K escape events. To verify these distributions of the escape location have converged, the convergence process from Section 3.2 is used for both c and w escape locations.

This process results in converged distributions for exit location in both c and w along Γ_u for this noise regime: starting with two sets of $N = 50000$ realizations and doubling until there are two sets of $N = 1600000$. In this case, $Err_c = 0.095 < 0.1$ and $Err_w = 0.098 < 0.1$. In total, there are 3200000 simulations in which 65008 realizations escape.

Collecting the points (c_i, w_i) from the paths that escaped, we see they fall on a specific part of Γ_u. In Figure 4.14(a) see a jointplot of the exit locations respectively and notice that there is a distinct spot on Γ_u where trajectories mostly exit. Additionally, see the overlay of the subriver and just the mouth of the subriver with the jointplot in Figure 4.14(b) and Figure 4.14(c) respectively. The majority of the subriver exits at the densest spot of the exit points.

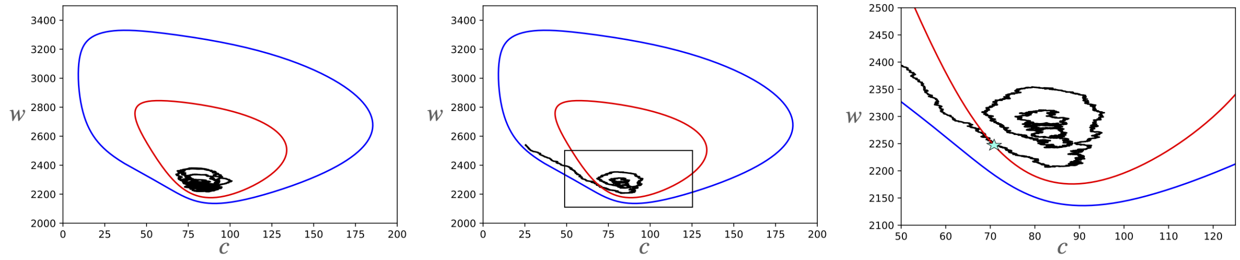

(a) (b) (c)

Figure 4.13: Two sample paths of (4.36) (black) initialized at z^* on the interval $[0, 15]$ with $dt = .005$ and $\sigma_1 = \sigma_2 = 5$, overlaid with the stable (blue) and unstable (red) periodic orbits. (a) The sample path does not escape. (b) The sample path escapes the unstable periodic orbit, Γ_u. (c) A zoomed-in version of the rectangular box in (b), where the cyan star denotes the path's exit location, (c_i, w_i).

In conclusion, a dynamical system approach was used for computing the most probable path where the boundary of the basin of attraction is a periodic orbit. Notice that besides the noisy realizations, these calculations do not depend on the noise strength. While vanishingly small noise predicts cycling, Freidlin-Wentzell theory can be used to show how cycling is actually resisted when noise strengths are larger. Of interest are the points on Γ_u where the River trajectories cross as they escape, in which a subset of these trajectories, the subriver, lined up almost exactly with the Monte Carlo simulations.

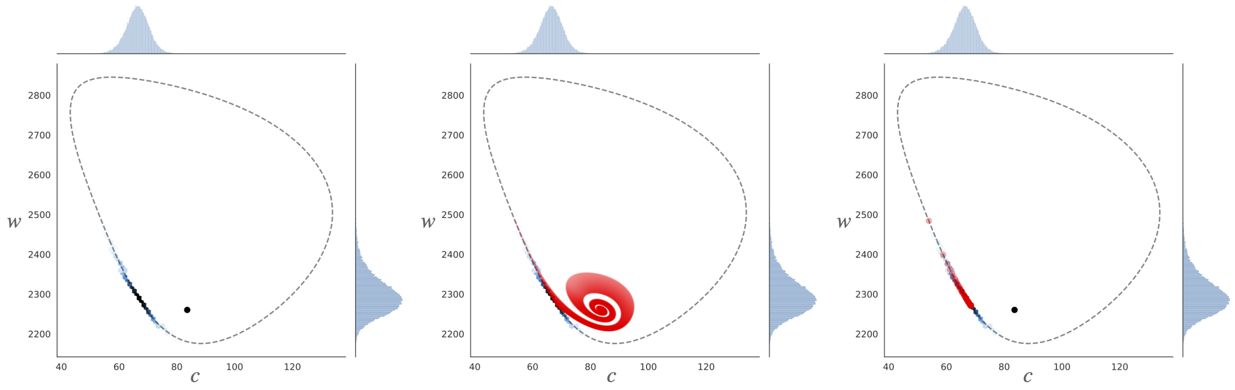

(a)

(b)

(c)

Figure 4.14: Jointplots and kernel density estimates of the tipped realizations of (4.36). Parameters are set at $\sigma_1 = \sigma_2 = 5$. The stable fixed point z^* is denoted by the black circle and the unstable periodic orbit Γ_u is denoted by the gray dashed curve. (a) Jointplot of points (c_i, w_i) from 21801 realizations that escaped through Γ_u. We can see a clear region of exit points. (b) Jointplot of points (c_i, w_i) from 65008 realizations that escaped through Γ_u overlaid with trajectories of the subriver (red). (c) Jointplot of points (c_i, w_i) from 65008 realizations that escaped through Γ_u overlaid with where subriver exits Γ_u (red points).

4.4 Discussion

4.4.1 Considering the Onsager-Machlup Functional for the Stochastic System

To understand why the noisy trajectories escape via a specific area when crossing Γ_u, we need to calculate the energy required by a path to escape to higher order. This involves the Onsager-Machlup functional[13] which becomes relevant when the noise is not vanishingly small. The Onsager-Machlup functional is considered as a perturbation of the Freidlin-Wentzell functional.

The Onsager-Machlup functional for a path $(c(t), w(t))$ on an interval $[t_0, t_f]$ is given by

$$I[c,w] = \int_{t_0}^{t_f} \left(\frac{(\dot{c_1} - f)^2}{\sigma_1^2} + \frac{(\dot{c_2} - g)^2}{\sigma_1^2} + \sigma_1 (\nabla \cdot V(c,w)) \right) dt, \tag{4.37}$$

where V is the vector field given by (4.3). To find the global minimizer of the system, we have to calculate this Onsager-Machlup term for each of our trajectories within the subriver. Essentially, this process provides a selection mechanism to pick out a specific most probable escape path out of our subriver trajectories.

Once we have the selected path, it needs to be verified with Monte Carlo simulations. A kernel density estimation will be used to determine how noisy trajectories exit Γ_u. The trajectories will be reparameterized to begin a certain radius away from z^*. This circle is chosen large enough so that realizations are on their way to tip, and not just bouncing around z^*. While this is an arbitrary choice of a parameterization, it shows the time evolution of the distribution of noisy trajectories. We believe, based on the work of Fleurantin et al.[20], the chosen trajectory from the Onsager-Machlup functional will match the distribution of noisy trajectories all along the path, where this trajectory is acting as a guide for the realizations exiting Γ_u.

4.4.2 Allowing Both Noise and Rate-Induced Tipping

As seen in this chapter, we have studied rate-induced tipping and noise-induced tipping individually within the oceanic carbon cycle model. In the next chapter, these two tipping mechanisms are combined by allowing white noise on both state variables, while also having the CO_2 injection rate be a time-dependent parameter. Realistically, it makes sense to still allow noise to act on the system and interact with the time-dependent CO_2 injection rate.

CHAPTER 5

A Canonical Problem for Rate and Noise-Induced Tipping

This chapter focuses on when there is a parameter shift (R-tipping) and the addition of random fluctuations (N-tipping). The aim is to assess the extent that rate and noise-induced tipping work together to facilitate tipping in cases where neither readily tip on their own.

We consider a canonical one-dimensional system with a ramp parameter and impose additive noise on its dynamics. The addition of noise to the system causes the system to tip for all r values less than the critical rate needed for rate-induced tipping, and does so with significantly increased probability over the noise or ramp acting alone. The most probable path to tip for all r values corresponds to the global minimizer of the Freidlin-Wentzell rate functional, which itself is a heteroclinic orbit. While we show these results in context of a canonical problem, the phenomenon found is suggestive for tipping between stable base states and threshold boundaries.

We compactify the system and derive the Euler-Lagrange equations associated with the Freidlin-Wentzell action functional[23]. Using a dynamical systems framework, including tracking invariant manifolds, using the Wazewski principle, and applying shooting methods, we prove there is always an intersection of the unstable manifold of the base state and stable manifold of the threshold state. Through numerical simulations it is shown that this intersection is unique.

There are three candidates for the path to tip between the two saddles of interest. However, this chapter exposes that the most probable path is unambiguous. The action values indicate that the heteroclinic connection through the found intersection point is the global minimizer of the Freidlin-Wentzell functional, and Monte-Carlo simulations, at appropriate noise levels, converge to this heteroclinic connection as well.

As nonzero rates are considered within the ramp parameter, the ramp is a nontrivial component of the system. Consequently, this means that the additive noise should be of small levels, away from the limit, as otherwise the noise effects would come after the ramp finishes, and our focus is on the interplay of these phenomena. A drawback of the Freidlin-Wentzell theory is that it necessitates vanishingly small noise[23]. In focusing on a small but not vanishingly small noise regime, the transient behavior of the underlying deterministic system will play an important role. The Freidlin-Wentzell theory will still hold in regard to the dynamical structure for small noise strengths, namely the heteroclinic connection will be the most probable path, but more discussion is needed when considering the expected time to tip. The extension from vanishingly small to small noise levels is relevant for several applications of interest, especially in environmental, social, or biological contexts, as detailed in the motivation for this work in Chapter 1.2.

The addition of noise, regardless of size, will always result in tipping of the system in infinite time. If we consider a finite time horizon, the addition of noise will cause the system to tip with a certain probability. The probability of tipping is dependent on both the noise strength and the speed of the ramp parameter, r, where the time horizon is chosen long enough to ensure the ramp function completes its transition. The size of small noise will change depending on the value of r being considered. The noise strengths are chosen so that the probability of tipping is less than 21%.

This analysis builds off the work of Ashwin et al.[5] and Ritchie and Sieber[36]. Ashwin et al.[5] introduced and studied the prototype model for rate-induced tipping:

$$\dot{x} = (x+\lambda)^2 - 1, \tag{5.1}$$

with a monotonically increasing time-dependent parameter,

$$\lambda(t) = \frac{\lambda_{max}}{2}\left(1+\tanh\left(\frac{\lambda_{max} r t}{2}\right)\right), \quad r > 0. \tag{5.2}$$

Using a compactification[44] as described in Chapter 4.2, they augment the system to an autonomous two-dimensional system containing equilibria and compact invariant sets, and in turn, the rate-induced tipping problem turns into a heteroclinic connection problem between two saddle equilibria. Perryman[35] finds the critical rate needed for tipping within the system is $r_c = 4/3$. Ritchie and Sieber[36] then considered this canonical problem with additive noise, and found that an interplay between the noise and ramp parameter results in tipping of the system before the critical rate, r_c, is reached. However, they only consider r values close to the critical rate. Ritchie and Sieber[36] find solutions of the variational problem determining the most likely tipping path using numerical continuation techniques. The majority of their work focuses on the most likely tipping time in the plane of two parameters: distance from tipping threshold and noise intensity.

5.1 Deterministic Dynamics

Consider

$$\dot{x} = (x+y)^2 - 1, \tag{5.3}$$

where $\dot{} = \frac{d}{dt}$, and a monotonically increasing time-dependent parameter, as proposed by Ashwin et al.[5],

$$y(t) = \frac{3}{2}\left(1 + \tanh\left(\frac{3rt}{2}\right)\right), \quad r > 0. \tag{5.4}$$

Reformulating the nonautonomous system in (5.3) into the compactified system using the ramp function in (5.4) as the coordinate transformation maps the real line onto the finite $y-$interval $(0,3)$. The y-interval is closed by including $y = 0,3$ which come from the limits of (5.4) at $\pm\infty$. This leads to the autonomous compactified two-dimensional system

$$\begin{aligned} \dot{x} &= (x+y)^2 - 1, \\ \dot{y} &= ry(3-y). \end{aligned} \tag{5.5}$$

The system given in (5.5) has four fixed points, though the focus is on the saddle equilibria $(-1,0)$ and $(-2,3)$. At a critical r, denoted r_c, there is a heteroclinic connection between the two saddle points. Perryman[35] found that $r_c = 4/3$ and the connecting orbit is the line given by $x = -\frac{y}{3} - 1$. For $0 < r < r_c$, the system end-point tracks the saddle equilibrium initialized at $(-1,0)$ to $(-4,3)$, and when $r > r_c$, the system tips to infinity. Figure 5.1 shows trajectories for different values of r for the system given in (5.5), demonstrating solution behaviors when initializing at the saddle $(-1,0)$.

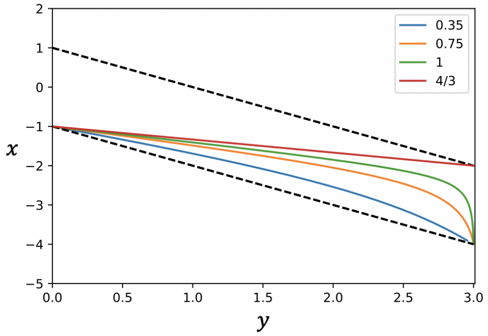

Figure 5.1: Solutions of the compactified system given by (5.5). The blacked dash curves track the fixed points $x = 1 - y$ and $x = -1 - y$ in the frozen system over time. The colored trajectories are solution curves initialized at $x = -1, y = 2.80729 \times 10^{-13}$ for different values of r. Solution curves with $0 < r < 4/3$ do not tip, whereas the solution curves with $r \geq 4/3$ tip. There is a heteroclinic connection between the two saddle equilibria at $r = 4/3$.

5.2 Building the Stochastic Framework

For the remainder of this work, we want to consider the effects of additive noise on the dynamics of x in (5.5). However, to use Freidlin-Wentzell theory, noise has to be considered on both the dynamics of x and y, but then we can take the limit as noise goes to zero in the y component. The stochastic version of the canonical problem is of the form

$$\begin{aligned} dx &= f(x,y)dt + \sigma_1 dW_1 = ((x+y)^2 - 1)dt + \sigma_1 dW_1, \\ dy &= g(x,y)dt + \sigma_2 dW_1 = (ry(3-y))dt + \sigma_2 dW_2. \end{aligned} \tag{5.6}$$

Speaking generally of this form, x, y are the stochastic processes parameterized by time, f, g are the deterministic pieces of the system, W_1, W_2 are standard Wiener processes, and σ_1, σ_2 denote the respective noise strengths.

With the addition of noise to the system, with probability equal to one, there is tipping in the system between the two saddle equilibria. We want to find the most probable path to tip between these two points. The tool used to study these transitions is the Freidlin-Wentzell theory of large deviations, where the action functional and derivation of the Euler-Lagrange equations were introduced in Section 3.1.

5.3 A Dynamical Systems Perspective on the Canonical Problem

The general Euler-Lagrange equations from (3.11) for the stochastic version of the canonical problem (5.6) become

$$\begin{aligned} \ddot{x} &= f_y \dot{y} + f f_x, \\ \ddot{y} &= g g_y + \frac{\sigma_2^2}{\sigma_1^2}(f f_y - \dot{x} f_y), \end{aligned} \tag{5.7}$$

as $g(x,y) = g(y)$, implying $g_x = 0$. Using the Euler-Lagrange equations given by (5.7), we make a Legendre transform[4] to create a degree four Hamiltonian system. Let

$$\begin{aligned} p &= \frac{\dot{x} - f}{\sigma_1^2}, \\ q &= \frac{\dot{y} - g}{\sigma_2^2}. \end{aligned} \tag{5.8}$$

Differentiating p and q with respect to t implies

$$\begin{aligned} \dot{p} &= \frac{\ddot{x} - f_x\dot{x} - f_y\dot{y}}{\sigma_1^2}, \\ \dot{q} &= \frac{\ddot{y} - g_y\dot{y}}{\sigma_2^2}. \end{aligned} \tag{5.9}$$

Then $\ddot{x}$ is substituted into $\dot{p}$ and $\ddot{y}$ is substituted into $\dot{q}$ from (5.7), resulting in

$$\begin{aligned} \dot{p} &= \frac{(f_y\dot{y} + ff_x) - f_x\dot{x} - f_y\dot{y}}{\sigma_1^2} \\ &= \frac{ff_x - f_x\dot{x}}{\sigma_1^2} \\ &= \frac{ff_x - f_x(f + \sigma_1^2 p)}{\sigma_1^2} \\ &= -f_x p, \\ \dot{q} &= \frac{\frac{\sigma_2^2}{\sigma_1^2}(-\dot{x}f_y + ff_y) + gg_y - g_y\dot{y}}{\sigma_2^2} \\ &= \frac{\frac{\sigma_2^2}{\sigma_1^2}(-(f + \sigma_1^2 p)f_y + ff_y) + gg_y - g_y(g + \sigma_2^2 q)}{\sigma_2^2} \\ &= \frac{-\sigma_2^2 pf_y - \sigma_2^2 qg_y}{\sigma_2^2} \\ &= -f_y p - g_y q. \end{aligned} \tag{5.10}$$

Using the expressions for $\dot{p}$ and $\dot{q}$ from (5.10) and rearranging the expressions in (5.8) for $\dot{x}$ and $\dot{y}$, the degree four Hamiltonian system is of the form

$$\begin{aligned} \dot{x} &= f + \sigma_1^2 p, \\ \dot{p} &= -f_x p, \\ \dot{y} &= g + \sigma_2^2 q, \\ \dot{q} &= -g_y q, \end{aligned} \tag{5.11}$$

and the associated Hamiltonian function is

$$H(x,p,y,q) = fp + gq + \frac{\sigma_1^2}{2}p^2 + \frac{\sigma_2^2}{2}q^2. \tag{5.12}$$

As mentioned earlier, we want to only consider noise on the dynamics of x, as y is a time parameterization, and thus σ_2 is sent to zero. It follows that $\dot{x}, \dot{p}, \dot{y}$ are all independent of q, and so it is possible to project the equations into x, p, y space. Using this independence of q and substituting f and g as they are defined in (5.6) results in (5.11) becoming

$$\begin{aligned} \dot{x} &= (x+y)^2 - 1 + \sigma_1^2 p, \\ \dot{p} &= -2(x+y)p, \\ \dot{y} &= ry(3-y). \end{aligned} \tag{5.13}$$

In addition, notice that $p=0$ is invariant and carries the deterministic flow given by (5.5). These equations in (5.13) are the most probable path equations. Throughout this work, remember that x is the original state variable, y is a time reparameterization, and p is the extra variable representing the work a trajectory has to do against the vector field.

Notice that alternatively we could have derived the Euler-Lagrange equations using the Freidlin-Wentzell functional on the nonautonomous system (5.3), then use a Legendre transform to create a degree two Hamiltonian system, and finish by compactifying the system. The compactification process and the Euler-Lagrange and Legendre transform procedures commute, as proven below in Claim 5.3.1, and results in the same equations as shown in (5.13). This alternative method is useful when performing numerical experiments in Section 5.4.2.

Claim 5.3.1. *The compactification process and the Euler-Lagrange and Legendre transform procedures commute.*

Proof. Consider the one-dimensional system (5.3) with ramp function (5.4). The stochastic version of this system is of the form

$$dx = f(x,t)dt + \sigma_1 dW_1. \tag{5.14}$$

The most probable path, between two points is a curve $c_1(t)$ that minimizes the Freidlin-Wentzell functional

$$I[c_1] = \int_{t_0}^{t_f} \frac{(\dot{c_1} - f(x,t))^2}{\sigma_1^2} dt. \tag{5.15}$$

Minimizing this functional would be similar to that of the argument shown in Section 3.1. The resulting Euler-Lagrange equation for the system in (5.3) is

$$\ddot{x} = f f_x + f_t. \tag{5.16}$$

Making a Legendre transform with

$$p = \frac{\dot{x} - f}{\sigma_1^2}, \tag{5.17}$$

results in a two-dimensional Hamiltonian system. Differentiating p with respect to t and substituting $\ddot{x}$ from (5.16) implies

$$\begin{aligned} \dot{p} &= \frac{\ddot{x} - f_x\dot{x} - f_t}{\sigma_1^2} \\ &= \frac{ff_x + f_t - f_x\dot{x} - f_t}{\sigma_1^2} \\ &= \frac{ff_x - f_x(f + \sigma_1^2 p)}{\sigma_1^2} \\ &= -f_x p. \end{aligned} \tag{5.18}$$

Using the expressions for $\dot{p}$ from (5.18) and rearranging the expressions in (5.17) for $\dot{x}$, the degree two Hamiltonian system is of the form

$$\begin{aligned} \dot{x} &= f + \sigma_1^2 p, \\ \dot{p} &= -f_x p, \end{aligned} \tag{5.19}$$

and the associated Hamiltonian function is

$$H(x,p,y,q) = fp + \frac{\sigma_1^2}{2}p^2. \tag{5.20}$$

Now introducing the coordinate transform $y(t) = \frac{3}{2}\left(1 + \tanh\left(\frac{3rt}{2}\right)\right)$ and compactifying the system leads to the three-dimensional system

$$\begin{aligned} \dot{x} &= (x+y)^2 - 1 + \sigma_1^2 p, \\ \dot{p} &= -2(x+y)p, \\ \dot{y} &= ry(3-y), \end{aligned} \tag{5.21}$$

and finishes the proof that the two procedures commute.

□

Performing a phase portrait analysis on (5.13), there are six equilibria: three on $y = 0$ and three on $y = 3$. We are interested in the heteroclinic connection between the saddle points $(-1,0,0)$ and $(-2,0,3)$, as these correspond to the saddles $(-1,0)$ and $(-2,3)$ in our two-dimensional phase space. For notation purposes, refer to $(-1,0,0)$ as s_1 and $(-2,0,3)$ as s_2. A quick check of the eigenvalues of (5.13) linearized at s_1 show

s_1 has a one-dimensional stable manifold and a two-dimensional unstable manifold. Similar methods show s_2 has a one-dimensional unstable manifold and a two-dimensional stable manifold. We denote the unstable and stable manifolds of a point p by $W^u(p)$ and $W^s(p)$ respectively. Using this notation, the desired heteroclinic will lie on $W^u(s_1)$ and also on $W^s(s_2)$. See Figure 5.2 for what the phase space looks like on $y = 0$. Notice that asymptotically the phase space dynamics are identical on $y = 3$.

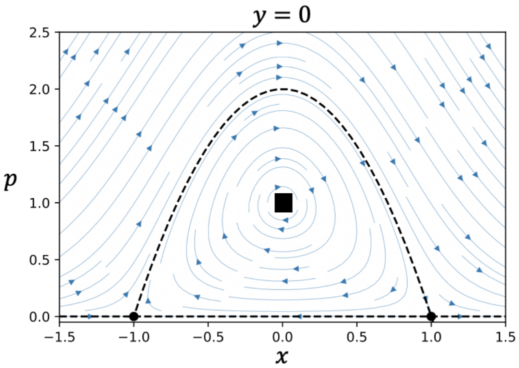

Figure 5.2: The phase space for (5.13) on the plane $y = 0$. There are two saddles (black circles) and one center (black square). The black dashed lines represent where $H = 0$. The blue arrows show the direction of the vector field. The phase space is asymptotically identical on the plane $y = 3$.

Using the Hamiltonian structure in the invariant planes $y = 0$ and $y = 3$ creates two possible tipping paths between the two saddles of interest. The first possible path is to tip from s_1 to $(1,0,0)$ in $y = 0$ and then end-point track from $(1,0,0)$ to s_2 in $p = 0$. The second possible path is to end-point track in $p = 0$ from s_1 to $(-4,0,3)$ and then tip to s_2 in $y = 3$. As seen in Section 5.4.3 and Section 5.4.4, these paths have essentially an infinite time until tipping occurs and have a high action value.

We claim there is always a third heteroclinic connection that is the most probable path and is the path of least action. To prove the existence of a heteroclinic orbit between the two saddles s_1 and s_2 for all $0 < r \leq r_c$, we first show $W^u(s_1)$ is continuous on the plane $y = -x$ for $y \leq \frac{3}{2}$ for $0 < r \leq r_c$, and then, that $W^u(s_1)$ and $W^s(s_2)$ are symmetric.

Proposition 5.3.2. *The primary intersection of $W^u(s_1)$ with the plane $y = -x$ is continuous on the plane $y = -x$ for $y < \frac{3}{2}$ and $r > 0$.*

Proof. The Wazewski Principle[40] states the following:

Let W^- be the immediate exit set of W and let W^0 be the eventual exit set of W. If W^- is closed relative to W^0, then W is a Wazewski set, and the map $K : W^0 \to W^-$ that takes each point to the first where it exits W, *is continuous.*

We define the primary intersection of $W^u(s_1)$ with the plane $y = -x$ to be the first crossing of this plane from trajectories initialized in the unstable subspace of s_1 coming from $-\infty$. For the system given in (5.13), the Wazewski set, W, is the space bounded by the following planes: $y = -1-x$, $y = -x$, $y = 0$, $y = 3/2$, and $p = 0$, and extends infinitely in the positive p direction. Based on flow of the vector field, the following are true about the boundaries of W: $y = -1-x$ is an entrance set, $y = 0$ and $p = 0$ are neither entrance nor exit sets as they are invariant planes, and $y = 3/2$ is an exit set. On $y = -x$, below the curve $p = \frac{1}{\sigma_1^2}(1-ry(3-y))$ is an entrance set, and above it, an exit set. Refer to Figure 5.3 for a visual of W.

Now it needs to be determined what happens on the curve $p = \frac{1}{\sigma_1^2}(1-ry(3-y))$ itself, which is the boundary between an entrance set and an immediate exit set. Consider x and p as functions of y. Looking at the first and second derivatives at the point $z = (-y, \frac{1}{\sigma_1^2}(1-ry(3-y)), y)$, representing any point on this curve, these derivatives simplify to

$$\begin{aligned}
\left.\frac{dx}{dy}\right|_z &= -1, \\
\left.\frac{d^2x}{dy^2}\right|_z &= \frac{3-2y}{y(3-y)} > 0 \text{ for } y < 3/2, \\
\left.\frac{dp}{dy}\right|_z &= 0, \\
\left.\frac{d^2p}{dy^2}\right|_z &= 0.
\end{aligned} \tag{5.22}$$

In (5.22), $\frac{dx}{dy} = -1$ and $\frac{d^2x}{dy^2} > 0$. By the second derivative test, a trajectory would be concave up at this point, forcing any points to leave and consequently not enter W. Therefore the boundary of the immediate exit set is contained in the immediate exit set, and the following can be said about the immediate exit set and eventual exit set of W:

$$W^- = \{(x,p,y) \mid y = 3/2, y = -x \text{ for } p \geq \frac{1}{\sigma_1^2}(1-ry(3-y))\},$$

$$W^0 = \{(x,p,y) \mid W \setminus \{y = 0, y = -1-x, p = 0, (-1,0,0), (0,1,0)\}\}.$$

The boundary of the immediate exit set is in the immediate exit set, and it easily follows that W^- is closed relative to W^0, implying W is a Wazewski set and the map $K: W^0 \to W^-$ is continuous for $y < \frac{3}{2}$. This further implies that $W^u(s_1)$ intersected with the plane $y = -x$ is continuous for $y < \frac{3}{2}$ and $r > 0$. $\square$

Proposition 5.3.3. *$W^u(s_1)$ intersected with W^- crosses the plane $y = \frac{3}{2}$ for $0 < r \leq r_c$.*

Proof. Notice $y = \frac{3}{2}$ separates W^- into two pieces. Take the quarter circle of radius ε around the fixed point s_1 intersected with $W^u(s_1)$ that lies in W, and call this curve C_W. Applying the map K to C_W results in a curve in $\mathbb{R}^3$, specifically a curve lying in W^- by the definition of Wazewski map K.

Since C_W is a closed curve, it is possible to track where the two endpoints of C_W map to under K. The first endpoint of C_W has $y = 0, p \neq 0$ and second endpoint of C_W has $p = 0, y \neq 0$. Take the endpoint of C_W that lies in $y = 0$. Since the $y = 0$ plane is invariant, when applying K, the trajectory must stay in this plane and eventually exit through $y = -x$ and above $p = \frac{1}{\sigma_1^2}(1 - ry(3-y))$. Take the endpoint of C_W that lies in $p = 0$. Since the $p = 0$ plane is invariant, applying K, the trajectory must stay in this plane. Since $\dot{y} > 0$, this trajectory will eventually exit through $y = \frac{3}{2}$, when $0 < r \leq r_c$.

$W^u(s_1)$ intersected with W^- actually intersects $y = \frac{3}{2}$ by the intermediate value theorem, as K is a continuous map, and one endpoint of C_W maps to the plane $y = -x$ in $y = 0$ while the other endpoint of C_W maps to the plane $y = 3/2$ in $p = 0$. Therefore the intersection of $W^u(s_1)$ and the plane $y = -x$ is continuous for $y \leq \frac{3}{2}$ for $0 < r \leq r_c$. See Figure 5.3 for an illustration of this shooting argument. $\square$

Proposition 5.3.4. *$W^u(s_1)$ and $W^s(s_2)$ are symmetric.*

Proof. Recall the system given in (5.13). Making the change of variables $\tau = -t$, the time reversed system is

$$\begin{aligned} x' &= -(x+y)^2 + 1 - \sigma_1^2 p, \\ p' &= 2(x+y)p, \\ y' &= ry(y-3). \end{aligned} \tag{5.23}$$

We transform the variables x, p, y by

$$\begin{aligned} \hat{x} &= -x - 3, \\ \hat{p} &= p, \\ \hat{y} &= 3 - y. \end{aligned} \tag{5.24}$$

and substitute them into the time-reversed system found in (5.23). The equations simplify to

$$\begin{aligned} \hat{x}' &= (\hat{x}+\hat{y})^2 - 1 + \sigma_1^2 \hat{p}, \\ \hat{p}' &= -2(\hat{x}+\hat{y})\hat{p}, \\ \hat{y}' &= r\hat{y}(3-\hat{y}). \end{aligned} \tag{5.25}$$

Observe that (5.25) is in the original form as given in (5.13), and it follows that $W^u(s_1)$ and $W^s(s_2)$ are symmetric.

□

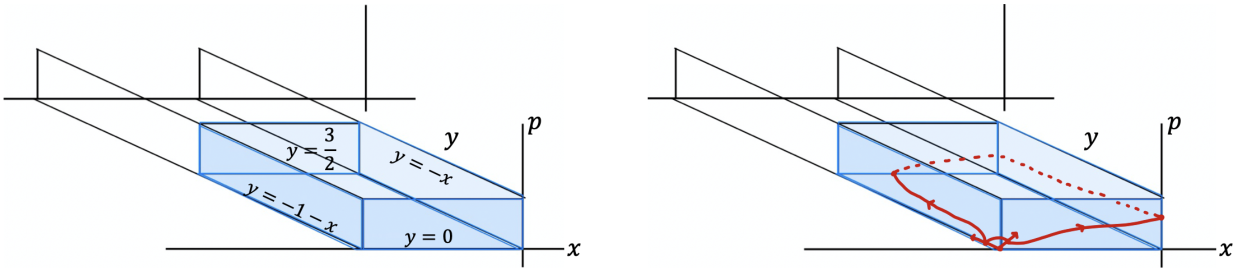

Figure 5.3: The boundary of the Wazewski set is in blue and extends infinitely in the positive p direction. It is the space bounded by $y = -1 - x, y = 0, y = -x, y = \frac{3}{2}$, and $p = 0$. Taking a quarter circle of radius ε about s_1 intersected with the piece of $W^u(s_1)$ lying in W, and applying map K, results in the dotted red curve.

Theorem 5.3.5. *There exists a heteroclinic connection between the saddle points s_1 and s_2 that goes through the plane $y = -x$ at $y = \frac{3}{2}$ for $0 < r \leq r_c$.*

Proof. Using Propositions 5.3.2 and 5.3.3, the intersection of $W^u(s_1)$ and the plane $y = -x$ is continuous for $y \leq \frac{3}{2}$ for $0 < r \leq r_c$. The symmetry of $W^u(s_1)$ and $W^s(s_2)$, proven in Proposition 5.3.4, implies the intersection of $W^s(s_2)$ intersected with the plane $y = -x$ is continuous for $y \geq \frac{3}{2}$ for $0 < r \leq r_c$. Therefore $W^u(s_1)$ and $W^s(s_2)$ will always intersect once in the plane $y = -x$ at $y = \frac{3}{2}$, implying a heteroclinic connection between s_1 and s_2 for $0 < r \leq r_c$, and concluding the proof of Theorem 5.3.5. □

There exists a heteroclinic connection between s_1 and s_2 for all $0 < r \leq r_c$, and this proof demonstrates how to find this heteroclinic using the intersection of the invariant manifolds. In the deterministic system, for $0 < r < r_c$, there would not be tipping or a heteroclinic connection between the saddles. The presence of noise, regardless of size, allows direct tipping between these saddles within the system.

5.4 Computational Methods and Numerical Results

5.4.1 Visualization of Invariant Manifolds and the Heteroclinic Connection

Section 5.3 proved the existence of the intersection of $W^u(s_1)$ and $W^s(s_2)$ at $y = 3/2$, giving rise to a heteroclinic connection between the two saddle points through that specific point. We numerically compute these manifolds, plot them in $y = -x$, and observe their intersection at $y = 3/2$. This enables the visualization of their intersection, as well as enables the computation of the trajectory through the intersection point. The trajectory is then projected into the xy plane to find the heteroclinic connection in the two-dimensional extended phase space.

The local unstable subspace of s_1 is spanned by the two vectors

$$\left(\frac{\sigma_1^2}{4}, 1, 0\right)^T \text{ and } \left(\frac{-2}{3r+2}, 0, 1\right)^T, \tag{5.26}$$

which span the plane

$$4(x+1) - (\sigma_1^2 + 4)p - \frac{12r}{3r+2}y = 0. \tag{5.27}$$

Intersecting this plane with the sphere

$$(x+1)^2 + p^2 + y^2 = (0.001)^2 \tag{5.28}$$

and taking points such that $y, p > 0$, results in a curve of points that lie in the unstable subspace, as seen in Figure 5.4. This curve is discretized and the tuples are used as a set of initial conditions.

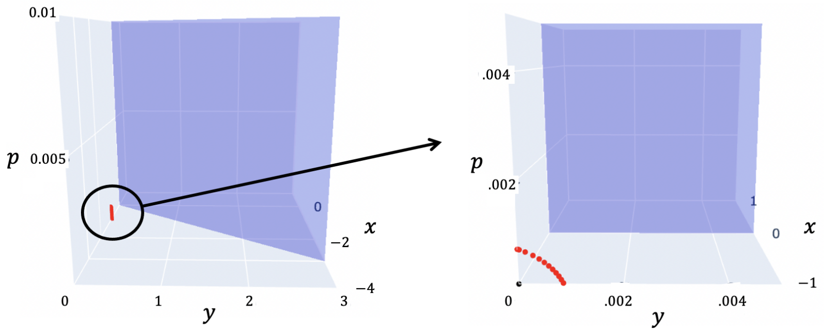

Figure 5.4: Parameters are set at $r = 1, \sigma_1 = 0.15$. The red curve is the intersection of the sphere (5.28) and the plane (5.27) spanned by (5.26).

We numerically run system (5.13) forward in time for each initial condition until the trajectory first hits the plane $y = -x$. Similarly, this process is performed when looking at the stable subspace of s_2 and running system (5.13) backwards in time. The intersection of these two curves is found in the plane $y = -x$, and through these simulations, observe that the intersection point of these two curves in $y = -x$ is unique. Running the system both forwards and backwards in time from the intersection point supplies the full heteroclinic trajectory. Refer to Figure 5.5 to see a visualization of $W^u(s_1)$ and $W^s(s_2)$ intersecting in the plane $y = -x$, as well as the trajectory through the intersection point for two different parameter pairs of r and σ_1, corresponding to the heteroclinic orbit between s_1 and s_2. Projecting this heteroclinic orbit into xy space is the connecting orbit between $(-1,0)$ and $(-2,3)$, and it is shown in the next section that this orbit is in fact the most probable path between these points.

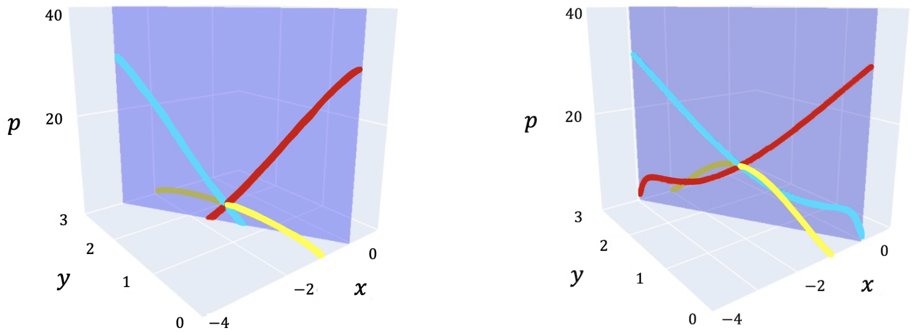

(a)

(b)

Figure 5.5: $W^u(s_1)$ (red) and $W^s(s_2)$ (cyan) in the plane $y = -x$ (purple) for $y \in (0,3)$. The trajectory through their intersection point is the heteroclinic orbit connecting s_1 and s_2 (yellow). (a) Parameters are set at $r = 1, \sigma_1 = 0.25$. (b) Parameters are set at $r = 0.5, \sigma_1 = 0.25$.

In the compactified system, the heteroclinic connections do not look identical when varying r. For fixed r and varying σ_1, the heteroclinic connections will look identical when projected into the xy plane as this variation of σ_1 only scales the p variable. Notice that in Figure 5.7(b), while the heteroclinic orbit connecting the two saddle equilibria looks linear, it is not a line. As r approaches the critical rate of the deterministic system, the heteroclinic orbit becomes deceptively linear.

Besides the existence of the heteroclinic connection between s_1 and s_2 proven in Section 5.3, this first set of numerical simulations now verifies the uniqueness of the heteroclinic connection between s_1 and s_2, though it has not yet been shown that the heteroclinic connection is the most probable path between these two points. These calculations are performed in the next section.

5.4.2 Monte Carlo Simulations and the Most Probable Path

The heteroclinic connection constructed in Section 5.3 is in fact the most probable path and corroborated using Monte Carlo simulations. Recall the original problem was a one-dimensional differential equation. Consider its stochastic version, given by

$$\begin{aligned} dx &= ((x+y)^2-1)dt+\sigma_1 dW, \\ y(t) &= \frac{3}{2}\left(1+\tanh\left(\frac{3rt}{2}\right)\right), r>0. \end{aligned} \tag{5.29}$$

As shown in Claim 5.3.1, the order of compactification process and the Euler-Lagrange and Legendre procedures commute, so (5.29) can be used for running simulations as it is computationally less expensive.

Realizations of (5.29) are numerically simulated using the Euler-Maruyama method, described in Section 3.2 over a time interval of length 30. To apply the Euler-Maruyama method, the time interval is partitioned into sub-intervals of width $\Delta t = 0.001$, and the solution is initialized at $x=-1$ and $y = 2.80729\times 10^{-13}$. This y initial condition is used to find the corresponding t_0 by solving the rescaled time $rt=-10$. This explains why the exact time intervals of length 30 vary for each case. Changing the initial y value, corresponding to changing the starting time, only shortens or extends the time for a realization to tip[36]. To create the discretized Markov process, x is recursively defined as

$$x_{n+1} = x_n + ((x_n+y(t_n))^2-1)\Delta t + \sigma_1 \Delta W_n. \tag{5.30}$$

Recall a standard Weiner process, W, satisfies the property that Brownian increments are independent and normally distributed with mean zero and variance Δt. It follows that $\Delta W = W_n - W_{n-1}$ can be numerically simulated using $\sqrt{\Delta t}\cdot N(0,1)$, as shown in Claim 3.2.1.

We simulate M realizations of (5.29) using the Euler-Maruyama method given in (5.30). These realizations are mapped to two dimensional phase space by plotting $(y(t),x)$. We define tipping to be when a realization of (5.29) crosses $W^s(-2,3)$, and $\lim_{t\to\infty} x(t) \neq -4$. $W^s(-2,3)$ can be see in Figure 5.6.

Of the M realizations, M_{tip} is defined as the number of realizations that tip on the finite time interval of choice. Thus $M-M_{tip}$ do not tip, an example of which is shown in Figure 5.7(a) for $r=1, \sigma_1 = 0.15$. There are M_{tip} points within the M_{tip} realizations that tipped for every discretized time. Python is used to get the kernel smoothing density estimation of the M_{tip} points at each time. This finds the ‘most probable point' at every time step, which is determined by the peak of the kernel density estimation (KDE). This peak corresponds to the mode of the M_{tip} points at that time. Plotting the mode at each time step provides an approximation for the most probable path. Overlaying the numerically-simulated most probable path, with what was found using the the projection of the trajectory through intersection of $W^u(s_1)$ and $W^s(s_2)$ in $y = -x$ in Section 5.4.1, observe that the approximation matches the actual path extremely well, an example of which is shown in Figure 5.7(b) for $r = 1, \sigma_1 = 0.15$. Therefore, the trajectories that tipped followed the heteroclinic connection, and the heteroclinic connection between the two saddles is the most probable path.

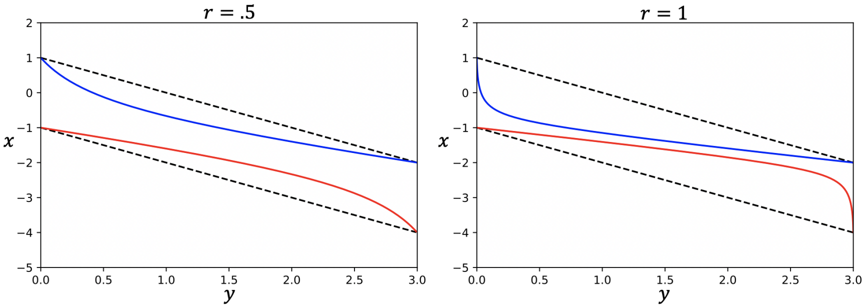

Figure 5.6: $W^u(-1,0)$ (red) and $W^s(-2,3)$ (blue) for $r = 0.5$ and $r = 1$. Tipping occurs when a realization of (5.30) crosses $W^s(-2,3)$ and $\lim_{t\to\infty} \neq -4$.

As mentioned above, the Monte Carlo simulations show that trajectories either tip to infinity or end-point track the stable path to $(-4,3)$ on the given finite time horizon. The trajectories that end-point track the stable path follow the pullback attractor^5 of $(-1,0)$. Performing another kernel smoothing density estimation on the realizations that did not tip, observe that these trajectories actually peak along this pullback attractor, an example of which is shown in Figure 5.7(c) for $r = 1, \sigma_1 = 0.15$.

The heteroclinic orbit and the pullback attractor are objects that can be used to separate trajectories of the system. These computations show that the addition of noise allows the system to tip when its deterministic equivalent would not tip, as the trajectory would be the pullback attractor. For the specific parameter regime $r = 1, \sigma_1 = 0.15$ as depicted above, even with r being $3/4$ of the critical rate, tipping occurs within the system.

5.4.3 Time to Tip

There is concern that the influence of noise on (5.3) is the sole reason the system exhibits tipping. However, it is verified in this section that the tipping occurs due to the interplay of both the ramp parameter and noise. The frequency of tipping largely increases with this addition of small noise strengths interacting with the ramp parameter.

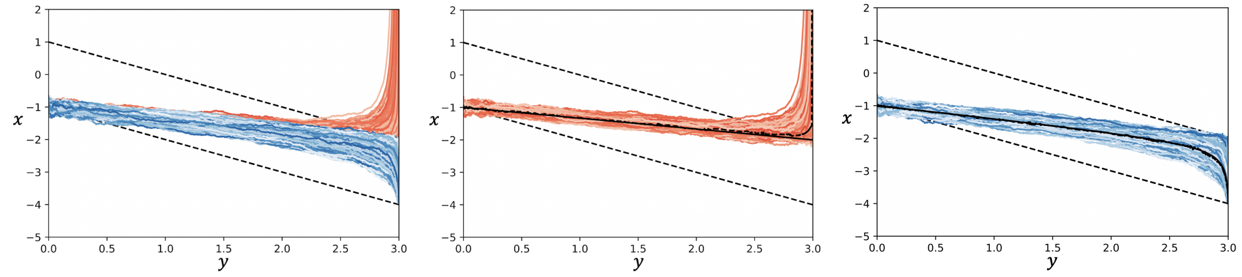

(a) (b) (c)

Figure 5.7: (a) 3000 Monte Carlo simulations of (5.29) with $r = 1$ and $\sigma_1 = 0.15$ on the interval $[0,30]$ with $dt = 0.001$. 2807 realizations do not tip (blue) and 193 tip (red). (b) The realizations that tipped, overlaid with the heteroclinic orbit found (solid black) and a kernel density estimate of the realizations that tipped (dashed black). (c) The realizations that did not tip, overlaid with the pullback attractor of $(-1,0)$ (solid black) and the kernel density estimate (dashed black).

Recall the original goal is to tip from $(-1,0)$ to $(-2,3)$, which correspond to s_1 and s_2 in the three-dimensional system in (5.13). Using (5.13), based on the stable and unstable directions of these saddles and the direction of the vector field, there were initially two possible ways to tip due to the Hamiltonian structure in the invariant planes $y = 0$ and $y = 3$. Section 5.3 proves that there is a third way of tipping via a heteroclinic orbit between the two saddles, which is now verified as the most probable path from the Monte Carlo simulations. Refer to Figure 5.8 for a visual of these possible tipping paths.

Notice that if tipping occurs in either $y = 0$ or $y = 3$, there is no interplay with the ramp parameter, as it would be before or after the ramping occurs. In the planes $y = 0, 3$, if there is no ramp parameter, then the system is a one-dimensional stochastic differential equation. Recall from Chapter 2 that there are asymptotic formulae to approximate the expected time to tip for gradient systems[9], given by

$$\mathbb{E}[\tau] \approx Ce^{\frac{2\Delta V}{\sigma_1^2}}, \tag{5.31}$$

where V is the associated potential function and ΔV gives the height of the potential barrier. The expected time to tip is calculated for each tipping path. In the numerical analysis, $0.08 \leq \sigma_1 \leq 0.3$ for all experiments, as a small noise regime is considered.

Case 1. Assume tipping from s_1 to $(1,0,0)$ occurs in $y = 0$ and then there is end-point tracking from $(1,0,0)$ to s_2 along $W^s(-2,3)$. We can find the expected time to tip between the fixed points in $y = 0$ as the system is a gradient system in this plane. The associated form of the gradient system and potential function, V, is

$$
\begin{aligned}
dx &= (x^2-1)dt + \sigma_1 dW \\
&= -\nabla V dt + \sigma_1 dW \\
&= -\nabla(x - \frac{1}{3}x^3)dt + \sigma_1 dW.
\end{aligned} \tag{5.32}
$$

The extrema of V correspond to the fixed points of the problem when $y = 0 : x = -1, 1$. Solving for the expected time to tip, without the ramp parameter,

$$
\mathbb{E}[\tau] \approx e^{\frac{8}{3\sigma_1^2}} > 10^{12}. \tag{5.33}
$$

The time to tip from s_1 to s_2 along this path will be some time greater than 10^{12}. There is a depiction of Case 1 in Figure 5.8(a).

Case 2. Similarly, assume there is an end-point tracking of the path from s_1 to $(-4,0,3)$ along $W^u(-1,0)$ and then tipping occurs from $(-4,0,3)$ to s_2 in $y = 3$. We find the expected time to tip in $y = 3$. Again, it is a gradient system and so the system is rewritten in terms of the potential function V,

$$
\begin{aligned}
dx &= ((x+3)^2-1)dt + \sigma_1 dW \\
&= -\nabla(-8x - 3x^2 - \frac{1}{3}x^3)dt + \sigma_1 dW.
\end{aligned} \tag{5.34}
$$

Solving for the expected time to tip, without the ramp parameter,

$$
\mathbb{E}[\tau] \approx e^{\frac{8}{3\sigma_1^2}} > 10^{12}. \tag{5.35}
$$

The time to tip from s_1 to s_2 along this path will also be some time greater than 10^{12}. There is a depiction of Case 2 in Figure 5.8(b).

Case 3. To determine the expected time to tip of the most probable path found in Section 5.3, a sufficient number of Monte-Carlo simulations are run so that the expected time to tip distribution converges. The Euler-Maruyama method is used to simulate M realizations of (5.29) on a time interval of length 30, initialized at $x = -1, y = 2.80729 \times 10^{-13}$, with a step size of $dt = 0.001$. Recall this initial condition for y is used to find the corresponding t_0 for each value of r. We want to find the realizations that have tipped to infinity, and capture when the mapped versions, $(y(t), x)$, have crossed $W^s(-2,3)$.

Let τ_i denote the first time a path, X_i of the form $(y(t), x)$, crosses $W^s(-2,3)$. Escape events are defined to be the paths X_i that have $\tau_i \leq 30$ and component $x \to \infty$. Assume that for M realizations there are K escape events. We construct the distribution for the K crossing times of $W^s(-2,3)$. To verify if the distribution of the time of escape events has converged, the process described in Section 3.2 is used.

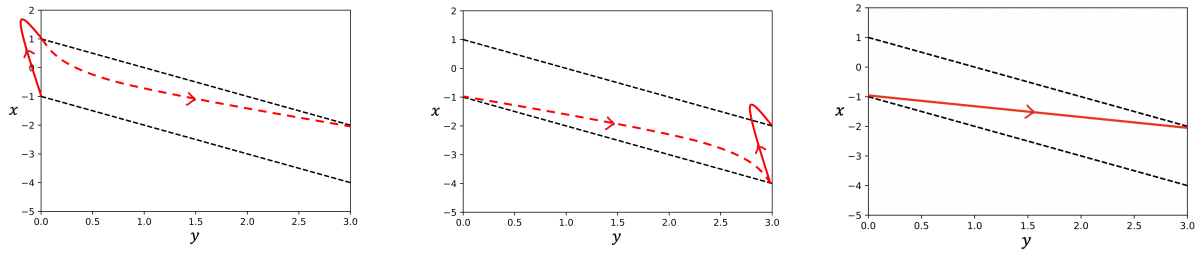

(a) (b) (c)

Figure 5.8: Schematic diagrams for the three possible ways to tip from saddle node $(-1,0)$ to saddle node $(-2,3)$. (a) Case 1. (b) Case 2. (c) Case 3. In Cases 1 and 2, the end-point tracking curves (dashed red) will be dependent on $W^u(-1,0)$ and $W^s(-2,3)$. Here they are sketched for $r = 0.5$. Additionally, in Cases 1 and 2, the solid red curves are to represent tipping via the heteroclinic orbit in $y = 0$ and $y = 3$. These are for presentation purposes as one would only see vertical lines instead of these parabolic curves if projected into the xy plane.

This experiment is conducted for different values of r, σ_1 pairs. In Table 5.1, the ranges of some of the expected times to tip are displayed. Unlike Cases 1 and 2, the expected time to tip is now finite. The different times to tip between s_1 and s_2, depending on which path taken, demonstrates that tipping without the ramp is extremely rare to the point of almost never tipping. In addition, if there is a ramp parameter but no stochastic component, there is no tipping for when $0 < r < 4/3$. Thus, there is an interplay of additive noise and a ramp parameter, and together they facilitate tipping on a finite timescale.

Notice in Table 5.1 that the expected time to tip for the majority r, σ_1 pairs considered correspond approximately to $t = 0$, implying $y \approx 3/2$. This might be seen as validation that the symmetric extremal calculated in Section 5.3 is indeed close to where the first passages are taking place.

r	σ_1 range	t_0	τ range
0.75	$0.15 - 0.30$	-13.33	$\in (0.07, 0.67)$
0.85	$0.10 - 0.30$	-11.76	$\in (0.04, 0.74)$
1	$0.08 - 0.25$	-10.00	$\in (-0.20, 0.48)$
1.1	$0.08 - 0.25$	-9.09	$\in (-0.29, 0.41)$

Table 5.1: Monte Carlo simulation results for the expected time to tip, τ, for $r = 0.75, 0.85, 1, 1.1$ for different values of σ_1. These times come from converged results of the Monte Carlo simulations using the method described above.

5.4.4 Path Actions

In addition to using Monte Carlo simulations to see how realizations behave and to calculate the expected time to tip, we compute the action along the different path options. The most probable path should be the path of least action. Due to the choice for the p variable in the Legendre transform, for a fixed r, the variation of σ_1 results in a scaling in p. Scaling by some constant does not change the actual minimizer of the functional given by (3.1). Therefore, consider the normalized action when calculating the path actions to make the action more numerically tractable. The normalized action is given by

$$I_N[x] = \int_{t_0}^{t_f} (\dot{x} - f)^2 dt = \int_{t_0}^{t_f} \sigma_1^4 p^2 dt. \tag{5.36}$$

Using (5.36), we find the heteroclinic constructed in Section 5.3, Case 3, has the least action compared to the other two paths of tipping, Cases 1 and 2. If tipping occurs before the ramp starts or after the ramp finishes, the action value is 5.333, but tipping along the most probable path gives the least action value, by multiple orders of magnitude. Table 5.2 displays the comparison of the action size for each of Cases $1-3$ for different r values.

In regards to the action values for Cases 1 and 2 being the same, we first want to stress that both of these paths for tipping are extremely unlikely on reasonable timescales. Practically speaking, the action values are the same when looking along the heteroclinic orbits in the planes $y = 0, 3$ as the p values are the exact same when considering the curves where $H = 0$. The rest of each path lies in $p = 0$, so there is no other contribution to the action. While one might expect it would be easier to track a stable quasi-steady state and then transition, as opposed to transitioning and then tracking an unstable quasi-steady state, we believe it has to do with the compactification, as this brought the dynamics at $\pm\infty$ into the finite world.

Case #	r value	Action
1	-	5.333
2	-	5.333
3	1.1	0.023
3	1	0.054
3	0.75	0.226
3	0.5	0.684

Table 5.2: Action values for Cases 1-3. Cases 1 and 2 do not depend on r as they tip either before or after the ramp. For Case 3, which is dependent on r, we see that for different r values the action is much less than the action of the other paths to tip.

5.5 Discussion and Final Conclusions

5.5.1 The Heteroclinic Orbit as the Most Probable Path

A key observation is the proximity of the heteroclinic orbit to the Monte Carlo KDE most probable path. The KDE most probable path estimate tracks the heteroclinic connection quite closely far beyond the first half of the ramping phase. A consequence of this fact is that we can conclude the heteroclinic connection does carry the realizations that tip through the ramping phase. The heteroclinic connection provides a surprising amount of guidance on how the trajectories that tip do so, especially as we are dealing with not vanishingly small noise: a regime we were forced into because otherwise there would be no interaction of the ramp parameter and additive noise.

Another interpretation for how realizations are tipping would involve considering trajectories following the corresponding deterministic pullback attractor: tipping would occur when $W^u(-1,0)$ and $W^s(-2,3)$ were closest. Running simulations of the noisy system for different values of r and overlaying the tipped realizations with $W^u(-1,0)$ and $W^s(-2,3)$, we see these realizations do not track $W^u(-1,0)$ (when you consider where the tipped realizations are most densely concentrated). As we decrease r, we see the significance of the heteroclinic orbit more clearly as the heteroclinic orbit becomes more distinguishable from the pullback attractor. The realizations that tip closely follow the heteroclinic orbit from the start. However, as r increases, $W^u(-1,0)$ and $W^s(-2,3)$ grow closer together which is why it looks as if the tipped realizations track the pullback attractor for some time.

5.5.2 A Scaling Law for the Expected Time to Tip

For vanishingly small noise, the Freidlin-Wentzell theory of large deviations, which gives the probability of a specific trajectory in a stochastic dynamical system, aids in finding the most probable path between two points. This is obtained by minimizing the Freidlin-Wentzell action functional. This theory also provides the expected time to tip[23]. We saw in this work that Freidlin-Wentzell theory holds in regard to the dynamical structure of the most probable path for small noise strengths. It is still an open question if the expected time to tip aligns between the vanishingly small noise case and the small noise case.

We discovered a power scaling law for the expected time to tip via Monte Carlo simulations, τ, and $1/\sigma_1^2$, for set $r > 0$ and varying values of σ_1. The log-log plot of these coordinate pairs result in a linear relationship, examples of which are shown in Figure 5.9. This linear relationship in log-log space corresponds to a power law of the form $a(\frac{1}{\sigma_1^2})^b$ between $1/\sigma_1^2$ and the expected time to tip. While the scaling laws in Figure 5.9 are

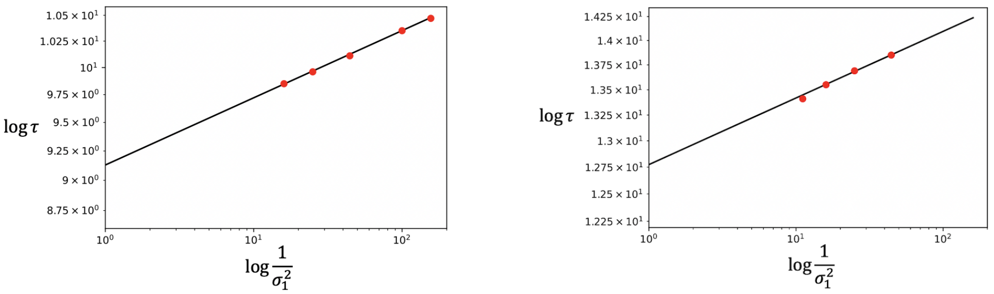

(a) (b)

Figure 5.9: (a) Log-log plot of τ vs. $\frac{1}{\sigma_1^2}$ for $r = 1, \sigma_1 = 0.25, 0.2, 0.15, 0.1, 0.08$. The linear relationship in log-log space corresponds to a power law of the form $9.14(\frac{1}{\sigma_1^2})^{0.027}$. (b) Log-log plot of τ vs. $\frac{1}{\sigma_1^2}$ for $r = 0.75, \sigma_1 = 0.3, 0.25, 0.2, 0.15$. The linear relationship in log-log space corresponds to a power law of the form $12.42(\frac{1}{\sigma_1^2})^{0.021}$.

for $r = 1$ and $r = 0.75$, the linear relationship in log-log space held true for multiple r values we studied. An interesting observation is the slope of the line in log-log space for $r = 1$ in Figure 5.9(a) is the same as the $\frac{1}{2}$(Action Value $r = 1$), the value of which can be seen in Table 5.2.

This scaling law is different from the asymptotic formula given by the Freidlin-Wentzell theory. There are various explanations for this mismatch. The most likely is that we are considering a small noise regime, and not $\sigma_1 \to 0$, and so it is not necessarily surprising the known scaling law does not hold. Alternatively, we have yet to find the leading coefficient, c, which could be dependent on r. We hypothesize that you can find the leading coefficient by finding more expected times to tip and switching perspectives to that of inverse problems.

We believe this task needs to implement importance sampling[45] to aid in speeding up the time required to gather the converged data sets. Importance sampling is commonly used to speed up Monte Carlo simulations of rare events by biasing realizations to those rare events[21].

We would like to point out that Ritchie and Sieber[36] found that for rate values between $r = 1.05$ and $r = 1.25$, that as the noise is decreased, the time to tip increases slowly. They find a similar relationship for the delay in the rate-induced tipping as that of Bakhtin[7] for rare escapes of an autonomous system.

5.5.3 Final Conclusions

Using compactification[44] with a coordinate transformation of the ramp parameter (5.4) allows us to frame the canonical problem as a two-dimensional autonomous system with fixed points and invariant objects, as well as study the heteroclinic connection. We have shown the addition of additive noise causes the system to tip well below the critical rate needed for rate-induced tipping to occur. The system will always have a heteroclinic connection directly between the two saddle equilibria for all $0 < r \leq r_c$. The heteroclinic orbit found using the intersection of invariant manifolds matches the kernel density estimate of the noisy realizations found by Monte Carlo simulations, corroborating it as the most probable path of tipping between these two points. Calculating the action over all the possible paths between the two saddles, we find that the heteroclinic connection we constructed has the least action by multiple orders of magnitude, verifying we have truly found the most probable path between these two points. We find rate and noise-induced tipping conspire to facilitate tipping with increased probability, when neither tip on their own when considering a finite time horizon and $0 < r < r_c$.

We have pushed on the levels of noise to a size where the Freidlin-Wentzell theory may no longer hold as the noise strength was not vanishingly small, though we find that the Freidlin-Wentzell theory actually is still relevant in the extent of the most probable path.

This chapter has considered a one-dimensional canonical problem, but we believe this work can extend to understanding tipping between a base state and a threshold state of similar forms, as we will show in the next chapter. Our methods in this chapter made use of the symmetry within the system. If that symmetry does not exist, other implementations of the Wazewski principle will need to be used to prove that an intersection of the invariant manifolds exist.

CHAPTER 6

Generalizing the Nonlinearity of the Canonical Problem

Chapter 5 illustrated tipping between two saddles in a noisy system all for $r \leq r_c$ by proving the existence of a heteroclinic connection between these two saddles. The proof of Theorem 5.3.5 relied on a special symmetry of the unstable and stable manifolds of these two saddles. Due to this reliance on symmetry, proving the existence of a heteroclinic orbit between two saddle nodes for other problems with both a ramp parameter and noise does not readily extend.

We begin with a one-dimensional differential equation with a ramp parameter. At the start of the problem, we list the necessary assumptions about the function and the ramp parameter, where each assumption will be denoted by $(\mathbf{a_i})$. These assumptions are chosen to ensure a similar structure as seen in Chapter 5, but free enough to have variability and not have to necessarily assume a symmetry of the invariant manifolds.

The system is compactified using the ramp parameter as the coordinate transform, forming a two-dimensional autonomous system. This leads to the last required assumption: the deterministic system first undergoes rate-induced tipping when $r = r_c$ between two saddle nodes. We then consider the addition of additive noise on the compactified system. The Euler-Lagrange equations associated with the Freidlin-Wentzell action functional[23] are derived and used to create a four-dimensional Hamiltonian system, which can be considered in three-dimensional space due to three of the equations being decoupled.

Using a dynamical systems framework, the remainder of the approach is as follows. By assumption, the base saddle has a two-dimensional unstable subspace spanned by its unstable eigenvectors of the linearization, and similarly, the threshold saddle has a two-dimensional stable subspace spanned by its stable eigenvectors.

This is where the methods diverge from those of Chapter 5. We define Wazewski sets for both the forward and backward time systems: W_F and W_B, which will share a boundary at a fixed y value. The unstable manifold of the base saddle is tracked in W_F, and the stable manifold of the threshold saddle is tracked in W_B. For each Wazewski set, we consider a quarter circle lying in the unstable and stable subspace, respectively. The variational equations are then used to track the piece of each manifold carried along the trajectories that begin at the endpoints of the quarter circle, implying they are tracked by tangent vectors. For both the unstable and stable manifolds, the behavior of the tangent vectors as they approach the boundaries of W_F and W_B respectively, need to be determined in terms of their initialization. This reveals how the tangent spaces to the invariant manifolds are carried under the flow.

Then, using the Wazewski principle and shooting methods, it is shown that there is always an intersection of the unstable manifold of the base state and stable manifold of the threshold state. This intersection implies there is a heteroclinic connection between two fixed points for all subcritical rates.

A general schematic of these Wazewski sets and shooting methods as well as the intersection of $W^u(s_1)$ and $W^s(s_2)$ is shown in Figure 6.1. This is not necessarily what the surfaces look like, but this figure does illustrate the bigger picture of this chapter and highlights the approach taken.

Note that this argument only provides the guarantee of a heteroclinic orbit between the base state and the threshold state; it is not a guarantee that the heteroclinic orbit is the most probable path. As noise strengths are small, but not vanishingly small, the Freidlin-Wentzell theory does not imply that the heteroclinic orbit is the most probable path. It is impossible to establish the most probable path in generality. Verifying the heteroclinic orbit is the most probable path requires the use of Monte Carlo simulations, KDE estimates, and the consideration of action values, in which an explicit function, parameter shift, and fixed noise strengths are needed.

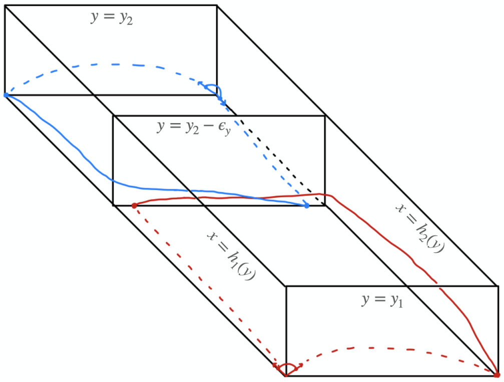

Figure 6.1: W_F is the space bounded by $x = h_1(y), x = h_2(y), y = y_1, y = y_2 - \varepsilon_y$, and $p = 0$ and W_B is the space bounded by $x = h_1(y), x = h_2(y), y = y_2, y = y_2 - \varepsilon_y$, and $p = 0$. Taking a quarter circle of small radius about s_1 intersected with the piece of $W^u(s_1)$ lying in W_F, and applying map K_F, results in the red curve. Taking a quarter circle of small radius about s_2 intersected with the piece of $W^s(s_2)$ lying in W_B, and applying map K_B, results in the blue curve. The blue and red curves intersect in the plane $y = y_2 - \varepsilon_y$.

6.1 The Deterministic System and the Necessary Assumptions

Consider the first-order differential equation

$$\dot{x} = f(x,y), \tag{6.1}$$

where $x \in \mathbb{R}$ and $y = h(rt) \in \mathbb{R}$. The following are the assumptions needed on the parameter shift y.

($\mathbf{a_1}$) The coordinate transform $y = z(rt)$ is a C^2 smooth, monotonically increasing, bi-asymptotically constant external input, that maps the real t-line onto the finite y-interval (y_1, y_2), and has a vanishing first derivative as t tends to $\pm\infty$. The past limit state is y_1 and the future limit state is y_2.

($\mathbf{a_2}$) The coordinate transform $y = z(rt)$ is such that $\dot{y}$ can be rewritten as $\dot{y} = rg(y)$, such that $g(y) = \dot{z}(z^{-1}(y))$, where $g_y(y_1) = A > 0$ and $g_y(y_2) = -A < 0$.

The system is compactified using $y = z(rt)$ as the coordinate transform. By assumptions (a_1) and (a_2), this results in the two-dimensional autonomous system given by

$$\begin{aligned} \dot{x} &= f(x,y), \\ \dot{y} &= rg(y). \end{aligned} \tag{6.2}$$

The following are the assumptions needed on the function $f(x,y)$.

($\mathbf{a_3}$) $f(x,y) \in C^2$.

($\mathbf{a_4}$) $f(x,y_1) = 0$ at $x_1 < x_2 < \ldots < x_n$, and $f(x,y_2) = 0$ at $X_1 < X_2 < \ldots < X_n$.

($\mathbf{a_5}$) The level sets $f(x,y) = 0$ are such that $f(x_0,y_0) = 0$ and $f_x(x_0,y_0) \neq 0$. By the implicit function theorem, let $x = h_1(y), h_2(y), \ldots, h_n(y)$ be the paths that track the zeros of $f(x,y)$ for $y_1 \leq y \leq y_2$, where $h_i(y)$ tracks x_i to X_i.

($\mathbf{a_6}$) $f(x,y) < 0$ for all $y \in [y_1,y_2]$ and $h_1(y) < x < h_2(y)$.

($\mathbf{a_7}$) $f_x(h_1(y),y) < 0$ and $f_x(h_2(y),y) > 0$, as well as $f_y(h_1(y),y) < 0$ and $f_y(h_2(y),y) > 0$.

($\mathbf{a_8}$) $f_x(x_1,y_1) = -b$ and $f_x(x_2,y_1) = b$, where $b > 0$.

($\mathbf{a_9}$) $f_x(X_1,y_2) = -B$ and $f_x(X_2,y_2) = B$, where $B > 0$.

(a$_{10}$) $f_x(x,y_1) = f_y(x,y_1)$ for $x \in [x_1,x_2]$ and $f_x(x,y_2) = f_y(x,y_2)$ for $x \in [X_1,X_2]$.

Solving for fixed points of (6.2), by (a_1) and (a_2), it follows that $\dot{y} = 0$ at $y = y_1$ and $y = y_2$, and by (a_4), when $y = y_1$, $\dot{x} = 0$ at $x = x_1, x_2, ...x_n$, and when $y = y_2$, $\dot{x} = 0$ at $x = X_1, X_2, ...X_n$. The two fixed points (x_1,y_1) and (X_2,y_2) will be the main focus.

The Jacobian matrix of (6.2) is given by

$$\begin{pmatrix} f_x & f_y \\ 0 & rg_y \end{pmatrix}, \tag{6.3}$$

implying both (x_1,y_1) and (X_2,y_2) are saddles, as each has one positive and one negative eigenvalue by assumptions (a_2), (a_8), and (a_{10}), as see in

$$J(x_1,y_1) = \begin{pmatrix} -b & -b \\ 0 & rA \end{pmatrix} \quad , \quad J(X_2,y_2) = \begin{pmatrix} B & B \\ 0 & -rA \end{pmatrix}. \tag{6.4}$$

This leads to the final assumption of the chapter.

> **(a$_{11}$)** The system does not exhibit rate-induced tipping for $r < r_c$, but there is a critical rate r_c such that when $r = r_c$, (6.2) undergoes rate-induced tipping away from (x_1,y_1) to (X_2,y_2).

6.2 Introducing the Stochastic Framework

The underlying deterministic system is such that there is rate-induced tipping away from (x_1,y_1). Now, consider the stochastic version of (6.2) with additive noise, which is of the form

$$\begin{aligned} dx &= f(x,y)dt + \sigma_1 dW_1, \\ dy &= rg(y) + \sigma_2 dW_2, \end{aligned} \tag{6.5}$$

where $r << \leq r_c$. The ultimate goal is to find the most probable path between (x_1,y_1) and (X_2,y_2). Using the minimization process of the Freidlin-Wentzell functional as in Chapter 3, the Euler-Lagrange equations for this system are given by

$$\begin{aligned} \ddot{x} &= f_y\dot{y} + ff_x, \\ \ddot{y} &= gg_y + \frac{\sigma_2^2}{\sigma_1^2}(ff_y - \dot{x}f_y), \end{aligned} \tag{6.6}$$

as $g(x,y) = g(y)$, implying $g_x = 0$. Using the Euler-Lagrange equations given by (6.6), we make a Legendre transform[4] to create a degree four Hamiltonian system. Let

$$p = \frac{\dot{x} - f}{\sigma_1^2} \text{ and } q = \frac{\dot{y} - g}{\sigma_2^2}. \tag{6.7}$$

Following an identical process as in Chapter 5, the degree four Hamiltonian system is of the form

$$\begin{aligned} \dot{x} &= f + \sigma_1^2 p, \\ \dot{p} &= -f_x p, \\ \dot{y} &= g + \sigma_2^2 q, \\ \dot{q} &= -g_y q, \end{aligned} \tag{6.8}$$

and the associated Hamiltonian function is

$$H(x,p,y,q) = fp + gq + \frac{\sigma_1^2}{2}p^2 + \frac{\sigma_2^2}{2}q^2. \tag{6.9}$$

As mentioned earlier, we want to only consider noise on the dynamics of x, as y is a time parameterization, and thus σ_2 is sent to zero. It follows that $\dot{x}, \dot{p}, \dot{y}$ are all independent of q, and so it is possible to project the equations into x, p, y space. To simplify the calculations performed in this chapter, make the change of variables $p = \frac{1}{\sigma_1^2} p$, resulting in the system given by

$$\begin{aligned} \dot{x} &= f + p, \\ \dot{p} &= -f_x p, \\ \dot{y} &= rg, \\ H &= \frac{1}{\sigma_1^2}(fp + \frac{1}{2}p^2), \end{aligned} \tag{6.10}$$

where $f = f(x,y)$ and $g = g(y)$.

On the planes $y = y_1$ and $y = y_2$, there exist Hamiltonian structures, implying the fixed points of the system are all classified as saddles or centers. We are interested in the heteroclinic connection between the saddle points $(x_1, 0, y_1)$ and $(X_2, 0, y_2)$, as these correspond to the saddles (x_1, y_1) and (X_2, y_2) in the two-dimensional phase space. For notation purposes, we will refer to $(x_1, 0, y_1)$ as s_1 and $(X_2, 0, y_2)$ as s_2. To study and understand the unstable and stable directions of s_1 and s_2, we need to linearize both fixed points: the Jacobian matrix is

$$J(x,p,y) = \begin{pmatrix} f_x & 1 & f_y \\ -f_{xx}p & -f_x & -f_{xy}p \\ 0 & 0 & rg_y \end{pmatrix}. \tag{6.11}$$

A quick check of the eigenvalues of (6.11) show s_1 has a one-dimensional stable manifold and a two-dimensional unstable manifold, and s_2 has a one-dimensional unstable manifold and a two-dimensional stable manifold. We denote the unstable and stable manifolds of a point p by $W^u(p)$ and $W^s(p)$ respectively. Using this notation, the desired heteroclinic will lie on both $W^u(s_1)$ and $W^s(s_2)$.

Theorem 6.2.1. *Under assumptions $(a_1)-(a_{11})$, there exists a heteroclinic orbit between s_1 and s_2 for all $0 < r \leq r_c$.*

This theorem is proven by construction throughout the rest of this chapter. To construct the heteroclinic orbit between s_1 and s_2, the transverse intersections of the relevant unstable and stable manifolds of the two fixed points, namely $W^u(s_1)$ and $W^s(s_2)$, need to be found. Determining if a transverse intersection occurs implies understanding the tangent spaces of these manifolds, and so both the forward and backward time systems are considered.

6.3 The Forward Time System

The forward time system is used to track $W^u(s_1)$. At the fixed point s_1, by assumptions (a_2), (a_8), and (a_{10}), (6.11) becomes

$$J(s_1) = \begin{pmatrix} -b & 1 & -b \\ 0 & b & 0 \\ 0 & 0 & rA \end{pmatrix}. \tag{6.12}$$

The unstable eigenvalues are $\lambda_{1,2} = b, rA$ with corresponding eigenvectors $v_{1,2} = (\frac{1}{2b}, 1, 0), (\frac{-b}{b+rA}, 0, 1)$.

Recall the Wazewski principle given in Proposition 5.3.2. For the system given in (6.10), the Wazewski set, W_F, is the space bounded by the following two-dimensional surfaces: $x = h_1(y)$, $x = h_2(y)$, $y = y_1$, $y = y_2 - \varepsilon_y$, and $p = 0$, and extends infinitely in the positive p direction. Based on flow of the vector field, the following are true about the boundaries of W_F: $y = y_1$ and $p = 0$ are neither entrance nor exit sets as they are invariant planes, $y = y_2 - \varepsilon_y$ is an exit set as $\dot{y} > 0$, $x = h_1(y)$ is an entrance set, by Claim 6.3.1, and $x = h_2(y)$ is an exit set by similar calculations as shown in the proof of Claim 6.3.1.

Claim 6.3.1. *The surface $x = h_1(y)$ is an entrance set.*

Proof. The normal vector to the surface $x = h_1(y)$ is $(f_x(h_1(y),y),0,f_y(h_1(y),y))$. Recall $f_x(h_1(y),y)$ and $f_y(h_1(y),y)$ have the same sign by (a_7). By the right hand rule, the orientation of this normal vector is such that $f_x(h_1(y),y) > 0$ and $f_y(h_1(y),y) > 0$. Then,

$$\begin{aligned}(\dot{x},\dot{p},\dot{y})\cdot(f_x(h_1(y),y),0,f_y(h_1(y),y)) &= (f(h_1(y),y)+p)f_x(h_1(y),y)+rgf_y(h_1(y),y)\\ &= pf_x(h_1(y),y)+rgf_y(h_1(y),y)\\ &> 0,\end{aligned} \tag{6.13}$$

by the assumptions for $y \in [y_1, y_2 - \varepsilon_y]$, as long it is not the fixed point s_1. So $x = h_1(y)$ is an entrance set. □

Now we need to determine the eventual exit set of W_F, W_F^0. Recall that based on the eigenvalues of $J(s_1)$, s_1 has a two-dimensional unstable manifold and a one-dimensional stable manifold. The unstable subspace is spanned by the unstable eigenvectors of $J(s_1)$, v_1 and v_2. Taking the plane spanned by v_1 and v_2, intersected with a small ball around s_1, gives rise to a quarter circle in the unstable subspace of s_1. We call the point of this quarter circle rooted in $p = 0$, a_1, and the point of this quarter circle rooted in $y = y_1$, a_2. The goal is to show that as this quarter circle flows in time, some of it exits through $y = y_2 - \varepsilon_y$ and some of it exits through $x = h_2(y)$.

Assume by way of contradiction that W_F^0 is empty, implying that the flow acting on the quarter circle would need to stay within W_F for all time. However, W_F^0 must be nonempty since a_1 will eventually exit through $y = y_2 - \varepsilon_y$ as $\dot{y} > 0$ and $r \leq r_c$. This argument guarantees that some of the quarter circle exits through the plane $y = y_2 - \varepsilon_y$.

6.3.1 Tracking the Tangent Space

To show that some of the quarter circle exits through $x = h_2(y)$, the tangent space of $W^u(s_1)$ is tracked using the variational equations, by studying the evolution of the normal vector to the unstable manifold of s_1 on $y = y_1$.

The variational equations for (6.10) are

$$\begin{aligned}\delta\dot{x} &= f_x\delta x + f_y\delta y + \delta p\\ \delta\dot{p} &= -f_{xx}p\delta x - f_{xy}p\delta y - f_x\delta p\\ \delta\dot{y} &= rg_y\delta y\end{aligned} \tag{6.14}$$

Consider two solutions of (6.14)

$$\begin{aligned}\eta_1 &= (\delta x_1, \delta p_1, \delta y_1),\\ \eta_2 &= (\delta x_2, \delta p_2, \delta y_2),\end{aligned} \tag{6.15}$$

such that η_1 is the vector field itself. Both η_1 and η_2 are tangent to the unstable manifold of s_1 and thus $\eta_1 \times \eta_2 = (\psi, \lambda, \omega)$ is normal to it. The idea is that for x sufficiently close to $x = h_2(y)$, if the tangent vector is pointing in the positive y and p directions, it will have to exit $x = h_2(y)$ as there will be no time for the trajectories to exit elsewhere. It must be determined how the tangent vector of $W^u(s_1)$ behaves when $x = x_2 - \varepsilon$. The normal vector to the plane $x = x_2 - \varepsilon$ is given by $(1,0,0)$, and to determine the behavior of the tangent vector of $W^u(s_1)$ when $x = x_2 - \varepsilon$, we consider

$$(\psi, \lambda, \omega) \times (1,0,0) = (0, \omega, -\lambda). \tag{6.16}$$

In y-p space, the tangent vector $(0, \omega, -\lambda)$ will have a slope of $\frac{\omega}{-\lambda}$ when $x = x_2 - \varepsilon$ and $y = y_1$. The goal is to show this tangent vector points in the positive y and positive p directions, and so $\frac{\omega}{-\lambda}$ needs to be positive. Note that the vector (ψ, λ, ω) at $x = x_1$ can be determined using the unstable eigenvectors from the linearization at s_1, $(\frac{1}{2b}, 1, 0)$ and $(\frac{-b}{b+rA}, 0, 1)$, as they are tangent to the unstable manifold of s_1 at $x = x_1$ and $y = y_1$. Taking the cross product of these vectors results in the normal vector

$$\left(\frac{1}{2b}, 1, 0\right) \times \left(\frac{-b}{b+rA}, 0, 1\right) = \left(1, \frac{-1}{2b}, \frac{b}{b+rA}\right). \tag{6.17}$$

As $t \to -\infty$, the behavior of (ψ, λ, ω) is written as $(1, \frac{-1}{2b}, \frac{b}{b+rA})Ce^{dt}$, which at s_1 results in $(\psi, \lambda, \omega) = (0,0,0)$.

To track the normal vector, we study how it is changing by using the components of the derivative of $\eta_1 \times \eta_2$ with respect to time. Using properties of the cross product,

$$\frac{d}{dt}(\eta_1 \times \eta_2) = \left(\frac{d\eta_1}{dt} \times \eta_2 + \eta_1 \times \frac{d\eta_2}{dt}\right). \tag{6.18}$$

Recall $\lambda = \eta_1 \times \eta_2 \cdot j$. Differentiating λ,

$$\begin{aligned}\dot{\lambda} &= \left(\frac{d\eta_1}{dt} \times \eta_2 + \eta_1 \times \frac{d\eta_2}{dt}\right) \cdot j \\ &= \delta\dot{y}_1\delta x_2 - \delta\dot{x}_1\delta y_2 + \delta y_1\delta\dot{x}_2 - \delta x_1\delta\dot{y}_2 \\ &= rg_y\delta y_1\delta x_2 - (f_x\delta x_1 + f_y\delta y_1 + \delta p_1)\delta y_2 + \delta y_1(f_x\delta x_2 + f_y\delta y_2 + \delta p_2) - \delta x_1 rg_y\delta y_2 \\ &= rg_y\delta y_1\delta x_2 - (f_x\delta x_1 + \delta p_1)\delta y_2 + \delta y_1(f_x\delta x_2 + \delta p_2) - \delta x_1 rg_y\delta y_2.\end{aligned} \tag{6.19}$$

This expression can be simplified using the fact that $\delta x_1, \delta p_1$, and δy_1 are the vector field itself by assumption. Consequently, the right-hand side of (6.10) can be substituted into equation (6.19). Additionally, we consider this expression when $y = y_1$, implying the system is Hamiltonian. Rearranging $H = 0$ implies $p = -2f(x, y_1)$, and so (6.19) becomes

$$\begin{aligned}\dot{\lambda} &= -[f_x(f+p) - f_x p]\delta y_2 - (f+p)rg_y\delta y_2 \\ &= -[f_x(-f) - f_x(-2f)]\delta y_2 - (-f)rg_y\delta y_2 \\ &= [-ff_x + rg_y f]\delta y_2.\end{aligned} \tag{6.20}$$

It is possible to explicitly solve for δy_2 using the third equation of (6.14) with separation of variables. Solving, $\delta y_2 = ce^{rg_y(y_1)t} = ce^{rAt}$ by (a_2). Assume without loss of generality that $c > 0$, though it does not matter as it will cancel in the expression $\frac{w}{-\lambda}$. It follows that (6.20) simplifies to

$$\dot{\lambda} = [-f_x(x, y_1)f(x, y_1) + rAf(x, y_1)]ce^{rAt}. \tag{6.21}$$

By similar calculations,

$$\begin{aligned}\dot{\omega} &= \left(\frac{d\eta_1}{dt} \times \eta_2 + \eta_1 \times \frac{d\eta_2}{dt}\right) \cdot k \\ &= \delta\dot{x}_1\delta p_2 - \delta\dot{p}_1\delta x_2 + \delta x_1\delta\dot{p}_2 - \delta p_1\delta\dot{x}_2 \\ &= [-2f_{xy}(x, y_1)f^2(x, y_1) - 2f_y(x, y_1)f_x(x, y_1)f(x, y_1)]ce^{rAt}.\end{aligned} \tag{6.22}$$

To solve for λ and ω, it is necessary to integrate both (6.21) and (6.22), though solving for λ is a more straightforward calculation. The left hand side of (6.21) is equivalent to $\frac{d\lambda}{dt}$, and so rewrite (6.21) as

$$d\lambda = [-f_x(x, y_1)f(x, y_1) + rAf(x, y_1)]ce^{rAt}dt. \tag{6.23}$$

A consequence of the Hamiltonian structure on $y = y_1$ is the fact that $dt = \frac{-1}{f(x,y_1)}dx$, and so (6.23) turns into

$$\begin{aligned} d\lambda &= [-f_x(x,y_1)f(x,y_1) + rAf(x,y_1)]ce^{rAt}\left(\frac{-1}{f(x,y_1)}\right)dx \\ &= [f_x(x,y_1) - rA]ce^{rAt}dx, \end{aligned} \tag{6.24}$$

which changes the variable of integration to x. Integrating over $x = x_1$ to $x = x_2 - \varepsilon$, implies

$$\begin{aligned} \int_{x=x_1}^{x=x_2-\varepsilon} d\lambda &= \int_{x_1}^{x_2-\varepsilon} [f_x(x,y_1) - rA]ce^{rAt}dx \\ &= \int_{x_1}^{x_2-\varepsilon} cf_x(x,y_1)e^{rAt}dx - \int_{x_1}^{x_2-\varepsilon} crAe^{rAt}dx. \end{aligned} \tag{6.25}$$

Apply integration by parts on $\int_{x_1}^{x_2-\varepsilon} cf_x(x,y_1)e^{rAt}dx$ with $u = ce^{rAt}$ and $dv = f_x dx$, resulting in (6.25) to become

$$\begin{aligned} \int_{x=x_1}^{x=x_2-\varepsilon} d\lambda &= cf(x,y_1)e^{rAt}\Big|_{x_1}^{x_2-\varepsilon} - \int_{x_1}^{x_2-\varepsilon} crA\frac{dt}{dx}f(x,y_1)e^{rAt}dx - \int_{x_1}^{x_2-\varepsilon} crAe^{rAt}dx \\ &= cf(x,y_1)e^{rAt}\Big|_{x_1}^{x_2-\varepsilon} + \int_{x_1}^{x_2-\varepsilon} crAe^{rAt}dx - \int_{x_1}^{x_2-\varepsilon} crAe^{rAt}dx \\ &= cf(x,y_1)e^{rAt}\Big|_{x_1}^{x_2-\varepsilon} \end{aligned} \tag{6.26}$$

Notice, using the fundamental theorem of calculus to solve the final line of the right hand side of (6.26) only relies on knowing the behavior of $cf(x,y_1)e^{rAt}$ at $x = x_1$ and $x = x_2 - \varepsilon$. We can exploit the asymptotic behaviors at these points to understand the relationship between x and t. The asymptotic behaviors occurring near x_1 and x_2 are given by

$$\begin{aligned} \lim_{t\to-\infty} \frac{x - x_1}{c_1e^{bt}} &= 1 \to x \sim x_1 + c_1e^{bt}, \\ \lim_{t\to\infty} \frac{x_2 - x}{c_2e^{-bt}} &= 1 \to x \sim x_2 - c_2e^{-bt}, \end{aligned} \tag{6.27}$$

where we assume that $x_2 - \varepsilon$ corresponds to some $t > T$ sufficiently large so that this asymptotic behavior is true near $x = x_2 - \varepsilon$. Rearranging the asymptotic relationships show t can be written as a function of x,

$$\begin{aligned} x \sim x_1 + c_1e^{bt} &\implies t \sim \frac{1}{b}\ln\left(\frac{x - x_1}{c_1}\right), \\ x \sim x_2 - c_2e^{-bt} &\implies t \sim \frac{-1}{b}\ln\left(\frac{x_2 - x}{c_2}\right). \end{aligned} \tag{6.28}$$

Using these asymptotic behaviors, (6.26) becomes

$$\begin{aligned} \lambda(x_2-\varepsilon)-\lambda(x_1) &\sim \lim_{x\to x_2-\varepsilon} cf(x,y_1)\left(\frac{x_2-x}{c_2}\right)^{-rA/b} - \lim_{x\to x_1} cf(x,y_1)\left(\frac{x-x_1}{c_1}\right)^{rA/b} \\ &= cf(x_2-\varepsilon,y_1)(\varepsilon/c_2)^{-rA/b} - cf(x_1,y_1)(0)^{rA/b} \\ &= cf(x_2-\varepsilon,y_1)(\varepsilon/c_2)^{-rA/b} \end{aligned} \tag{6.29}$$

By (a_6), $cf(x_2-\varepsilon,y_1)(\varepsilon/c_2)^{-rA/b}<0$, and because $\lambda(x_1)=0$,

$$\lambda(x_2-\varepsilon)<0. \tag{6.30}$$

A similar set of calculations and simplifications are used to solve for ω from $\dot{\omega}$ as above, beginning with

$$\begin{aligned} d\omega &= [-2f_{xy}(x,y_1)f^2(x,y_1)-2f_y(x,y_1)f_x(x,y_1)f(x,y_1)]ce^{rAt}dt \\ &= [2f_{xy}(x,y_1)f(x,y_1)+2f_y(x,y_1)f_x(x,y_1)]ce^{rAt}dx. \end{aligned} \tag{6.31}$$

Integrating over $x=x_1$ to $x=x_2-\varepsilon$, implies

$$\int_{x_1}^{x_2-\varepsilon} d\omega = \int_{x_1}^{x_2-\varepsilon} 2f_{xy}(x,y_1)f(x,y_1)ce^{rAt}dx + \int_{x_1}^{x_2-\varepsilon} 2f_y(x,y_1)f_x(x,y_1)ce^{rAt}dx. \tag{6.32}$$

Apply integration by parts twice and use (a_{10}), to find

$$\int_{x_1}^{x_2-\varepsilon} d\omega = 2cf(x,y_1)f_y(x,y_1)e^{rAt}\Big|_{x_1}^{x_2-\varepsilon} + 2crAf(x,y_1)e^{rAt}\Big|_{x_1}^{x_2-\varepsilon} + \int_{x_1}^{x_2-\varepsilon} 2cr^2A^2e^{rAt}dx, \tag{6.33}$$

at which point, the asymptotic behaviors in (6.28) are used

$$\int_{x_1}^{x_2-\varepsilon} d\omega \sim 2cf(x_2-\varepsilon,y_1)f_x(x_2-\varepsilon,y_1)(\varepsilon/c_2)^{-rA/b} + 2crAf(x_2-\varepsilon,y_1)(\varepsilon/c_2)^{-rA/b} + \int_{x_1}^{x_2-\varepsilon} 2cr^2A^2e^{rAt}dx. \tag{6.34}$$

The first two terms of the right hand side of (6.34) are negative while the integral is a positive quantity, implying the sign of these three terms is inconclusive. However, the integral in (6.34) can be further analyzed by first expanding it into three components, and then using the asymptotic behaviors in (6.28) to simplify it as

$$
\begin{aligned}
\int_{x_1}^{x_2-\varepsilon} 2cr^2A^2e^{rAt}dx &= \int_{x_1}^{x_1+\delta} 2cr^2A^2e^{rAt}dx + \int_{x_1+\delta}^{x_2-\delta} 2cr^2A^2e^{rAt}dx + \int_{x_2-\delta}^{x_2-\varepsilon} 2cr^2A^2e^{rAt}dx \\
&\sim \int_{x_1}^{x_1+\delta} 2cr^2A^2(x-x_1)^{rA/b}dx + \int_{x_1+\delta}^{x_2-\delta} 2cr^2A^2e^{rAt}dx + \int_{x_2-\delta}^{x_2-\varepsilon} 2cr^2A^2(x_2-x)^{-rA/b}dx \\
&= \frac{2cr^2A^2b}{rA+b}(x-x_1)^{rA/b+1}\Big|_{x_1}^{x_1+\delta} + \int_{x_1+\delta}^{x_2-\delta} 2cr^2A^2e^{rAt}dx + \frac{2cr^2A^2}{rA-b}(x_2-x)^{-rA/b+1}\Big|_{x_2-\delta}^{x_2-\varepsilon} \\
&= \frac{2cr^2A^2b}{rA+b}(\delta)^{rA/b+1} + \int_{x_1+\delta}^{x_2-\delta} 2cr^2A^2e^{rAt}dx + \frac{2cr^2A^2}{rA-b}(\varepsilon^{1-rA/b} - \delta^{1-rA/b}).
\end{aligned}
\tag{6.35}
$$

This further analysis of the integral allows (6.34) to be written as

$$
\begin{aligned}
\int_{x_1}^{x_2-\varepsilon} d\omega \sim & 2cf(x_2-\varepsilon,y_1)f_x(x_2-\varepsilon,y_1)(\varepsilon)^{-rA/b} + 2crAf(x_2-\varepsilon,y_1)(\varepsilon)^{-rA/b} \\
& + \frac{2cr^2A^2b}{rA+b}(\delta)^{rA/b+1} + \int_{x_1+\delta}^{x_2-\delta} 2cr^2A^2e^{rAt}dx + \frac{2cr^2A^2}{rA-b}(\varepsilon^{1-rA/b} - \delta^{1-rA/b}).
\end{aligned}
\tag{6.36}
$$

If we consider the limit of (6.36) as $\varepsilon \to 0$, L'Hopital's rule is used to show that there exists ε sufficiently small such that the positive terms dominate over the negative terms. While these calculations are omitted, there are three cases to consider: $\frac{rA}{b} < 1$, $\frac{rA}{b} = 1$, $\frac{rA}{b} > 1$, though all cases have the same result. Since the right hand side of (6.36) is a positive quantity, and $\omega(x_1) = 0$,

$$
\omega(x_2-\varepsilon) > 0. \tag{6.37}
$$

In y-p space, the tangent vector $(0,\omega,-\lambda)$ has slope $\frac{\omega}{-\lambda} > 0$ when $x = x_2 - \varepsilon$ and $y = y_1$ using (6.30) and (6.37), which points in the positive y and positive p directions. This implies that some of the quarter circle must exit through $x = h_2(y)$ under the flow.

We conclude the following about the immediate exit set and eventual exit set of W_F:

$$
\begin{aligned}
W_F^- &= \{(x,p,y) \mid y = y_2 - \varepsilon, x = h_2(y)\}, \\
W_F^0 &= \{(x,p,y) \mid W \setminus \{y = y_1, x = h_1(y), p = 0, (x_1,0,y_1), (x_2,0,y_2)\}\}.
\end{aligned}
$$

It follows that W_F^- is closed relative to W_F^0, implying W_F is a Wazewski set and the map $K_F : W_F^0 \to W_F^-$ is continuous for $y \le y_2 - \varepsilon$. For subcritical rates, the flow takes a_1 to $(X_1,0,y_2)$ in $p = 0$, exiting through $y = y_2 - \varepsilon$, it takes a_2 to $(x_1,0,y_2)$ in the plane $y = y_1$, and it takes some point near a_2 on the quarter circle, call it a_{2c}, through $x = h_2(y)$. We know where a_1 and a_{2c} map to under K_F, and since K_F is a continuous map, there is a continuous curve in W_F^- connecting the exit locations of a_1 and a_{2c}.

6.4 The Backward Time System

Before $W^s(s_2)$ is tracked in the backward time system, notice at the fixed point s_2, by assumptions (a_2), (a_8), and (a_{10}), (6.11) becomes

$$J(s_2) = \begin{pmatrix} B & 1 & B \\ 0 & -B & 0 \\ 0 & 0 & -rA \end{pmatrix}. \tag{6.38}$$

The stable eigenvalues are $\lambda_{3,4} = -B, -rA$ with corresponding eigenvectors $v_{3,4} = (\frac{-1}{2B}, 1, 0), (\frac{-B}{B+rA}, 0, 1)$, and so there is a two-dimensional stable manifold of s_2.

The stable subspace is spanned by the stable eigenvectors of $J(s_1)$, v_3 and v_4. Taking the plane spanned by v_3 and v_4, intersected with a small ball around s_2, gives rise to a quarter circle in the stable subspace of s_2. We call the point of this quarter circle rooted in $p = 0$, a_3, and the point of this quarter circle rooted in $y = y_2$, a_4.

Making the change of variables $\tau = -t$, results in the backward time system

$$\begin{aligned} x' &= -f - p, \\ p' &= f_x p, \\ y' &= -rg, \end{aligned} \tag{6.39}$$

where $f = f(x,y)$ and $g = g(y)$.

Let W_B be the space bounded by the following two-dimensional surfaces: $x = h_1(y)$, $x = h_2(y)$, $y = y_2$, $y = y_2 - \varepsilon_y$, and $p = 0$, and extends infinitely in the positive p direction. Based on flow of the vector field, the following are true about the boundaries of W_B: $y = y_2$ and $p = 0$ are neither entrance nor exit sets as they are invariant planes, $y = y_2 - \varepsilon_y$ is an exit set, $x = h_1(y)$ is an exit set and $x = h_2(y)$ is an entrance set. Similar calculations as shown in the proof of Claim 6.3.1 show $x = h_1(y)$ is an exit set, and $x = h_2(y)$ is an entrance set.

The goal is to show that as this quarter circle flows in backward time, some of it exits through $y = y_2 - \varepsilon_y$ and some of it exits through $x = h_1(y)$. Now we need to determine the eventual exit set of W_B, W_B^0. First assume by way of contradiction that W_B^0 is empty, implying that the flow acting on the quarter circle would need to stay within W_B for all time. However, W_B^0 must be nonempty since a_3 will eventually exit through

$y = y_2 - \varepsilon_y$ as $y' < 0$ and $r \leq r_c$. This argument guarantees that some of the quarter circle exits through the plane $y = y_2 - \varepsilon_y$.

6.4.1 Tracking the Tangent Space

To show that some of the quarter circle exits through $x = h_1(y)$, tangent space of $W^s(s_2)$ is tracked using the variational equations of (6.39), by studying the evolution of the normal vector to the stable manifold of s_2 on $y = y_2$.

The idea is that for x sufficiently close to $x = h_1(y)$, if the tangent vector is pointing in the negative y and positive p directions, it will have to exit $x = h_1(y)$, as there will be no time for the trajectories to exit elsewhere. It must be determined how the tangent vector of $W^s(s_2)$ behaves when $x = X_1 + \varepsilon$. The calculations of tracking the normal vector to the tangent space of the stable manifold of s_2 are omitted as the calculations are nearly identical to that of the forward time system. It can be concluded through these calculations that the tangent vector does point in the negative y and positive p directions, implying that some of the quarter circle must exit through $x = h_1(y)$ under the flow.

We conclude the following about the immediate exit set and eventual exit set of W_B:

$$W_B^- = \{(x,p,y) \mid y = y_2 - \varepsilon, x = h_1(y)\},$$
$$W_B^0 = \{(x,p,y) \mid W \setminus \{y = y_2, x = h_2(y), p = 0, (X_1,0,y_2), (X_2,0,y_2)\}\}.$$

It follows that W_B^- is closed relative to W_B^0, implying W_B is a Wazewski set and the map $K_B : W_B^0 \to W_B^-$ is continuous for $y \leq y_2 - \varepsilon$. For subcritical rates, the flow takes a_3 to $(x_2,0,y_1)$ in $p = 0$, exiting through $y = y_2 - \varepsilon_y$, it takes a_4 to $(X_1,0,y_2)$ in the plane $y = y_2$, and it takes some point near a_4 on the quarter circle, call it a_{4c}, through $x = h_1(y)$. We know where a_3 and a_{4c} map to under K_B, and since K_B is a continuous map, there is a continuous curve in W_B^- connecting the exit locations of a_3 and a_{4c}.

6.5 Bringing the Forward and Backward Time Systems Together

Both quarter circles in the unstable subspace of s_1 and the stable subspace of s_2 are continuous closed curves. By applying a shooting method on both sets of points a_1, a_{2c} and a_3, a_{4c}, we know there is a continuous curve in W_F^- connecting the exit locations of a_1 and a_{2c} as well as a continuous curve in W_B^- connecting the exit locations of a_3 and a_{4c}.

For all rates $r \leq r_c$, these two curves will always intersect in the plane $y = y_2 - \varepsilon_y$, implying the existence of a transverse intersection of $W^u(s_1)$ and $W^s(s_2)$ in $y = y_2 - \varepsilon_y$, which proves there is always a heteroclinic orbit between these two saddle points.

6.5.1 Discussion and Final Conclusions

An artifact of this argument is that it truly only works for subcritical rates $r < r_c$ and the critical rate $r = r_c$. Tracking the points a_1 and a_3 in the plane $p = 0$ under the flow show the only way an intersection of the invariant manifolds is guaranteed is if the x value of a_1 is less than or equal to the x value of a_3, implying $r \leq r_c$. If the x value of a_1 is greater than the x value of a_3, the shooting method does not guarantee an intersection. The schematics of these cases are shown in Figure 6.2.

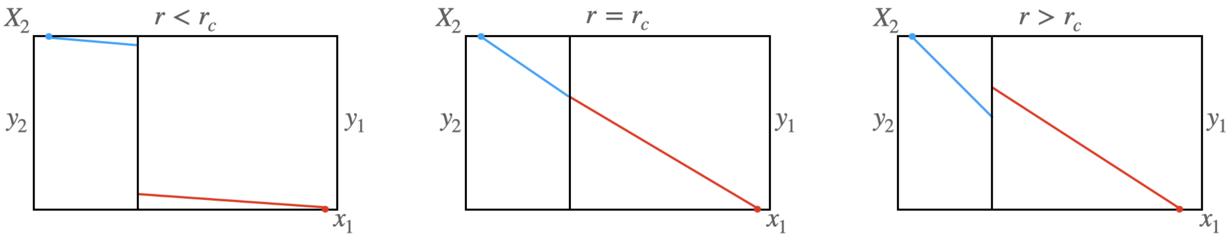

Figure 6.2: A schematic tracking a_1 (red circle) and a_3 (blue circle) under the flow for different values of r in the plane $p = 0$.

The purpose of this chapter was to provide an alternative method for proving the existence of a heteroclinic connection between two saddle fixed points, that can be used to show tipping occurs between these two points for subcritical rates. While the framework provided works for a fairly general class of functions, it still does rely on some specific structures of the underlying system. This method can still be used for proving the existence of a heteroclinic orbit for functions that do not exactly fit this exact type of nonlinearity, but it would need to be considered on a case by case basis.

CHAPTER 7

Conclusions

This dissertation developed tools for rate-induced tipping, noise-induced tipping, and their interaction, for noise strengths away from the small noise limit. The driving question explored was understanding what information can be extracted from the theory of large deviations for noise levels outside the validity of the approach, where the guiding principles were geometric dynamical systems methods and Monte Carlo simulations.

In Chapter 4, we explored a model of the oceanic carbon cycle, and focused on the escape from a fixed point through an unstable periodic orbit, both due to a time-dependent parameter as well as noise, but as separate phenomena. We are the first to show that the system is susceptible to rate-induced tipping in the deterministic system. When the noisy system is considered, we find that for small noise strengths away from the limit the escaping paths become resistant to cycling, differing from the behavior in the small noise limit: realizations should cycle around the unstable periodic orbit[16]. We expose that a subset of the unstable manifold of the fixed point in the Euler-Lagrange system, with Maslov index zero, determines where the noisy trajectories escape.

The only work, to our knowledge, of studying rate-induced tipping in noisy systems is that of Ritchie and Sieber[36, 37]. We further develop this theory by considering a one-dimensional differential equation with both additive noise away from the small noise limit and a ramp parameter in Chapter 5. The addition of noise to the system can cause it to tip well below the critical rate at which rate-induced tipping would occur. We achieve this by finding a global minimizer of the Freidlin-Wentzell functional of large deviation theory that represents the most probable path for tipping. This is realized as a heteroclinic connection for the Euler-Lagrange system associated with the Freidlin-Wentzell action and we show it exists for all rates less than or equal to the critical rate. We prove that the structure of the most probable path predicted by Freidlin-Wentzell theory still holds true away from the small noise limit. We also extended this work to show the existence of a heteroclinic orbit for a fairly general class of functions in Chapter 6.

REFERENCES

[1] Aletti, G., Naldi, G., and Toscani, G. (2007). First-order continuous models of opinion formation. *SIAM Journal on Applied Mathematics*, 67(3):837–853.

[2] Andreoni, J., Nikiforakis, N., and Siegenthaler, S. (2021). Predicting social tipping and norm change in controlled experiments. *Proceedings of the National Academy of Sciences*, 118(16):e2014893118.

[3] Andreoni, J., Nikiforakis, N., and Siegenthaler, S. (2021 [Online]). Social tipping points and forecasting norm change. *CEPR*. cepr.org/voxeu/columns/social-tipping-points-and-forecasting-norm-change.

[4] Arnold, V. I. (1997). *Mathematical methods of classical mechanics*. Number 60 in Graduate Texts in Mathematics. Springer, New York, 2nd edition.

[5] Ashwin, P., Perryman, C., and Wieczorek, S. (2017). Parameter shifts for nonautonomous systems in low dimension: Bifurcation- and Rate-induced tipping. *Nonlinearity*, 30(6):2185–2210.

[6] Ashwin, P., Wieczorek, S., Vitolo, R., and Cox, P. (2012). Tipping points in open systems: bifurcation, noise-induced and rate-dependent examples in the climate system. *Philosophical Transactions of the Royal Society A: Mathematical, Physical and Engineering Sciences*, 370(1962):1166–1184.

[7] Bakhtin, Y. (2013). On Gumbel limit for the length of reactive paths. arXiv:1312.1939.

[8] Berestycki, H., Nadal, J., and Rodiguez, N. (2015). A model of riots dynamics: shocks, diffusion and thresholds. *Networks and Heterogeneous Media*, 10(3):443–475.

[9] Berglund, N. (2011). Kramers' law: validity, derivations and generalisations. *Markov Processes and Related Fields*, 19.

[10] Beri, S., Mannella, R., Luchinsky, D., Silchenko, A., and McClintock, P. (2005). Solution of the boundary value problem for optimal escape in continuous stochastic systems and maps. *Physical Review E*, 72(3):036131.

[11] Bonnasse-Gahot, L., Berestycki, H., Depuiset, M., Gordon, M., Roche, S., Rodriguez, N., and Nadal, J. (2018). Epidemiological modelling of the 2005 French riots: a spreading wave and the role of contagion. *Scientific Reports*, 8(1):107.

[12] Cameron, M. (2012). Finding the quasipotential for nongradient sdes. *Physica D: Nonlinear Phenomena*, 241(18):1532–1550.

[13] Chao, Y. and Duan, J. (2019). The onsager–machlup function as lagrangian for the most probable path of a jump-diffusion process. *Nonlinearity*, 32(10):3715–3741.

[14] Chu, J. (2019 [Online]). Breaching a "carbon threshold" could lead to mass extinction. *MIT News*. news.mit.edu/2019/carbon-threshold-mass-extinction-0708.

[15] Collins M., M. Sutherland, L. Bouwer, S. Cheong, T. Frolicher, H. Jacot Des Combes, M. Koll Roxy, I. Losada, K. McInnes, B. Ratter, E. Rivera-Arriaga, R.D. Susanto, D. Swingedouw, and L. Tibig (2019). *Extremes, Abrupt Changes and Managing Risk*, pages 589–655. Cambridge University Press.

[16] Day, M. V. (1996). Exit cycling for the Van der Pol oscillator and quasipotential calculations. *Journal of Dynamics and Differential Equations*, 8(4):573–601.

[17] Day, M. V. and Darden, T. A. (1985). Some regularity results on the ventcel-freidlin quasi-potential function. *Applied Mathematics and Optimization*, 13:259–282.

[18] Dhooge, A., Govaerts, W., and Kuznetsov, Y. A. (2003). Matcont: A matlab package for numerical bifurcation analysis of odes. *ACM Transactions on Mathematical Software*, 29(2):141–164.

[19] Dodge, Y. (2008). Kolmogorov-Smirnov test. In *The Concise Encyclopedia of Statistics*, pages 283–287. Springer, New York, NY.

[20] Fleurantin, E., Slyman, K., Barker, B., and Jones, C. K. R. T. (2023). A dynamical systems approach for most probable escape paths over periodic boundaries. arXiv:2302.00758.

[21] Forgoston, E. and Moore, R. O. (2018). A primer on noise-induced transitions in applied dynamical systems. *SIAM Review*, 60(4):969–1009.

[22] Freedman, D. and Diaconis, P. (1981). On the histogram as a density estimator: L_2 theory. *Zeitschrift fur Wahrscheinlichkeitstheorie und Verwandte Gebiete*, 57(4):453–476.

[23] Freidlin, M. I. and Wentzell, A. D. (2012). *Random Perturbations of Dynamical Systems*, volume 260 of *Grundlehren der mathematischen Wissenschaften*. Springer, Berlin, Heidelberg.

[24] Higham., D. J. (2001). An Algorithmic Introduction to Numerical Simulation of Stochastic Differential Equations. *SIAM Review*, 43(3):525–546.

[25] Jones, C. K. R. T. (1995). *Geometric singular perturbation theory*, pages 44–118. Springer Berlin Heidelberg, Berlin, Heidelberg.

[26] Kaszas, B., Feudel, U., and Tel, T. (2019). Tipping phenomena in typical dynamical systems subjected to parameter drift. *Scientific Reports*, 9(8654).

[27] Kemp, L., Xu, C., Depledge, J., Ebi, K., Gibbins, G., Kohler, T., Rockstrom, J., Scheffer, M., Schellnhuber, H., Steffen, W., and Lenton, T. (2022). Climate endgame: exploring catastrophic climate change scenarios. *Proceedings of the National Academy of Sciences*, 119(34):e2108146119.

[28] Kiers, C. (2020). Rate-induced tipping in discrete-time dynamical systems. *SIAM Journal on Applied Dynamical Systems*, 19(2):1200–1224.

[29] Kiers, C. and Jones, C. (2019). On conditions for rate-induced tipping in multi-dimensional dynamical systems. *Journal of Dynamics and Differential Equations*.

[30] Lenton, T. M. (2011). Early warning of climate tipping points. *Nature Climate Change*, 1(4):201–209.

[31] Lenton, T. M., Held, H., Kriegler, E., Hall, J. W., Lucht, W., Rahmstorf, S., and Schellnhuber, H. J. (2008). Tipping elements in the Earth's climate system. *Proceedings of the National Academy of Sciences*, 105(6):1786–1793.

[32] National Oceanic and Atmospheric Administration (2013 [Online]). Ocean acidification. www.noaa.gov/education/resource-collections/ocean-coasts-education-resources/ocean-acidification.

[33] Nolting, B. C. and Abbott, K. C. (2016). Balls, cups, and quasi-potentials: quantifying stability in stochastic systems. *Ecology*, 97(4):850–864.

[34] Otto, I. M., Donges, J. F., Cremades, R., Bhowmik, A., Hewitt, R. J., Lucht, W., Rockstrom, J., Allerberger, F., McCaffrey, M., Doe, S., Lenferna, A., Moran, N., van Vuuren, D. P., and Schellnhuber, H. J. (2020). Social tipping dynamics for stabilizing earth's climate by 2050. *Proceedings of the National Academy of Sciences*, 117(5):2354–2365.

[35] Perryman, C. G. (2015). How fast is too fast? Rate-induced bifurcations in multiple time-scale systems. *PhD thesis, University of Exeter*.

[36] Ritchie, P. and Sieber, J. (2016). Early-warning indicators for rate-induced tipping. *Chaos: An Interdisciplinary Journal of Nonlinear Science*, 26(9):093116.

[37] Ritchie, P. and Sieber, J. (2017). Probability of noise- and rate-induced tipping. *Physical Review E*, 95(5).

[38] Rothman, D. (2019). Characteristic disruptions of an excitable carbon cycle. *PNAS*, 116(30).

[39] Sharpe, S. and Lenton, T. M. (2021). Upward-scaling tipping cascades to meet climate goals: plausible grounds for hope. *Climate Policy*, 21(4):421–433.

[40] Srzednicki, R. (2004). Wazewski Method and Conley Index. In *Handbook of Differential Equations: Ordinary Differential Equations*, volume 1, pages 591–684. Elsevier.

[41] van der Bolt, B. and van Nes, E. H. (2021). Understanding the critical rate of environmental change for ecosystems, cyanobacteria as an example. *PLOS ONE*, 16(6):e0253003.

[42] Wieczorek, S., Ashwin, P., Luke, C. M., and Cox, P. M. (2011). Excitability in ramped systems: the compost-bomb instability. *Proceedings of the Royal Society A: Mathematical, Physical and Engineering Sciences*, 467(2129):1243–1269.

[43] Wieczorek, S., Xie, C., and Ashwin, P. (2021a). Rate-induced tipping: Thresholds, edge states and connecting orbits. arXiv:2111.15497.

[44] Wieczorek, S., Xie, C., and Jones, C. K. R. T. (2021b). Compactification for Asymptotically Autonomous Dynamical Systems: Theory, Applications and Invariant Manifolds. *Nonlinearity*, 34(5):2970–3000.

[45] Yu, Y., Muratov, C. B., and Moore, R. O. (2019). Importance sampling for thermally induced switching and non-switching probabilities in spin-torque magnetic nanodevices. *IEEE Transactions on Magnetics*, 55(9):1–11.